# UNIVERSIDAD COMPLUTENSE DE MADRID

## FACULTAD DE CIENCIAS FÍSICAS


# TESIS DOCTORAL

Desarrollo de láseres de pulsos ultracortos de supercontinuo coherente todo-fibra y aplicación en microscopía óptica no lineal

Development of all-fiber coherent supercontinuum ultrashort-pulse lasers and application to nonlinear optical microscopy

MEMORIA PARA OPTAR AL GRADO DE DOCTORA

PRESENTADA POR


Azahara Almagro Ruiz


DIRECTORES


Pere Pérez Millán

Francisco Javier Solís Céspedes

# UNIVERSIDAD COMPLUTENSE DE MADRID

Facultad de Ciencias Físicas
Departamento de Física de Materiales

TESIS DOCTORAL

Programa de DOCTORADO EN FÍSICA D9AD/RD99

**Desarrollo de láseres de pulsos ultracortos de supercontinuo coherente todo-fibra y aplicación en microscopía óptica no lineal**

**Development of all-fiber coherent supercontinuum ultrashort-pulse lasers and application to nonlinear optical microscopy**

MEMORIA PARA OPTAR AL GRADO DE DOCTORA
PRESENTADA POR

Azahara Almagro Ruiz

DIRECTORES

Pere Pérez Millán
Francisco Javier Solís Céspedes

Valencia, 2023

UNIVERSIDAD
COMPLUTENSE
MADRID

# DECLARACIÓN DE AUTORÍA Y ORIGINALIDAD DE LA TESIS PRESENTADA PARA OBTENER EL TÍTULO DE DOCTOR

D./Dña. Azahara Almagro Ruiz,
estudiante en el Programa de Doctorado en Física,
de la Facultad de Ciencias Físicas de la Universidad Complutense de Madrid, como autor/a de la tesis presentada para la obtención del título de Doctor y titulada:

Desarrollo de láseres de pulsos ultracortos de supercontinuo coherente todo-fibra y aplicación en microscopía óptica no lineal

y dirigida por: Pere Pérez Millán y Francisco Javier Solís Céspedes

**DECLARO QUE:**

La tesis es una obra original que no infringe los derechos de propiedad intelectual ni los derechos de propiedad industrial u otros, de acuerdo con el ordenamiento jurídico vigente, en particular, la Ley de Propiedad Intelectual (R.D. legislativo 1/1996, de 12 de abril, por el que se aprueba el texto refundido de la Ley de Propiedad Intelectual, modificado por la Ley 2/2019, de 1 de marzo, regularizando, aclarando y armonizando las disposiciones legales vigentes sobre la materia), en particular, las disposiciones referidas al derecho de cita.

Del mismo modo, asumo frente a la Universidad cualquier responsabilidad que pudiera derivarse de la autoría o falta de originalidad del contenido de la tesis presentada de conformidad con el ordenamiento jurídico vigente.

En Madrid, a 13 de junio de 2023

Azahara

Fdo.: AZAHARA ALMAGRO RUIZ

Esta DECLARACIÓN DE AUTORÍA Y ORIGINALIDAD debe ser insertada en la primera página de la tesis presentada para la obtención del título de Doctor.

*"Templa Casilda, que lo que pasa conviene"*

*María de los Mares Ruiz y José Almagro*

*Dedicado a mis padres*

*y a mi hermana*

# Agradecimientos

Si me lo propongo, estos agradecimientos podrían ser más extensos que la propia tesis, pero me hace ilusión que la gente la lea, así que voy a hacerla breve. Tengo la fortuna de haber contado hasta ahora con muy buenas amistades y muchas personas que me han apoyado y ayudado en estos treinta años de vida.

Primero quiero darle las gracias a las personas del entorno académico sin las que este trabajo no habría sido posible. A mis UCOprofes de la carrera de Física que encaminaron mis pasos hacia el mundo de la óptica, Antonio Dengra y Antonio Ortiz: gracias por impulsarme y por enviarme a ese Curso de Introducción a la óptica del CSIC, y por la paciencia durante el desarrollo de mi TFG. A mis profesores del máster por descubrirme la "magia" de los láseres y terminar de definir mi futuro profesional. A FYLA al completo y todas las personas con las que he podido trabajar en estos cinco años en esta empresa que me ha permitido llegar hasta aquí. Quiero empezar por las personas que han colaborado con nosotros para lograr el desarrollo de los láseres. Al grupo de XLIM, Romain Dauliat, Raphael Jamier y Philippe Roy por su experiencia y ayuda con las fibras "especiales". A David Castelló por su grandísima aportación numérica a esta tesis con sus conocimientos teóricos de generación de supercontinuo. Al equipo de Sphere, Rosa Romero, Paulo Guerreiro, Miguel Miranda y Helder Crespo por su empeño en conseguir un excelente sistema de compresión de pulsos. Al equipo del ICFO, Marina Cunquero, Gustavo Castro y Pablo Loza, por las maravillosas imágenes logradas con su colaboración. A mi director, Javier Solís y a mi tutora, Paloma Fernández, porque sin ellos, su apoyo y sus conocimientos de los entresijos de la universidad no podría haberlo hecho.

A mis primeros "jefesitos" "el Dr. Abreu" y Jorge Pérez. Aunque nuestros caminos se separaron pronto, las bromas en el laboratorio quedan para el recuerdo. Salva, a.k.a. "el Dios de FYLA", te quiero dar las gracias por tus explicaciones sobre el supercontinuo y los empalmes de fibra, y por compartir siempre el chocolate secreto del cajón. Sergio, sin ti no habría podido hacer los experimentos del RIN y lo sabes, mil gracias por demostrarme con un poco de tiempo que eres un grande. Mis dos "Estherillas", la doctora y la de marketing, solo podía quedar una, ¡estaba claro! Gracias por vuestras grandes ideas y consejos, ¡os habéis ganado los "mini puntos Esther"!; y por los eventos feministas que hemos compartido entre talleres por el día de la mujer y

manifestaciones, sin vosotras no sería lo mismo. Aitoret, los mejores viajes de FYLA ya sabes que son contigo, desde Barcelona hasta Ámsterdam (¡volveremos a por más tulipanes!); y las mejores fiestas ADSL por Valencia también, moltes gràcies per tot. Carlos, gracias por socorrerme con la electrónica y por seguir poniéndome al día con las novedades de Marvel. Sabes que eso es esencial, ¿verdad? Martín, a ti tengo que darte las gracias por las piezas defectuosas y de prueba de las impresoras 3D, que en lugar de tirarlas a la basura me las ofreces a mí. ¡Es material aprovechable! Héctor, creo que eres de los que más me han aguantado horas de coche, así que gracias por escuchar todas las historias de novelas y fanfictions que te fui narrando en esos viajes, y sobre todo gracias por los buenísimos memes que han surgido de tu mente y tu ordenador. A mis compañeros de producción, el equipo de operaciones que me ha acogido como una más desde principios de año: Alberto, gracias por ser el mejor DJ de la sala "temazos only" y por enseñarme a fabricar de todo; Iván, que nunca falten nuestras conversaciones filosóficas y nuestras excursiones a la playa, y muchas gracias por tus regalos improvisados (¡aún no he roto la taza!); Omarillo y Viorel, mis actuales "jefesitos", gracias por sacar más provecho de mí que yo misma, ¡prometo que no os vais a arrepentir! Eso sí, no me pidáis que sea niñera por bien que os parezca que lo hago, por favor. Chus y Patri, mis compañeras de contabilidad, hemos compartido incidencias de logística y de albaranes, muy buenos momentos juntas y muchos otros de desahogo. ¡Muchas gracias por vuestra paciencia infinita cuando he necesitado algo de vosotras! Pere, cualquier cosa que diga se queda corta para darte las gracias: el tiempo que he necesitado, me lo has concedido, cualquier cosa (razonable) que he pedido, me la has dado, luchas cada día por tu equipo y por la empresa, incluso si eso significa dejarme la puerta de I+D abierta para pasar a producción. Gracias por lo que he aprendido de escritura y por ser mi director de tesis y mi jefe.

Y como no todo en esta vida es trabajar, quiero ahora mencionar especialmente a mis amistades más íntimas y a mi familia, y me voy a permitir hacerlo por ciudades. En Madrid quedaron mis amigas RADFEM: Leireeee, mucho ánimo con tu tesis, que de to' se sale, y muchas gracias por haber sido mi primera compañera de curro, ¡la mejor! Belenius, a mitad de camino entre Madrid y Valencia, gracias por las correcciones, por tu sabiduría infinita y por compartir conmigo la afición por las novelas chinas de cultivación, los libros de Harry Potter y los churros de chocolate en fallas. Mi Rosa "vallekana", gracias por lo que he aprendido de ti, la valentía, que eres una tía de campeonato y me encanta tenerte de amiga. Chemis, Chemita, de ti aprendí a valorar las cosas importantes de la vida cuando se está a tiempo (y tenemos pendiente volver a vernos, ¡'êgraçiao'!). Loreto (mi Lore), gracias por haberme acogido en tu hogar cuando

sobrevivía en aquel zulo inmundo, te debo una. En Salamanca y perdido de la mano de Dios por otros lares, Alejandro, gracias por haberme abierto los ojos a las injusticias del mundo (¡el tecnocom llegará antes de lo previsto!). Y en Córdoba, mi Córdoba, quiero dar las gracias por el camino recorrido junto a mí en la carrera a mis piruletos Noelia, Angasi y Antuan, porque sin vosotros no habría sobrevivido a las asignaturas más chungas y por las risas que nos hemos pegao' entre las prácticas de laboratorio y los viajes en tren. Ale, nos conocimos aleatoriamente, surgió una de esas amistades que se dicen "para siempre" y me alegro muchísimo de ser apoyo la una de la otra (¿otro McFlurry este verano?). Marta, no quiero ni recordar cómo era cumplir años antes de conocerte porque no era lo mismo que encontrarnos en el parque e intercambiar regalos contigo. Me alegro muchísimo de tenerte de amiga y de compartir contigo tanto frikismo (¡orgullo friki a tope!).

"JÁ Power", Kilian y Raquel, mi familia unida por mucho más que la sangre, siempre que os necesito estáis ahí y sabéis que me tenéis siempre con vosotros también. Gracias por los vídeos, las risas, los desahogos, los cumpleaños y todo lo que venga. Que el plomillaso dao' nos siga uniendo. Gaia, a ti te debo también muchos momentos geniales y los mejores bollodramas de Valencia. Pocas cosas me han hecho tanta ilusión en la vida como cuando me pediste que fuera testigo de tu boda. Gracias por tu apoyo y tu compañía, porque incluso cuando no estás, estás. A los tres: os quiero 3000.

Finalmente, a mi familia: mis abuelos Pepe, Isabel, Pilar y Manolo, os quiero infinito, me siento afortunada de ser vuestra nieta. Mis tías y tíos, Montse, Pepa, Juan y Carmen, por hacer entretenidas las comidas familiares. Mi primita Marta, que de primita ya tienes poco con lo mayor que eres, ¡que me alegro muchísimo de que seamos familia! A mis padres, María del Mar y Pepe. Nunca os habríais creído (con razón) que estudiaría un doctorado en física si os lo llegan a decir cuando era un bicho rebelde de ocho años. Sin vosotros no estaría aquí en absoluto. Gracias por todo el amor, el apoyo y los medios para permitir que lo tuviera todo más fácil que mucha gente, incluso el ser yo misma. Y mi "Payasa", Celia, mi hermana, que aunque fueras insufrible de pequeña ahora somos uña y carne. Gracias por escuchar siempre mis desvaríos y mucho ánimo con todo, que estoy muy orgullosa de ti y sé que vas a triunfar (la mejor nutricionista del mundo, tengo pruebas y cero dudas).

A quienes he mencionado y a quienes no caben aquí, muchas gracias.

# Acknowledgements

I know that, if I try, this section could be longer than the thesis itself. But I really want people to read it so I will try to make it short. I am lucky to count with very good friends and people on my way that have supported and helped me during this thirty years of life.

I want to thank first those from the academic environment whom this work of thesis would have not been possible without. To my "UCOprofes" from Physics degree, who led my steps to the world of optics, Antonio Dengra and Antonio Ortiz: thank you for encouraging me and advising me to go to that "Curso de introducción a la óptica" at CSIC. Also, thank you for your patience during my TFG. To my professors from the master, for unveiling the "magic" of the lasers and finally define my professional future. To FYLA and to those whom I have been able to work with during these five years at this company that has allowed me to reach this point. I would like to start by those who has collaborated with us to develop our lasers. To XLIM team, Romain Dauliat, Raphael Jamier and Philippe Roy for their experience and help with the "special" fibers. To David Castelló for his great numerical contribution to this thesis with his knowledge of generation of supercontinuum theory. To Sphere team, Rosa Romero, Paulo Guerreiro, Miguel Miranda and Helder Crespo for their hard work to obtain an excellent pulse compressor. To the team of ICFO, Marina Cunquero, Gustavo Castro and Pablo Loza for the wonderful images achieved with their collaboration. To my thesis director, Javier Solís, and my tutor, Paloma Fernández: without them, their support and their knowledge of the intricacies of the university I could not have done it.

To my first "jefesitos" "el Dr. Abreu" and Jorge Pérez. Even though we went our separate ways early on, the jokes in the laboratory remain in the memory. Salva, a.k.a. "el Dios de FYLA", I want to thank you for your lessons on supercontinuum and fiber splicing, and for always sharing the drawer secret chocolate. Sergio, without you RIN experiments would have been impossible and you know it. Thank you so much for showing me with some time that you are a great guy. To my two "Estherillas", the doctor and the marketing one. Only one could remain, granted! Thank you for your awesome ideas and advices, you have earned the "mini puntos Esther"! Also, thank you for the shared feminist events from the workshops of the Women day to the manifestations: it would not be the same without you. Aitoret, you already know that the best FYLA trips are by your side, from Barcelona to Amsterdam (we will go back to take more tulips!); and the best ADSL parties at Valencia too, "moltes gràcies per tot". Carlos, thank you for saving me with the electronics issues and for keeping me up to date with Marvel news. You know that it is essential, right? Martín, I have to thank you for the defective and trial pieces from the 3D printer because instead of throwing them away you give them to me. They are reusable! Héctor, I think you are one of those who more driving hours has had to suffer with me, so thank you for listening to every novel and fanfiction that I narrated to you during those trips. But, more than everything, thank you for the great memes that came from your mind and computer. To my production colleagues, the operations team that has welcomed me as one of them since early this year: Alberto, thank you for being the best DJ of the "temazos only" room and for teaching me how to manufacture everything; Iván, I wish our philosophical conversations and our trips to the beach never miss, and thank you very much for your improvised gifts (I still have not broken the cup!); Omarillo and Viorel, my current "jefesitos", thank you for getting out more of me than myself, I promise you will not regret it! But, please, do not ask me to babysit your children even if you think I am good at that. Chus and Patri, my accountant colleagues. We have shared logistic and delivery notes incidences, very good times together and some other of venting our emotions. Thank you very much for your infinite patience when I needed something from you! Pere, whatever I can say is never enough to thank you: the time I needed, you allowed it, any (reasonable) request I asked, you answered yes. You fight for your team and the company every single day even if it means leaving the R&D door open for me to move to production. Thank you for what I learned about writing and for being my director and boss.

But not everything in this life is about working, so now I want to specially mention my closest friends and family, and I am doing so by cities. In Madrid stayed my RADFEM friends: Leireeee, good luck with your thesis, everything has an end, and thank you so much for being my first colleague, the best one! Belenius, halfway between Madrid and Valencia, thank you for the revisions, your infinite wisdom and for sharing with me the interest in Chinese cultivation novels, Harry Potter books and the "fallas" chocolate and churros. My Rosa "vallekana", thank you for what I have learned from you: courage. You are such a powerful girl and I love having you as a friend. Chemis, Chemita, I learned from you to value the important things of life when there is still time (and we still have to meet again, êgraçiao!). Loreto (my Lore), thank you for welcoming me in your home when I was surviving in that filthy hole, I owe you. In Salamanca and lost in God forsaken places, Alejandro, thank you for opening my eyes to the injustice of this world (tecnocom will arrive sooner than later!). And in Córdoba, my Córdoba, I want to thank my "piruletos" Noelia, Angasi and Antuan for walking the path of the degree by my side: without you I would not have survived the hardest subjects. Thank you for the lots of laugh we have shared during the laboratory practical lessons and the hours spent in the train. Ale, we met by chance and an "everlasting friendship" was born. I am so happy to be support one of the other! (Another McFlurry this summer?). Marta, I do not want to even recall how was to celebrate my birthday before meeting you. It was not the same as meeting at the park and exchange gifts with you. I am really glad that I have you as a friend and that we share so much freakiness (freak pride!).

"JÁ Power", Kilian and Raquel, my family bonded by much more than blood, anytime I need you, there you are. And you know that you have me with you always as well. Thank you for the videos, the laughs, the anger-venting moments, the birthdays and everything that may come. Let the "plomillaso dao'" keep us together. Gaia, I also owe you a lot of great moments and the best "bollodramas" of Valencia. Few things in my life had thrilled me as much as when you asked me to be witness for your wedding. Thank you for your support and company, because even when you are not there, you are still there. To the three of you: I love you 3000.

Finally, to my family: my grands Pepe, Isabel, Pilar and Manolo, I love you forever, I feel very lucky of being your granddaughter. My aunts and uncles, Montse, Pepa, Juan and Carmen, thank you for making family meals fun. My little cousin Marta, who is little no more since you are so grown already. I am really happy that we are family! To my parents, María del Mar and Pepe. You would have never believed (fair enough) that I would study a Physics PhD if you were told when I was a rebel eight-years old child. Without you I would not be here at all. Thank you for all the love, support and tools that allowed me to have everything easier than so many people, even being myself. And my "Payasa", Celia, my sister. Even though you were insufferable when we were little, now we are inseparable. Thank you for always listening to my ramblings and I wish you the best at everything. I am really proud of you and I know you will success (the best nutritionist in the world, I have proof and zero doubts).

To those mentioned here and those who are not, thank you very much.

# Contents

# Abstract

In this work of thesis titled "Development of all-fiber coherent supercontinuum ultrashort-pulse lasers and application to nonlinear optical microscopy" the aim is to develop architectures of ultra-broadband pulsed emission through the excitation of photonic crystal microstructured fibers and solid graded-index (GRIN) fibers with laser sources at different spectral windows: central wavelength at 1.06 μm and 1.5 μm. We also aim to study the temporal coherence between their pulses. Supercontinuum (SC) laser pulses are compressible to few-cycle temporal widths when there is temporal coherence between them.

Since research in the SC generation field started, SC versatility has been demonstrated for numerous applications: telecommunications, frequency metrology, spectroscopy, nonlinear optical (NLO) microscopy and biomedical imaging, among others. There are designs of architectures that use pump sources of different kinds: solid-state lasers, optical parametric oscillators, semiconductor lasers or optical fiber lasers, among others. They can be continuous wavelength emission sources or ultrashort pulse sources of temporal widths ranging from nanoseconds to femtoseconds. These sources are used to excite optical fibers of a wide variety of characteristics and different materials: tapered fibers, microstructured fibers, graphene waveguides or hollow core fibers filled with gas; fibers with anomalous, normal or all-normal dispersion curves, with zero dispersion values at different wavelengths, etc.

Some of the applications that make use of SC sources require that there is temporal coherence between the pulses emitted by the SC source. A high degree of coherence increases the stability of the emission, decreases the noise intensity and favors the temporal compression of the pulses to their Fourier transform limit (FTL). To avoid that the temporal coherence breaks during the process of

SC generation, it is necessary to exploit nonlinear effects that do not imply solitonic phenomena. Solitonic effects appear when the pulses propagation happens at spectral regions where the chromatic dispersion of the fibers is anomalous. Effects such as self-phase modulation and four-wave mixing under normal chromatic dispersion conditions favor a temporally coherent broadening. It has been experimentally demonstrated that highly coherent SC can be generated exciting all-normal dispersion photonic crystal fibers (ANDi PCF).

In this work we are interested in obtaining commercial coherent SC sources that can be used in applications in which temporally coherent ultrashort pulse lasers are required. To do this, we design the sources from this work based on all-fiber architectures. Benefits of this characteristic are having laser sources permanently aligned, which are robust, do not need periodical maintenance and are easy to use by the end user. All this favors the use of the source and makes it easier to adopt temporally coherent SC sources in laboratories of different disciplines.

In this way, we have obtained an all-fiber coherent SC source exciting ANDi PCFs with an ultrashort pulse fiber laser at high repetition rate based on passive mode-locking at 1.06 μm central wavelength. On the one hand, we manufactured microstructured fibers with different geometrical parameters and studied the kind of spectral broadening that each one produced. With this, we defined the ranges of said parameters. On the other hand, we excited the ANDi PCFs without the need of a free-space coupling stage. We worked on the optimization of the transition between the laser fiber and the ANDi fiber to perform it through fiber splice. With this source we generated a 150 nm bandwidth SC. We studied the temporal coherence between its pulses using a dispersion-scan (d-scan) free-space compressor and confirmed that the temporal width of the compressed pulse, 12.6 fs, was practically its FTL. This development together with the proper electronical and mechanical design and a user-friendly software interface, has allowed to commercialize this source in the field of NLO microscopy. We have studied its performance as illumination source in multispectral and multimodal NLO microscopy. We have obtained different images of biological specimens through two-photon excitation fluorescence (2PEF), simultaneously in several fluorophores of absorption at different wavelengths. We have also obtained images combining this technique with second harmonic generation (SHG), allowing to observe neurons, muscle and pharynx from a C. elegans specimen in vivo. Our studies have shown that using this all-fiber coherent SC source allows to image dispersive tissue specimens with cellular resolution and at deeper penetration lengths than with traditional sources.

In addition, we have developed an all-fiber SC source centered at 1.5 μm exciting solid core GRIN fibers with zero-dispersion wavelengths around 1535 nm. Experimentally we studied the generation of SC exciting fibers of different core diameters and lengths at different repetition rates, obtaining a SC spectrum of ~ 600 nm. Also, we simulated the SC generation depending on the length of the excited fiber and compared it with the experimental results finding a good correspondence, qualitatively, between them. We studied the compression of the pulses and measured the degree of temporal coherence between two consecutive pulses through an interferometric experiment.

In conclusion, we have developed and manufactured sources of SC emission at 1.06 μm y a 1.5 μm, respectively; the temporal coherence of the first has been demonstrated by the compression of the pulse to almost its FTL and the temporal coherence of the second has been measured. Finally, high resolution images of biological samples have been obtained through NLO microscopy techniques illuminating the samples with the 1.06 μm source.

# Resumen

En este trabajo de tesis titulado "Desarrollo de láseres de pulsos ultracortos de supercontinuo coherente todo-fibra y aplicación en microscopía óptica no lineal" se tiene por objetivo desarrollar arquitecturas de emisión pulsada de amplio ancho de banda mediante la excitación de fibras microestructuradas de cristal fotónico y fibras sólidas de gradiente de índice (GRIN) con fuentes láser en distintas ventanas espectrales: longitud de onda central en 1.06 μm y 1.5 μm. También se pretende estudiar la coherencia temporal entre sus pulsos. Cuando existe coherencia temporal entre los pulsos generados a la salida de láseres de supercontinuo (SC), dichos pulsos son comprimibles hasta duraciones temporales de pocos ciclos ópticos.

Desde que se comenzó a investigar el campo de la generación de SC se ha demostrado su versatilidad para numerosas aplicaciones: telecomunicaciones, metrología de frecuencia, espectroscopía, microscopía óptica no lineal (NLO) y obtención de imágenes en biomedicina, entre otras. Existen diseños de arquitecturas que utilizan fuentes de bombeo de diversos tipos: láseres de estado sólido, osciladores paramétricos ópticos, láseres de semiconductor o láseres de fibra óptica, entre otros, que pueden ser de onda continua o de pulsos cortos con duraciones desde nanosegundos hasta femtosegundos. Con estas fuentes se excitan fibras ópticas que también han sido probadas con una amplia variedad de características y materiales diferentes: fibras cónicas, microestructuradas, guías de onda de grafeno o fibras de núcleo hueco rellenadas con gas; fibras con curvas de dispersión anómala, normal o todo-normal, con ceros de dispersión en diferentes longitudes de onda, etc.

Para algunas de las aplicaciones en las que se pueden emplear fuentes de SC, se tiene que dar la condición de que exista coherencia temporal entre los pulsos emitidos por la fuente de SC. Un alto grado de coherencia confiere propiedades

de mayor estabilidad, menor intensidad de ruido y la capacidad de compresión temporal de los pulsos hasta el límite permitido por su transformada de Fourier (FTL). Para que la coherencia temporal no se rompa durante el proceso de generación del SC, es necesario explotar efectos no lineales que no impliquen fenómenos solitónicos, que se dan cuando la propagación de los pulsos se produce en regiones del espectro en los que la dispersión cromática de las fibras es anómala. Efectos como la automodulación de fase y la mezcla de cuatro ondas en condiciones de dispersión cromática normal favorecen un ensanchamiento temporalmente coherente. Se ha demostrado experimentalmente que se pueden generar SCs altamente coherentes excitando fibras de cristal fotónico de dispersión todo-normal (ANDi PCF).

En este trabajo tenemos interés en obtener fuentes de SC coherente comerciales que se puedan utilizar en aplicaciones que requieran el uso de láseres de pulsos ultracortos temporalmente coherentes. Para ello, diseñamos las fuentes de este trabajo con arquitecturas todo-fibra. Los beneficios de esta característica, que son tener fuentes láser permanentemente alineadas, robustas, que no necesitan mantenimiento periódico y de fácil manejo para el usuario final, favorecen el uso de la fuente y facilitan la adopción del SC temporalmente coherente en laboratorios de distintas disciplinas.

Así se ha obtenido una fuente todo-fibra, de emisión SC coherente excitando ANDi PCFs con un láser de fibra de pulsos ultracortos de alta frecuencia de repetición basado en bloqueo de modos pasivo a la longitud de onda central de 1.06 μm. Por un lado, tras fabricar fibras microestructuradas con distintos parámetros geométricos y estudiar el tipo de ensanchamiento espectral que cada una de ellas producía, se acotó el rango de dichos parámetros. Por otro lado, el trabajo de optimización de la transición entre la fibra del láser y la fibra ANDi permitió que estas fibras fuesen excitadas de forma directa sin necesitar una etapa de acoplamiento a espacio libre. Se generó con esta fuente un supercontinuo de 150 nm de ancho de banda y, finalmente, se estudió su coherencia temporal mediante un compresor de espacio libre de escaneo de dispersión (d-scan) confirmando que la duración del pulso comprimido, 12.6 fs, era prácticamente su FTL. Este desarrollo, sumado al diseño electrónico y mecánico adecuado y al de un software de interfaz fácil de usar, han permitido la comercialización de esta fuente en el ámbito de la microscopía NLO. Concretamente, hemos estudiado su desempeño como fuente de iluminación en microscopía NLO multiespectral y multimodal, obteniendo: imágenes de diferentes especímenes biológicos a través de la fluorescencia de excitación de dos fotones (2PEF), simultáneamente en varios fluoróforos con absorción en distintas longitudes de onda; imágenes con la combinación de esta técnica y la generación de señal de segundo armónico (SHG), permitiendo observar a la vez neuronas, músculo y faringe de un espécimen C. elegans in vivo. Los estudios han demostrado que la utilización de esta fuente de SC coherente todo-fibra permite obtener imágenes de especímenes de tejido dispersivo con resolución celular y a mayor profundidad que con fuentes de uso tradicional.

También se ha desarrollado una fuente todo-fibra de SC centrada en 1.5 μm excitando fibras GRIN de núcleo sólido con cero de dispersión en torno a 1535 nm. Experimentalmente se estudió la generación de SC excitando fibras de distintos diámetros de núcleo y longitudes a distintas frecuencias de repetición, llegando a obtener un espectro SC de ~ 600 nm. Asimismo, se simuló la generación de SC en función de la longitud de la fibra excitada y se comparó con los resultados experimentales obteniendo una buena correspondencia cualitativa. Se hizo un estudio de la compresión del pulso usando un compresor de cuñas de espacio libre y se midió el grado de coherencia temporal entre dos pulsos consecutivos mediante un experimento de interferencia.

En conclusión, se han desarrollado y fabricado fuentes de emisión SC a 1.06 μm y a 1.5 μm, respectivamente; se ha demostrado la coherencia temporal de la primera mediante la compresión del pulso a casi su FTL y se ha medido la coherencia temporal de la segunda. Finalmente, se han tomado imágenes de alta resolución de muestras biológicas iluminadas con la fuente a 1.06 μm mediante técnicas de microscopía NLO.

# Chapter 1

# Introduction

Supercontinuum (SC) sources have attracted increasing interest since the first publications demonstrating wide emission spectra in the early 70s [1,2] as they enable applications where narrower spectra are a limitation, in fields like telecommunications, metrology and nonlinear optical (NLO) microscopy, among others. Applications where these sources present advantages are wavelength division multiplexing [3,4], frequency comb metrology [5–7], spectroscopy [8], generation of few-cycle pulses [9–11], optical coherent tomography [12,13], two-photon fluorescence imaging, multimodal and multispectral microscopy or coherent anti-Stokes Raman scattering [14–17], to give just some examples.
The generation of the SC spectrum occurs when some light seed (originally of narrow-band pulses) travels through highly nonlinear (NL) media. There, several nonlinear effects (NLE) are induced if the incident light seed is intense enough. These NLE broaden the light seed spectrum in different ways, depending on the kind of processes involved as the spectrum gets wider. When the group velocity dispersion (GVD) of the NL medium is contained in the anomalous regime, the broadening is led by solitonic effects such as soliton fission [18,19] and modulation instability [20], mixed with dispersive waves [21–23], Raman scattering [24], self-phase modulation [25–27] and four-wave mixing [28,29]. The new frequencies that appear in the spectrum of the pulses have different intensities and do not conserve pulse-to-pulse temporal coherence during the SC generation. Instead, when the GVD of the NL medium is contained in the normal region, the broadening is dominated by self-phase modulation [30]. Solitonic broadening effects are effectively avoided during the first stages of the SC generation. In that case, the resulting SC is not dependent on noise and pulse-to-

pulse coherence is maintained if the pumping source itself is coherent. The NL medium commonly used to efficiently generate coherent SC are photonic crystal fibers (PCFs). To understand the differences in the SC generation depending on the dispersion region and the NL medium, it is necessary to explain the main effects which can dominate the broadening process and the properties of the PCFs. A brief introduction to optical fibers, their design characteristics and dispersion properties follows in section 1.1. Then, the main broadening effects involved in the SC generation are described in section 1.2 and the concept of temporal coherence is introduced. Finally, section 1.3 highlights the aim of this PhD thesis: to efficiently generate SC at different central wavelengths of interest for NLO microscopy (1.06 and 1.5 μm) by exciting optical fibers under the normal dispersion regime to maintain pulse-to-pulse temporal coherence. We also give a brief revision of the state-of-the-art.

## 1.1. From standard fibers to PCFs

Standard optical fibers are a cylindrical kind of waveguide that transfer light through its length by means of the total internal reflection. They typically consist of two main parts, a core and a cladding with different refractive indices and diameters $d_c$ and $d_{cl}$, respectively, of typical sizes in the range of micrometers. When the refractive index of the core, $n_c$, is larger than that of the cladding, $n_{cl}$, light is confined inside the optical fiber core and propagates without escaping the fiber through the cladding. The fibers for which the index changes abruptly between the core and the cladding are called step-index (SI) fibers (Fig. 1.1 a)); and when the index of the core changes gradually in the radial coordinate, $\Delta n_c$, the fibers are called graded-index (GRIN) fibers (Fig. 1.1 b)). Also, another characteristic of standard fibers that divides them into two types is the number of transversal modes they can propagate. The fibers that can guide multiple transversal modes are defined as multi-mode (MM), while the kind that only supports one mode, the fundamental transversal mode, is called single-mode (SM). Regarding the aspect of polarization of the incident light, there are some fibers that can maintain the polarization of the light throughout the propagation: polarization maintaining (PM) fibers.

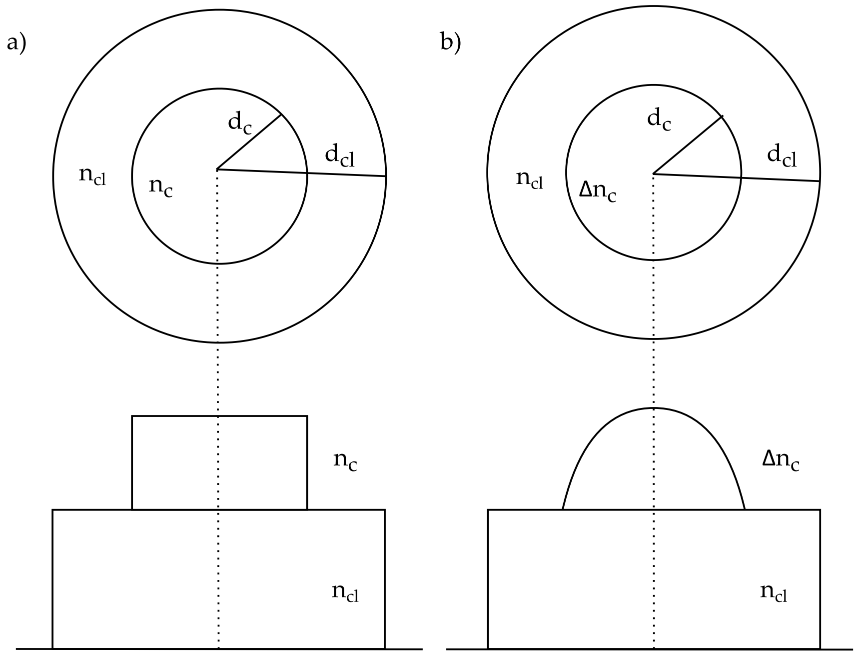


Figure 1.1. Cross section and refractive index profile of a) step-index and b) graded-index fibers.

The study presented in this work focuses on the propagation of pulses, so some of the basic concepts related to their propagation through optical fibers are introduced: the attenuation coefficient, $\alpha$, the mode-propagation constant, $\beta(\omega)$, and the NL refractive index coefficient, $n_2$. The attenuation coefficient $\alpha$ is used to describe the losses that an optical pulse of initial power $P_i$ suffers when traveling through a fiber of length $L$:

$$P_{out} = P_i e^{-\alpha L} \tag{1.1}$$

being $P_{out}$ its output power at the end of the fiber. Since the fiber lengths used to generate SC in this work are in the range of centimeters and their attenuation is of $\alpha$ ~ 0.2 dB/km, losses are neglectable.

When the optical fiber interacts with a propagating electromagnetic wave the medium absorbs the radiation from the wave at resonant frequencies, $\omega_j$, through oscillations of the bound electrons with a certain strength, $B_j$. This dependence of the medium response on the frequency translates into the dependence of the refractive index on the frequency, $n(\omega)$ [31]. This property is known as chromatic dispersion and it is expressed through the mode-propagation constant, the change per unit length of the phase of the electric field in the frequency domain, $\beta(\omega)$ (Eq. (1.2)) [31]:

$$\beta(\omega) = n(\omega)\frac{\omega}{c} =$$
$$\beta_0 + \beta_1(\omega - \omega_0) + \frac{1}{2}\beta_2(\omega - \omega_0)^2 + \frac{1}{6}\beta_3(\omega - \omega_0)^3 + \cdots \quad (1.2)$$

where

$$\beta_1 = \frac{d\beta}{d\omega} = \frac{1}{v_g},\ \beta_2 = \frac{d}{d\omega}\left(\frac{1}{v_g}\right),\ \beta_m = \left(\frac{d^m\beta}{d\omega^m}\right)_{\omega=\omega_0} \quad m = (0,1,2,3,\dots) \quad (1.3)$$

in the Taylor series expansion of $\beta$ around the central frequency $\omega_0$ [31]. $c$ is the speed of light travelling through vacuum.

The first-order term, $\beta_1$, is the inverse of the group velocity, $v_g$, the velocity at which the envelope of the pulse propagates, while the second-order term, $\beta_2$ or GVD parameter, describes the dispersion of the group velocity. Also, as we are mainly describing propagation through optical fiber media, there is another parameter commonly used in the field of optical fibers for dispersion, $D$, which is related to $\beta_2$ as follows:

$$D = \frac{d\beta_1}{d\lambda} = -\frac{2\pi c}{\lambda^2}\beta_2 \quad (1.4)$$

In the field of telecommunications, silica fibers geometrically designed to guide the fundamental mode at the 1.5 μm wavelength are commonly used and considered to be the standard fibers. The typical curves of dispersion $D(\lambda)$ that can be found in the literature for said fibers (Fig. 1.2) present a wavelength for which the value of dispersion is equal to zero. Said wavelength is called zero-dispersion wavelength (ZDW) and it divides the GVD into two regions: normal dispersion regime for D < 0 (GVD > 0) and anomalous dispersion regime for D > 0 (GVD < 0). The guiding properties of the fiber impose an effective refractive index to the propagating light which combines the geometric and the material components. The effective refractive index tends to be lower than that of the material inducing a shift of the ZDW to longer wavelengths (~ 1.31 μm for standard silica fibers) [31]. In the context of femtosecond pulses propagating near the ZDW [32] it is necessary to take also into account the third-order dispersion (TOD) term $\beta_3$ since it is the slope of the curve of the GVD around that wavelength.

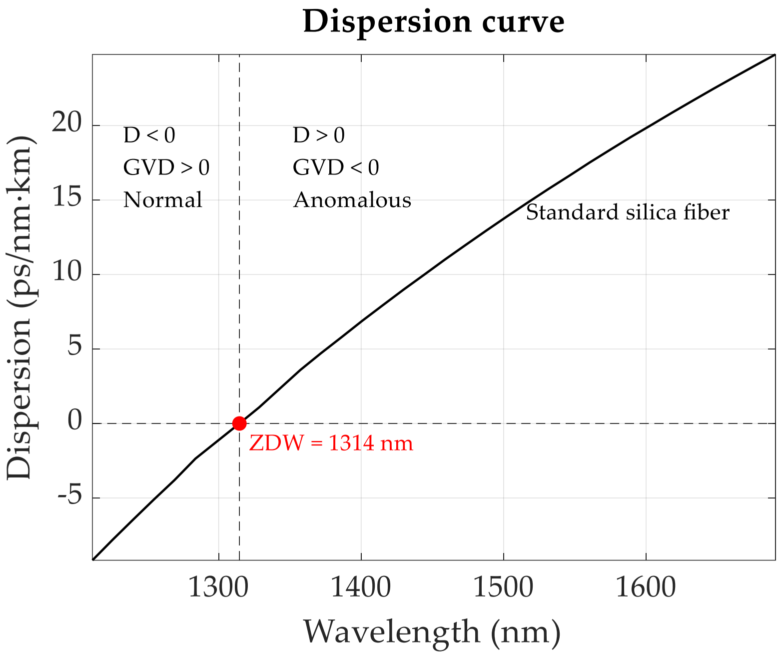


Figure 1.2. Dispersion as a function of wavelength and ZDW of standard silica fibers for the third window of telecommunication (1.5 μm).

When NL polarization is induced to the medium where the pulses propagate, the refractive index turns dependent on the optical intensity of the pulses [31]. This dependence is expressed through the NL refractive index coefficient, $n_2$:

$$n(\omega, I(t)) = n(\omega) + n_2|E(t)|^2 \tag{1.5}$$

where $n(\omega,I)$ is the total refractive index, $n(\omega)$ is the linear refractive index and $E(t)$ is the electric field of the pulses propagating through the medium as a function of time, $t$. The $n_2$ coefficient in silica fibers is typically lower than that of bulk media by two orders of magnitude (~ $2.3{\cdot}10^{-20}$ m$^2$/W [31]). Nonetheless, standard optical fibers present the length, low loss and modal effective area suitable to generate NLE at low pulse energies in the range of nanojoules [31]: $\alpha$ ~ 0.2 dB/km around 1550 nm for silica fibers and core diameters in the micrometers range (< 10 μm). At different wavelength ranges, though, losses are higher, the mode field diameter (MFD) is also higher for longer wavelengths, which decreases the intensity, and for shorter wavelengths not only the fundamental mode propagates but higher modes as well. The performance of standard fibers as NL media is limited by the design and material of the fibers. Nowadays, the dispersion engineering has allowed to overcome those limitations with the fabrication of new kinds of fibers that have their dispersion curves shifted or reshaped due to its dependence with the parameters of the fiber design: dispersion-shifted and microstructured optical fibers (MOFs) [33], respectively.

Dispersion-shifted fibers (DSF) are based in the design of particular refractive index profiles of the fibers through different material compositions, so that the material dispersion compensates the waveguide dispersion at the desired wavelength, thus shifting the ZDW of said fiber [34–36]. Instead, MOFs design started from the idea of confining the light with a new geometry based on photonic crystals [37], which would induce a modified total internal reflection by changing the waveguide properties. The guiding conditions of a MOF are determined by wavelength-scale holes performed on its cladding that run along the length of the fiber and surround the core in the form of a microscopic lattice [38]. The core of the fiber, depending on what it will be used for, can be solid or a hole of air. The first kind are the solid core PCFs typically used to generate SC, and the second are hollow core photonic bandgap (HC-PBG) fibers. While both of them are PCFs, the last kind is usually referred to as HC or HC-PBG fibers because the PBG is what modifies the propagation of the pulses through these fibers [39,40]. In contrast to pulse propagation through solid core PCFs, where NLE modify the propagation of the pulses, NLE are generally avoided in the pulse propagation through HC-PBG fibers. Thus, one of the applications for which their use is exploited is the pulse compression at the last stage of the chirped pulse amplification (CPA) technique, where NLE are usually unwanted [41,42].

In this work we focus on solid core PCFs. Fig 1.3 shows their standard geometry. It is a hexagonal array of holes with two main parameters that influence the refractive index and dispersion curve of the fiber: the diameter of the holes, $d$, and the periodic distance between them or pitch, $\Lambda$. There are several advantages to this kind of geometry. First of all, one of the first characteristics observed for solid core PCFs was the preservation of single-mode propagation (single-modedness) for a wide range of wavelengths and for long fiber lengths [43,44]. This distance $\Lambda$ between the microscopic holes is in the range of micrometers. Such distance is small enough to block the fundamental mode of the fiber from escaping the core through the solid gaps between the air holes along the fiber length. However, the intensity distribution of the higher transversal modes is such that the lobes of these modes can slip through the glass in between the holes [45]. Another advantage is the design flexibility offered by the geometry parameters of the fiber [46,47], which enables dispersion engineering. Multiple dispersion curves with new features can be achieved through the design of these fibers as for example: the shifting of the ZDW in wide wavelength ranges from the visible to the far infra-red [48,49], ultra-flattened dispersion curves for ranges of wavelengths of several hundreds of nanometers [50,51], and even inducing two different ZDWs or a total bending of the dispersion curve to reach all-normal dispersion (ANDi) curves [52–54].

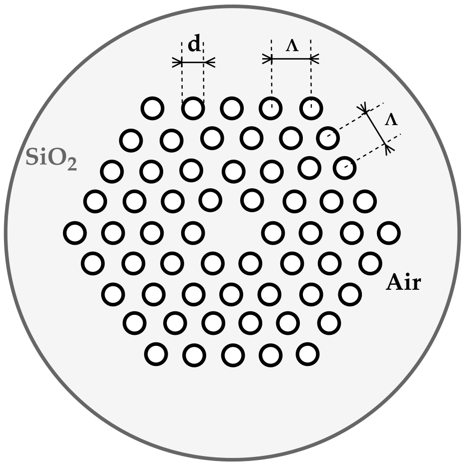


Figure 1.3. Cross section of a $SiO_2$ solid core PCF with standard hexagonal array geometry of air holes. $\Lambda$: distance between consecutive holes, $d$: diameter of the holes.

## 1.2. Spectral broadening effects

### 1.2.1. Soliton dynamics for picosecond pump pulses

At first, since bulk media presented clear NL properties at values of intensity at which optical fibers did not, exciting NLE was more advantageous in bulk media. When losses in optical fiber propagation were reduced (down to < 1 dB/km), it was observed that optical fibers were also appropriate media to generate NLE [55–57]. Furthermore, even though the NL refractive index coefficient for optical fibers is typically lower than that of bulk media as explained before, the typical sizes of the fiber cores confine the light to a few of microns (< 10 μm) which allows to induce NLE at low power levels of the input pulses [58]. With these observations came the discovery of solitons [59], a kind of pulses for which NLE compensate the dispersive effect of the fiber so that the pulses propagate for long distances maintaining their temporal shape. Solitons are the solution to the propagation equation, Eq. (1.6), when picosecond pulses propagate through short SM fibers ($\alpha$ = 0 for fiber lengths of less than 1 km) and the frame of reference $T = t - \beta_1 z$ is taken [31]. $t$ is the propagation time and $z$ is the position of the wave along the axis of propagation. In that case, Eq. (1.6) turns into Eq. (1.7) which is usually referred to as the nonlinear Schrödinger equation (NLSE).

$$\frac{\partial A}{\partial z} + \beta_1 \frac{\partial A}{\partial t} + i\frac{\beta_2}{2}\frac{\partial^2 A}{\partial t^2} + \frac{\alpha}{2}A = i\gamma(\omega_0)|A|^2 A \qquad (1.6)$$

$$i\frac{\partial A}{\partial z} - \frac{\beta_2}{2}\frac{\partial^2 A}{\partial T^2} + \gamma(\omega_0)|A|^2 A = 0 \qquad (1.7)$$

$$\gamma(\omega_0) = \frac{n_2(\omega_0)\omega_0}{cA_{eff}} \qquad (1.8)$$

*A(z,t)* is the slowly varying envelope function, $\beta_1$ and $\beta_2$ account for the first and second-order chromatic dispersion terms, $\alpha$ is the attenuation coefficient and $\gamma$ is the NL parameter which depends on the NL refractive index coefficient, $n_2$ , and on the effective area of the optical fiber $A_{eff}$ (Eq. (1.8)). $\omega_0$ is the central frequency of the pulse.

The solitonic solution appears when the sign of $\beta_2$ is negative, which means that the GVD of the fiber used as NL medium is anomalous for the incident wavelengths. For this reason, when the medium of propagation is pumped with intense pulses in its anomalous GVD region the NLE that widen the spectrum involve soliton-related dynamics. As mentioned before, solitons are a kind of pulses that can propagate through long distances without changing their temporal shape because of the compensation between NL and dispersive effects. The lengths at which dispersive and NL effects take place along the fiber length are the dispersive length, $L_D$, and the NL length, $L_{NL}$:

$$L_D = \frac{T_0^2}{|\beta_2|} \qquad (1.9)$$

$$L_{NL} = \frac{1}{\gamma P_0} \qquad (1.10)$$

where $T_0$ and $P_0$ are the temporal width (half width at 1/e intensity of the pump pulse) and peak power of the pump pulse, respectively. For an input pulse with a given temporal width the required peak power for the fundamental soliton to propagate comes from $N^2 = L_D / L_{NL}$ being equal to 1 (where $N$ is the order of soliton). In that case, the dispersive length is compensated by the NL length, which leads to the conservation of the pulse shape and spectrum through the propagation.

Higher-order solitons (solutions for $N > 1$) have several times more energy (a factor $N^2$) than the fundamental one ($N = 1$). While the fundamental soliton remains with a constant temporal profile during the propagation, the increase in the energy for higher-order solitons makes them evolve in temporal and spectral shape with a certain periodicity called soliton period $z_s$:

$$z_s = \frac{\pi T_0^2}{2|\beta_2|} \tag{1.11}$$

Every soliton period the evolution repeats the same pattern [30]. Said pattern, for an ideal case without perturbations makes these higher-order solitons propagate suffering an initial symmetric broadening of their spectrum and temporal compression for very short propagation distances. After that, the spectrum widens into the long wavelengths' regime asymmetrically and finally it recovers its original shape by the distance $z_s$. This evolution is generated by the interplay between self-phase modulation (SPM), which introduces a positive chirp during the SPM-induced spectral broadening, and anomalous GVD that, in contrast, compensates that effect compressing the pulses again.

### 1.2.2. Soliton dynamics for femtosecond pump pulses

For higher-order solitons, the effect of soliton fission can occur when higher-order dispersion (HOD) and intrapulse Raman scattering disturb their propagation, or by noise amplification when modulation instability (MI) takes part, breaking them into fundamental solitons [60]. These effects, though, due to their dependence with the inverse of $T_0$, only dominate for the propagation of ultrashort pulses (< 1 ps) through the fiber, and a different equation from Eq. (1.7) is required to describe their presence during propagation:

$$i\frac{\partial u}{\partial \xi} - \frac{sign(\beta_2)}{2}\frac{\partial^2 u}{\partial \tau^2} + |u|^2 u = i\frac{\beta_3}{6T_0|\beta_2|}\frac{\partial^3 u}{\partial \tau^3} - \frac{i}{T_0\omega_0}\frac{\partial(|u|^2 u)}{\partial \tau} + \tau_R u\frac{\partial |u|^2}{\partial \tau} \tag{1.12}$$

where

$$u = \sqrt{\gamma L_D}A,\ \ \xi = \frac{z}{L_D},\ \tau = \frac{T}{T_0} \tag{1.13}$$

Eq. (1.12) takes into account the Raman response (through the parameter $\tau_R$) which is neglected for longer pulses as it does not have effect for pulse widths > 1 ps [31]; and the HOD term is included through the TOD parameter $\beta_3$. The variables and parameters of Eq. (1.13) are introduced to follow the notation for soliton theory in the expression of Eq. (1.12).

If the pump pulses generating the higher-order solitons have pulse widths in the femtosecond range and the incident wavelength is near the ZDW, these solitons are not able to restore their spectral shape after the $z_s$ distance. Instead, the spectral broadening keeps happening during the propagation because of the effect of soliton fission. The process of fission occurs when higher-order solitons split into $N$ fundamental solitons, with different energy and group velocity values, inducing new frequencies [30,31,61]. At the effective length for soliton fission $L_{fiss} \sim L_D/N$ [30], the spectrum broadens initially because of the transference of energy from the original pulse to a narrow-band low-amplitude non-solitonic dispersive wave (DW) [22] for a wavelength allowed by the phase-matching condition [62], and from their interaction with solitons themselves [63]. While these new wavelengths are shorter than the original (falling in the normal dispersion regime of the fiber), the generation of longer ones happens because of their amplification thanks to the Raman-induced frequency shift (RIFS) $\Delta\omega_R$ [64–67], that can be expressed as

$$\Delta\omega_R(z) = \frac{-8|\beta_2|\tau_R}{15T_0^3} z \quad (1.14)$$

This shift is called Raman-induced because stimulated Raman scattering is the effect that produces the amplification of the low frequencies of the pulse when its spectral width overlaps with the Raman spectral gain [24,68]. Energy is transferred from the high-frequency components (shorter wavelengths) to the low-frequency components (longer wavelengths) of the pulse.

The combination of RIFS and DW generation yields widening of the pulse spectrum into both the red and blue sides respectively, generating SC spectra that can be of more than several hundreds of nanometers wide for input solitons of $N \geq 10$ [58,69].

A different kind of soliton breaking process is modulation instability (MI) [20,70,71], that has more influence in the spectral broadening for pulse widths > 100 fs, while the previously explained effects are more relevant to pulse widths < 100 fs [30]. The effective length of the MI, which is the distance at which it starts taking place, is expressed through the NL length:

$$L_{MI} = 16L_{NL} \quad (1.15)$$

In the pulse regime where pulse widths are over 100 fs, the higher-order soliton does not propagate through enough distance of the fiber so as to reach its maximum initial broadening because $L_{MI}$ happens to be shorter than the $L_{fiss}$ distance, and so MI starts amplifying the input pulse noise before soliton fission can occur.

This amplified noise affects the soliton propagation inducing the breaking of the pulses in a random process that destroys the coherence of the new fundamental solitons generated from said noise. The soliton fission itself is noise-sensitive and induces a certain amount of spectral and temporal jitter depending on the input pulse noise. In this way, the resulting SC is the mean spectrum from the spectral characteristics of each frequency-shifted soliton and not every wavelength has to be present in each of them at the same time [30]. When MI leads the breakup of the solitons, the generation of the new frequencies is completely incoherent [72,73].

### 1.2.3. Self-phase modulation and four wave mixing

Different NLE can appear for intense enough pump pulses from the third-order polarization term when the third-order susceptibility of the medium, $\chi^{(3)}$, is large enough so as to induce NL polarization in the pumped medium for an applied field. While the effects mentioned in the previous paragraphs depend on the molecular characteristics of the fiber, the parametric effects stemming from $\chi^{(3)}$ can be induced regardless of the intrinsic characteristics of the fiber material. For these effects, it is the design of the fiber as NL medium what controls the interaction among the optical waves [31]. In this subsection we focus in two of these effects that are stronger when pumping PCFs and contribute to the generation of new frequencies: self-phase modulation (SPM) and four wave mixing (FWM).

SPM is a self-induced shift of the phase of the pulse that stems from the dependence of the refractive index with the intensity of the propagating field (see Eq. (1.5)), and it is governed by the term in the right hand of Eq. (1.6). The first term in the right hand of Eq. (1.5) is frequency dependent and the second is intensity dependent. This dependence with the square of the electric field leads to a nonlinear phase shift, $\varphi_{NL}$ (Eq. (1.16)) related to the NL refractive index coefficient, $n_2$:

$$\varphi_{NL}(t) = n_2 \frac{2\pi}{\lambda} L|E(t)|^2 \tag{1.16}$$

where $L$ is the fiber length, and $\lambda$ and $E(t)$ are the wavelength and the electric field of the propagating pulse, respectively. $\varphi_{NL}$ has no influence of the dispersive term ($\beta_2 = 0$) when considering fiber lengths $L$ much shorter than the dispersive length $L_D$ of the fiber. This phase shift $\varphi_{NL}$, which increases with the fiber length, induces the spectral broadening continuously during the propagation through the fiber as a consequence of its dependence with time through the intensity $I(t) = |E(t)|^2$. This is referred to as frequency chirping and implies that for different times the pulse will have different instantaneous optical frequencies, $\omega_{SPM}$, according to the following expression [74]:

$$\Delta\omega_{SPM}(t) = -\frac{\partial\varphi_{NL}(t)}{\partial t} = -n_2\frac{2\pi}{\lambda}L\frac{dI(t)}{dt} \tag{1.17}$$

Considering femtosecond pumping pulses, SPM interacts with dispersion effects and can occur in both anomalous and normal GVD regimes [75]. In the case that SPM-induced spectral broadening contributing to the SC is generated under the normal dispersion region of the dispersion curve of the fiber, the contribution of $\beta_2 > 0$ cannot compensate the positive chirp introduced by SPM. The advantage of this effect is that being self-seeded, when the input pump pulse is coherent, the generated SC is not unstable or noise-dependent, unlike those obtained from soliton-related effects dominating the broadening. That would be the case when the SPM dominates, i.e., when the pumping wavelength lies in the normal dispersion region or for the case of very short (< 50 fs) pulses propagating through very few centimeters length fibers [27]. The disadvantage in such case is that the maximum spectrum width achieved is several hundreds of nanometers smaller than that generated from the mix of SPM and soliton-related effects [30,76]. This is a consequence of the loss of intensity due to the temporal stretching that the dispersion induces to the pulse as it propagates through the fiber. As the pulse intensity decreases, also the capability of the pulse of generating NLE that can broaden the spectrum is reduced.

The way in which the effect of FWM takes part in the generation of SC spectrum comes as well from the third-order susceptibility of the medium. It is a kind of interaction that takes place between four optical waves: two photons with new frequencies $\omega_3$ and $\omega_4$ are generated after the annihilation of two other photons propagating through the fiber with frequencies $\omega_1$ and $\omega_2$. This effect takes place when the phase-matching condition is satisfied [31]:

$$\Delta k = k_3 + k_4 - k_1 - k_2 = \frac{n_3\omega_3 + n_4\omega_4 - n_1\omega_1 - n_2\omega_2}{c} = 0 \tag{1.18}$$

being $\Delta k$ the wavenumbers mismatch, $k_i$ the wavenumbers and $n_i$ the refractive indices of each wave (i = (1, 2, 3, 4)). Considering $\omega_1 = \omega_2$ as a strong pump wave at the central frequency $\omega_0$, the other two new frequencies contributing to the SC spectrum are two symmetrically located sidebands, with respect to the pump frequency, at $\omega_3$ and $\omega_4$. The pumping wave transfers energy to upshifted and downshifted frequencies with respect to the pump frequency according to the energy conservation law: $2\hbar\omega_0 = \hbar\omega_3 + \hbar\omega_4$.

FWM can be SPM-induced when the phase-matching condition is achieved by the effect of SPM [31]. On the one hand, when the pump frequency propagates alone through the fiber, the moment the phase-matching condition allows it, the new sidebands are generated from noise. In fact, FWM is also the description of the MI effect in the frequency domain [72]. On the other hand, when SPM is taking place during the propagation it is possible for the central pump frequency $\omega_0$ to interact with a weak new SPM-generated wave of frequency $\omega_3$. Then, FWM amplifies that particular frequency and generates at the same time the new one at $\omega_4$. SPM-induced FWM contributes to the SC generation not only widening the spectrum but also giving more homogeneity to it, filling wavelength gaps left by the solitonic effects taking place in the anomalous regime of the fiber.

### 1.2.4. Coherence

The combination and complex interplay of all these dynamics and processes is what leads to a wider spectrum for the input femtosecond pulses that propagate through the NL fiber with pump wavelengths near the ZDW in its anomalous dispersion regime. Some experimental examples of SC generated under these conditions can be found in references [76–80] at different pumping wavelengths. Soliton fission can only take place in the anomalous GVD region, while the broadening by MI and FWM can be given in both (although it is more restricted for the normal region [73]). SPM can be induced in both regions, but coherent broadening of the spectrum by SPM only occurs in the normal GVD region [31]. The effects summarized above are just those that have greater impact in the generation of the SC spectrum, but there are other NLE contributing that had been studied in this field [81–84]. Also, regarding the polarization state of the propagating pulses, we are describing these effects from a scalar approach considering them as linearly polarized.

Being the temporal coherence the stability of the phase and amplitude between consecutive pulses, the problem with the SC generated from all these mixed effects is that a lot of fluctuations are present not only in intensity, but also in the relative phase between the different spectral components. In the temporal domain, the pump pulse is split into several pulses from solitonic dynamics and MI, which translates into complex temporal profile of the pulses, hindering its recompression. This, together with the change in the sign of the dispersion of the NL fiber as the spectrum widens and its new wavelengths pumping at both the normal and anomalous GVD regimes, leads to the degradation of the temporal coherence of the pulses because of spectral and phase instabilities [85], and susceptibility to laser shot noise.

## 1.3. Temporally coherent SC generated through ANDi PCFs

During the last years, SC generated from the effects explained in the previous section has been theoretically and experimentally demonstrated by pumping different kind of optical fiber configurations in the anomalous dispersion regime achieving bandwidths of several hundreds of nanometers, and even beyond octave spanning spectra [75,86–92]. However, a SC spectrum originated from soliton-related effects, which are noise-dependent, is bound to be very sensitive to the seed noise introduced by pump input pulses [88,93,94]. Understanding coherence as the stability of the spectral and temporal shot-to-shot intensities, this kind of SC is not coherent as it presents spectral and temporal intensity fluctuations. In fact, the reported results show ultrabroadband octave-spanning SCs at the expense of losing temporal coherence between the pulses.

Of the applications mentioned at the beginning of this introduction, those for which the temporal profile of the pulse is relevant can benefit from SC generation if the temporal coherence is maintained [3,5,8,12,13,95]. A particular example of these are nonlinear optical (NLO) microscopy applications, that require few-cycle pulses to excite the kind of nonlinear effects (NLE) that allows to image the biological samples with high resolution without damaging them [96,97]. Therefore, it is necessary to avoid solitonic effects and broaden the spectrum of the pulses by self-induced processes that maintain temporal coherence. One way is pumping PCFs with femtosecond pump pulses in the normal dispersion regime where SPM dominates, the PCFs having ANDi curves ranging from the shortest to the longest wavelength of the broadened spectrum. This is the key to the conservation of the temporal coherence of the pulses, firstly because the normal dispersion region does not allow soliton-related dynamics, thus avoiding the noise-dependent broadening effects; secondly, because the new frequencies generated during the widening process are also always under normal dispersion conditions; and thirdly, the SC is generated from self-induced broadening effects that can maintain the coherence level of the input pulses. The spectrum resulting from pumping the flattened top of ANDi PCFs is widened with smooth and flat spectral intensity and phase profile, and the conservation of the pulse in the time domain allows the recompression to their Fourier transform limit or near limit (FTL). This is what turns ANDi PCFs into an experimentally and numerically studied NL media for the generation of temporally coherent SC at different pump wavelengths [82,98–105].

The state-of-the-art shows that there are already a great number of reported SC generated with laser sources of short and ultrashort pulses as pump for the ANDi PCF, achieving high degree of coherence [9,11,106–112]. Some works numerically demonstrate SC generation in the wavelength range of 1.5-1.6 μm [110,111,113]. Some other works experimentally demonstrate SC generation either pumping in the 1.5 or the 1.06 μm region, but they do so by means of complex pumping sources [9,11,100,105,107,108,114] and/or do not provide experimental demonstration of the coherence level [108,115]. To actually profit from the advantages that coherent SC presents for NLO microscopy applications, the experimental setup required to generate SC has to make use of pumping laser sources less complex, and more robust and compact. All-fiber lasers can provide these features, do not require alignment or maintenance and can be integrated in the experimental system of the end user in a more accessible way than the free-space pumping sources described in the previous references. Since there is a lack of works showing experimental SC generation using such kind of sources, the aim of this PhD thesis is to develop few-cycle all-fiber laser sources in a range of interest mainly for NLO microscopy applications (0.8-1.8 μm) [116,117], basing our pump laser source in passively mode-locked all-fiber lasers. In this work of thesis, we demonstrate the level of coherence for each of the developed sources.

The thesis is divided into eight chapters, being this Introduction the first one. Second chapter describes the principles of the passively mode-locked oscillators used as pump at 1.06 and 1.5 μm. Third and fourth chapter are dedicated to explaining the design, development and experimental results of the all-fiber few-cycle source at 1.06 μm, and the monolithic fiber SC source at 1.5 μm, respectively. Chapter five describes NLO microscopy applications in which these sources are convenient tools and finally chapters six, seven and eight sum up the conclusions of the work, the future work that can be done and the publications related to the thesis that have been or are in process of being published, respectively.

# Chapter 2

# Passively mode-locked all-fiber lasers

Lasers can be described according to different characteristics: the properties of the emission, the active medium of the cavity or the technique used to generate the stimulated emission are some of the most relevant features used to describe a laser. For this work we focus on lasers of the following characteristics: regarding the temporal emission regime our lasers are periodically pulsed lasers because the light generated is emitted discontinuously in pulses of a certain temporal width and separated in time with certain repetition rate; regarding the active medium of the cavity, we use optical fibers doped with rare earths, which means that our lasers are fiber lasers; to generate ultrashort pulses we use the technique of passive mode-locking, with dispersion management of the cavity to obtain solitonic emission regimes. Depending on the target applications, the wavelength is another parameter that determines the design of the laser. Therefore, the pump light and the active medium are chosen according to the target wavelength. In order to generate emission at 1060 nm the pumping wavelength is set to 976 nm while it is set to 915 nm to obtain 1535 nm emission. The optical fiber acting as active medium is doped with ytterbium (Yb-doped) for the case of 1060 nm and it is co-doped with erbium and ytterbium (Er/Yb-doped) for the case of 1535 nm.

In this chapter, the reader will find a brief explanation on the concepts of amplification of light in rare-earth doped fibers and passive mode-locking as pulse generation technique.

# 2.1. Active medium: Yb- and Er/Yb-doped fibers

Population inversion is necessary to have stimulated emission in a laser cavity (Fig. 2.1). When using rare-earth doped fibers as active medium of the cavity, the dopants of the fiber can invert the population when their electrons absorb incident photons from an optical pump. Then, those electrons are excited from their fundamental (or ground) state to a higher energy state creating an optical gain for the medium. When photons of energy equal to the difference of energy between the excited and the ground state propagating through the medium interact with said excited electrons, their interaction generates the stimulated emission when the electrons relax to an empty lower energy state. For the case of $Er^{3+}$, that lower energy state is the fundamental state of the electrons. For $Yb^{3+}$ there is an intermediate level of lower energy than the upper level and of higher energy than the fundamental state, which drives a better and faster population inversion [118]. This, together with the fact that $Yb^{3+}$ also shows higher absorption efficiency than $Er^{3+}$ [119,120], leads to the use of co-doped Er/Yb fibers in 1.5 μm cavities. In this way, using $Yb^{3+}$ to absorb and $Er^{3+}$ to emit, the pump absorption is higher. Since the emission occurs between the two intermediate levels of the laser transition, cavities built with Yb- or Er/Yb-doped fibers can be considered as two-level systems.

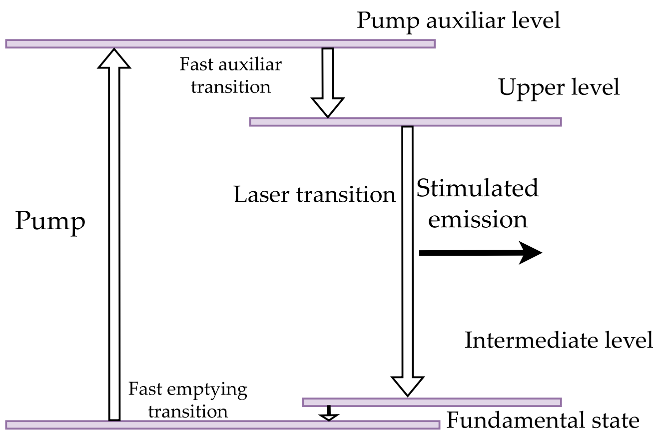


Figure 2.1. Stimulated emission generated in a quasi-three-level system.

The propagation equation introduced in chapter 1 (Eq. (1.6)) describes the propagation of pulses through optical fibers without dopants. Hence, none of its terms includes the population inversion derived from the optical gain induced by the dopants. However, taking into account the dynamics of a two-level system described by the Maxwell-Bloch equations [121], the gain parameters can be included in Eq. (1.6) as follows [122]:

$$\frac{\partial A}{\partial z} + \beta_1 \frac{\partial A}{\partial t} + i\frac{\beta_2}{2}\frac{\partial^2 A}{\partial t^2} + \frac{\alpha}{2}A = i\gamma(\omega_0)|A|^2 A + \frac{i\omega_0}{2\varepsilon_0 c}\langle P_d(r,t)\rangle \tag{2.1}$$

where $P_d(r,t)$ is the polarization induced from the contribution of dopants and $\varepsilon_0$ is the vacuum electric permittivity. The last term in the right hand of the equation accounts for the amplification of the amplitude of the pulse while propagating through rare-earth doped fibers.

## 2.2. Pulsed temporal regime: passive mode-locking

One way of achieving pulsed emission originates from the manipulation of the longitudinal modes of the laser cavity. A typical Fabry-Pérot resonator has two reflective elements (one of them partially reflective, the output coupler) sandwiching an active medium. Like this, the light can keep propagating back and forth inside of the cavity and be amplified in each round as it interacts with the active medium to reach gain values higher than the losses and obtain the laser signal. The length between both reflective sides, $L_c$ (length of the cavity), determines the frequency of the longitudinal modes that are allowed to propagate in said resonator:

$$f_n = \frac{nc}{2L_c} \tag{2.2}$$

where $f_n$ is the frequency of the longitudinal mode $n$, being $n$ an integer number. But this is not the only condition as to what modes can be amplified during the propagation to be part of the laser signal. The gain of the active medium depends on wavelength. The spectral curve of the gain will select some of the modes to be amplified while neglecting others. Generally, the phases and amplitudes of the longitudinal modes effectively resonating are independent and the superposition of all the modes leads to continuous emission. To achieve the desired pulsed emission, the mode-locking technique consists in locking the phases of the different modes so that at a certain moment during the propagation they are in phase and a pulse is generated from the constructive interference of the overlapping modes.

To lock the phases of the propagating modes it is necessary to induce a temporal dependence of the electromagnetic field, and this can be done through the modulation of the gain and/or the losses of the cavity in an active or a passive way. Passive techniques are frequently based on saturable absorbers, optical components with different absorption values depending on the intensity of the incident light. A semiconductor saturable absorber mirror (SESAM) is the absorber used for the mode-locked sources of this thesis. The SESAM modulates the light in the cavity because it absorbs low intensity pulses and saturates with those of high intensity. Therefore, the SESAM acting as one of the reflectors of the cavity favors the propagation of high intensity pulses by reflecting them. Such behavior helps suppressing the noise of the cavity and boosting the self-starting of the laser. The pulses that can propagate will run from the SESAM to the other reflector of the cavity (the output coupler) and then will come back to the SESAM. In this way, the amplified light will keep propagating and a train of pulses will exit the cavity through the output coupler at the repetition rate given by the optical path of one roundtrip. The structure of the SESAM is built from layers of different materials [123] so that one layer absorbs the incident photons up until the material saturates, and the other consists of an anti-resonant Bragg mirror of high reflectivity. The total reflectivity of the device presents a time dependence which is a combination of the constant reflectivity of the Bragg mirror and the time-dependent reflectivity of the saturable layer: the moment the SESAM saturates it stops absorbing and after some recovery time it starts to absorb again. When said recovery time is not much shorter than the incident pulse width but of the order, it cannot be considered as instantaneous. Then, the expression of the SESAM loss *q(t)* is given by [124]:

$$\frac{\partial q(t)}{\partial t} = -\frac{q - q_{ns}}{\tau_{SA}} - q\,\frac{|A(z,T)|^2}{E_{SA}} \tag{2.3}$$

and is related to the time dependence of the reflectivity of the SESAM device *R(t)* through the following expression:

$$R(t) = 1 - q(t) - l \tag{2.4}$$

where $q_{ns}$ is the non-saturated loss, $E_{SA}$ and $\tau_{SA}$ are the saturation energy and recovery time, respectively, and $l$ is the intrinsic insertion loss.

The use of a SESAM with finite recovery times can lead to a different kind of mode-locking: the Q-switch mode-lock regime. In the case of fiber lasers using

SESAM for passive mode-locking, the long lifetime of the higher energy state of the rare-earth dopants of the active medium leads to a slow absorption saturation of the SESAM and Q-switch can take place. So, in order to avoid Q-switch mode-locking and ensure stable operation it is necessary to work in a high saturation regime. The exposure of SESAM to such saturation, with high pulse energies reaching its surface and burning it throughout the long operation times of a standard laser source, ends up in the degradation of the device. Therefore, balance must be achieved and the limit as to how high the energy can be is set by the damage threshold of the SESAM (typically of the order of 1 mJ/cm$^2$). Regarding the output coupler of the cavity, the semi-reflector used for the 1060 nm oscillator of this work is a FBG in contrast to the dichroic mirror (DM) used for the 1535 nm oscillator. In the case of the 1535 nm source DMs were a more suitable option because of the high repetition rate of the oscillator. Cavities of the order of gigahertz need to be as short as of few centimeter lengths. FBGs would take about 2 cm of the total of ~ 8 cm of our cavity, a space that needs to be completely built from the active fiber in order to achieve the adequate gain regime. Instead, DMs can be deposited on the surface of the connector of the active fiber. Thus, for the case of the 1535 nm oscillator, in order to have 1.3 GHz repetition rate, we use DMs.

The oscillators used as seed for the sources at 1060 and 1535 nm are based on this technology of SESAM passive mode-locking and are completely built with optical PM fibers and PM fiber components. The PM fibers allow to have a linearly polarized output from the oscillator. This is necessary to avoid the instabilities that can be induced in the amplitude of the pulses during the amplifying stages if the polarization state of the oscillator varies; as well as the spectral variations that would be present in the generated SC, which is dependent on the polarization state. Some previously reported oscillators of this kind can be found in references [125–128]. These oscillators provide the advantages of all-fiber propagation: improved robustness and stability, higher coupling efficiency between the stages of the laser architecture and no beam spatial shape distortion, due to the absence of free-space optical elements as lenses, efficient cooling of the active medium and more compact designs that facilitate the use and transport of the sources in research and industrial environments.

Chapter 3

# Temporally coherent supercontinuum generation at 1.06 μm using ANDi PCFs

As outlined in chapters 1 and 2, SC emission showing highly temporal coherence can be achieved pumping the flat top of the dispersion curve of all-normal dispersion photonic crystal fibers (ANDi PCFs) with ultrafast fiber lasers, and different configurations for the excitation source can be found in the literature. Ti:sapphire (Ti:Sa) oscillators, optical parametric oscillators or master oscillator power amplifiers are examples of free-space pulsed optical sources used to pump ANDi PCFs to generate coherent SC [9,11,108,129,130]. Several works reporting pumping with ultrafast fiber lasers use free-space optics to couple the light between the seed and the PCF [100,106,109,110]. All-fiber configurations of monolithic sources in which all the stages are coupled to each other by fiber splices or fiber-based transitions are compact, air-cooled, turn-key, cost-effective and maintenance and alignment-free [16,127]. To the best of our knowledge, though, none of the current state-of-the-art configurations which demonstrate the compression of temporally coherent SC to transform or near-to-transform-limited few-cycle pulses are all-fiber configurations. For an all-fiber laser architecture, it is a challenge to offer pulses with > 15 kW peak power and < 250 fs duration as excitation pulses because the light is completely confined in the cores of the optical fibers, whose core diameters are typically below 10 μm. A peak power of 15 kW inside guiding fibers of 10 μm core diameter yields intensities of > 15 GW/cm². For propagation lengths of a few centimeters, such high intensities are above the threshold for undesired nonlinear effects (NLE) that distort the laser pulses propagating inside the fibers and, particularly, destroy the temporal coherence of the laser pulses. To overcome this problem, we use a chirped pulse amplification (CPA) system [41], with an all-fiber configuration (Fig. 3.1), where the temporal compression stage is built with a hollow core photonic bandgap (HC-PBG) fiber.

In this chapter we describe the design and development of a monolithic fiber-optic configuration for generating transform-limited temporally coherent SC pulses with central wavelength at 1.06 µm. Few-cycle emission of optimized time-domain quality is confirmed by independent pulse duration measurement techniques: dispersion-scan (d-scan) and interferometric autocorrelation.

# 3.1. Few-cycle all-fiber temporally coherent SC

The all-fiber configuration of the femtosecond temporally coherent SC source is based on a sequential structure of fiber-optic stages, each of them connected to the next by a fused fiber splice, as shown in Fig. 3.1.

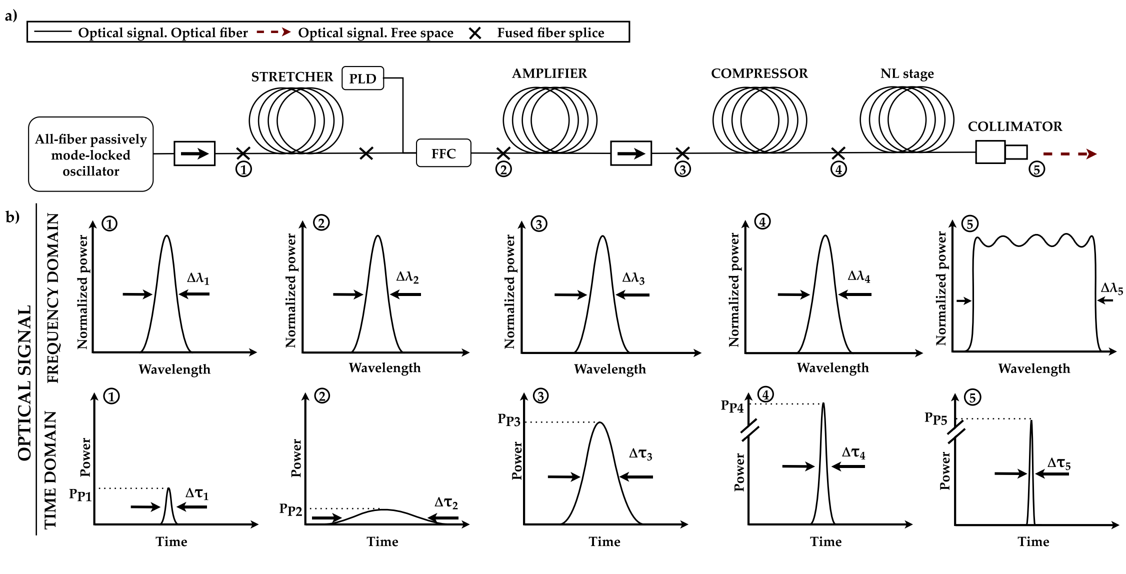


Figure 3.1. a) All-fiber configuration of a temporally coherent SC source of few-cycle pulses. b) Qualitative representation of the spectral and temporal properties of the pulsed optical signal from the first to the last stage of the all-fiber source. PLD: pump laser diode, FFC: fused fiber combiner, NL: nonlinear, $P_P$: peak power, $\Delta\lambda$: spectral bandwidth at full width at half maximum (FWHM), $\Delta\tau$: temporal width at FWHM.

The architecture is composed of several stages. First, an all-fiber passively mode-locked oscillator delivers transform-limited pulses of hundreds of femtoseconds duration and megahertz repetition rate at a certain central emission wavelength. Both, repetition rate and central wavelength, remain constant during the propagation through every stage. Dispersion management is performed in the cavity so as to achieve solitonic emission regime in order to obtain pulses that conserve their shape during the propagation through the cavity. Then, the pulses delivered from this stage undergo temporal stretching in stage 2 by means of a polarization maintaining (PM) single-mode (SM) optical fiber, so that they can be amplified in the next stage without generating NLE. By doing this, the peak power remains below the threshold of generation of NLE in the core of the optical fiber of the subsequent amplifying stage. A PM fused fiber combiner (FFC) launches light from a pump laser diode (PLD) into the active fiber of the amplifying stage, stage 3. This amplifying stage is composed of a double clad PM rare-earth doped active fiber that amplifies the pulses to the maximum possible peak power before inducing NLE that would distort the temporal and spectral shape of the pulses. The rare earth ions of the core of the fiber are pumped to excited states, as explained in chapter 2, by the light coming from the PLD through the first clad of the fiber (which is undoped), and the signal coming from the stretcher is amplified. This amplified signal is then delivered to the fiber compressor, stage 4, where the pulses are compressed by means of a HC-PBG fiber. The aim of this stage is to achieve the peak power required at the input of the fiber of the NL stage to efficiently generate temporally coherent spectral broadening. This fiber compressor is designed with HC-PBG fiber to obtain anomalous dispersion at 1 µm that compensates the normal dispersion previously suffered by the pulses. Also, the air core of the fiber allows to avoid NLE generated due to high peak powers. Thus, the pulses do not suffer changes in their spectrum. The compressed pulses are then sent to the last stage of the all-fiber source, stage 5, a highly NL ANDi PCF designed to have a dispersion curve with a flat top of near-zero-dispersion value at the central emission wavelength of the source. A few tens of centimeters of this fiber induce spectral broadening of the pulsed signal by self-phase modulation (SPM) preserving the temporal coherence of the pulses, which allows to compress them down to pulse durations corresponding to the Fourier limit of their spectrum. At the output of stage 5, the pulsed signal is collimated and delivered to free space.

In subsection 3.1.1 the stages between the oscillator and the fiber compressor are explained in detail. Said group of stages is defined as the seed of the source (Fig.

3.2). This seed pumps the following stage, the ANDi PCF, which is analyzed throughout subsection 3.1.2. Finally, subsection 3.1.3 presents the SC generated with the optimized ANDi PCF and Table 3.2 gathers the main properties of the pulsed signal at the output of each stage discussed throughout section 3.1.

### 3.1.1. All-fiber 1.06 μm femtosecond seed

The architecture of the all-fiber configuration presented above and shown in Fig. 3.1 starts with the four stages that compose the seed of the source (Fig. 3.2).

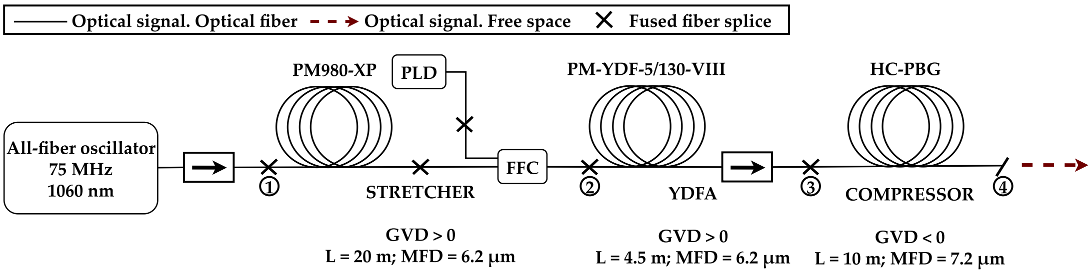


Figure 3.2. Stages of the all-fiber seed used to excite the ANDi PCF of the temporally coherent SC source (Fig. 3.1). PM980-XP: fiber of stage 2, PLD: pump laser diode, GVD: group velocity dispersion, MFD: mode field diameter, FFC: fused fiber combiner, PM-YDF-5/130-VIII: fiber of stage 3, YDFA: ytterbium-doped fiber amplifier, HC-PBG: hollow core photonic bandgap.

The first stage is the passively mode-locked oscillator (Fig. 3.3), an Yb-doped linear fiber cavity with a semiconductor saturable absorber mirror (SESAM) acting as one of the reflectors and a chirped fiber Bragg grating (CFBG) acting as output coupler. The light generated from a pump laser diode (PLD) (BL976SAG300, Thorlabs) at 976 nm pumps the Yb-doped active fiber of the cavity through the input port of a wavelength division multiplexer (WDM) built in PM fiber. It is delivered to the first component of the resonator, the CFBG (DMR-1060-13.5-11(+D0.202+0)-P1, TeraXion) with ~ 10 % reflectance at 1060 nm (Fig. 3.4 a)) and 13.5 nm reflection bandwidth. This device is specifically tailored to obtain a net group delay dispersion (GDD) anomalous and close to zero in the cavity. The GDD corresponds to the group velocity dispersion (GVD) that the pulses suffer after propagating through a certain distance of fiber *L* [131], so they both have the same sign, which is the opposite sign of the value of the dispersion parameter *D* (see Eq. 1.4). The passive fibers and the Yb-doped active fiber in this architecture exhibit normal dispersion at the 1.0 μm band, D = – 40.8 ps/nm·km. To compensate this normal dispersion, the CFBG, with central wavelength $\lambda_0$ =

1060 nm, is designed to induce a net anomalous dispersion of – 0.11 ps². The dispersion management achieved between these elements leads to a net GDD of the cavity anomalous and close to zero, – 0.08 ps², which favors the stable solitonic emission regime.

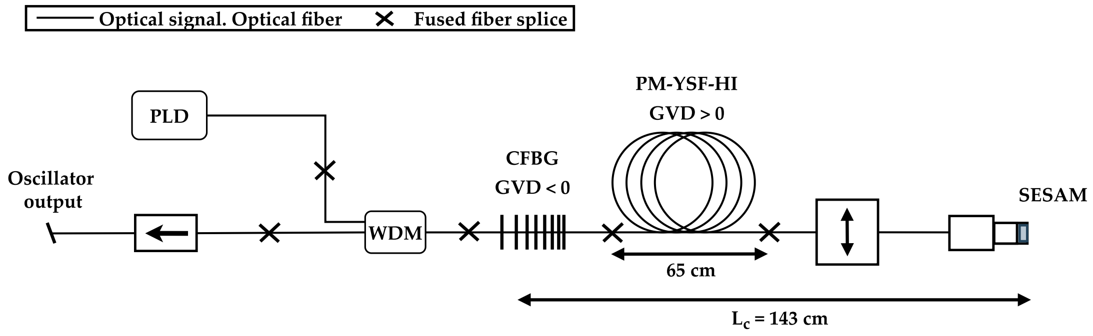


Figure 3.3. All-fiber passively mode-locked oscillator architecture. PLD: pump laser diode, WDM: wavelength division multiplexer, CFBG: chirped fiber Bragg grating, GVD: group velocity dispersion, PM-YSF-HI: Yb-doped active fiber, SESAM: semiconductor saturable absorber mirror.

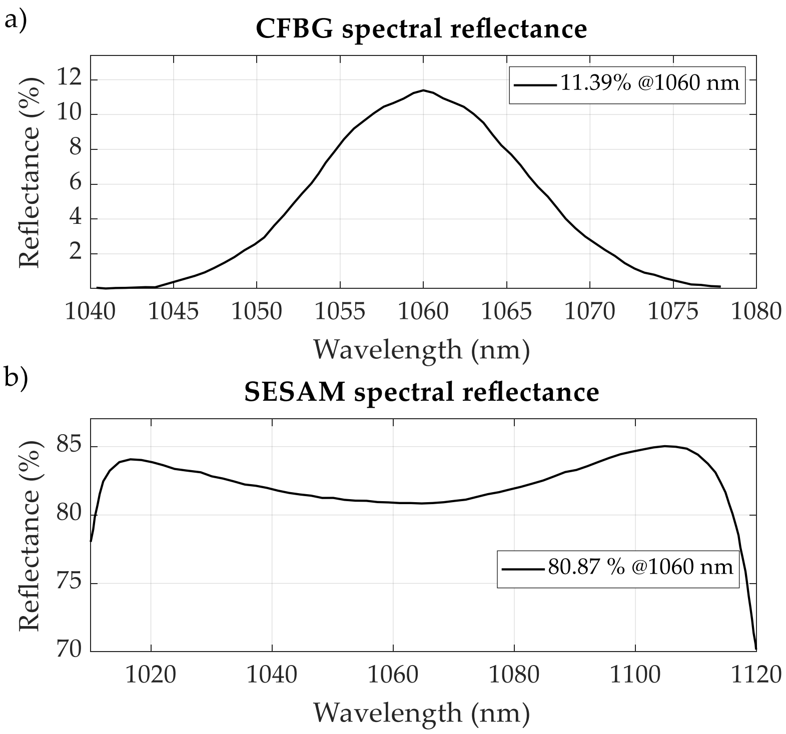


Figure 3.4. a) CFBG and b) SESAM curves of reflectance.

The light from the PLD enters the cavity through the CFBG and is propagated inside 65 cm of Yb-doped active fiber (PM-YSF-HI, Nufern). The total length of the cavity, $L_c$, is calculated so that the repetition rate of the oscillator is 75 MHz. After that, the light goes through an in-line polarizer (ILP-1064-3F-003-00-1.0-0.25-N0, RUIK) built with the same passive PM fiber as the WDM. The polarized light running through the cavity reaches the SESAM (SAM-1064-19-10ps-1.3b-0, Batop) that has 10 ps relaxation time, high reflection band from 1020 to 1100 nm (Fig 3.4 b)), 13 % modulation depth and 90 μJ/cm$^2$ saturation fluence. The SESAM comes as an unmounted square that we place in direct contact with the surface of the FC/PC (ferrule connector/physical contact) output connector of the polarizer. When the pulses generated in the cavity are reflected by the SESAM they travel back to the CFBG and ~ 90 % of the light power is transmitted to the WDM. A high power fiber-pigtailed polarizing isolator (HPMIS-1064-SF-003-011-NN-0510, RUIK) that can support optical powers up to 5 W is spliced at the output port of the WDM where the light from the cavity exits the oscillator. Before splicing the output fiber from the isolator to the following stage, the emission obtained from the all-fiber passively mode-locked oscillator of stage 1 is characterized at different pumping currents of the PLD. This way, we find the range of currents for which the oscillator shows self-starting behavior and stable pulse emission, corresponding to ~ 75 – 100 mW optical output power of the PLD. At the pumping current at which the emission is observed to be in a stable single-pulse regime, the spectrum has 13.6 nm bandwidth at full width at half maximum (FWHM) and the pulse width at FWHM is 3.1 ps. This width does not correspond to the Fourier limit of the pulses because they are temporally stretched by the dispersion induced during their propagation through the output fibers of the oscillator. The average power and the peak power obtained at the output of this stage are 20 mW and 86 W, respectively.

The output fiber of the oscillator is spliced to the input fiber of the second stage, the stretcher. The goal of this stage is to temporally stretch the output pulses of the oscillator and to obtain a normal net dispersion that will be later compensated with the anomalous dispersion introduced by the fiber compressor (stage 4). Since the oscillator and the amplifying stage are built with fibers that present normal dispersion (GVD > 0) at 1060 nm, a passive fiber (PM980-XP, Thorlabs) of normal dispersion is used as stretcher. This fiber has a 6.2 μm mode field diameter (MFD). We use 20 m of PM980-XP, a length calculated to increase three times the pulse duration so as to pre-compensate the anomalous dispersion that the pulses will experience in the compressor stage. The stretching fiber is then spliced to a FFC (2-M02-P02-P02-0-1, Gould Fiber Optics) that combines in a common output the 1060 nm emission from the stretcher and the 976 nm emission of a PLD (K976AB2RN-8.000W, BWT Beijing). The characterization of this stage is performed with the PLD current set to 0 A (no emission from this diode) and keeping constant the pump current of the PLD of stage 1. The spectrum remains with the same 13.6 nm bandwidth at FWHM, the pulse duration is increased to 9.6 ps and the average output power is 16 mW. The peak power decreases to 22 W.

The third stage, which is the amplifier, receives the light coming from the stretcher and sends it through 4.5 m of a double clad Yb-doped active fiber (PM-YDF-5/130-VIII, Nufern) with 6.2 μm MFD. The pumping light sent through the passive cladding of the active fiber excites the dopants of its core and the light coming from the stretcher is amplified. A study of the spectrum at different pumping currents of the amplifier is performed to find the maximum current that can be reached before inducing NLE. Then, a characterization of the pulses at the output of the amplifier with 3.75 W pumping power is performed. The spectrum is slightly wider than that of the previous stage, with 14.5 nm bandwidth at FWHM, while the temporal pulse width is 15 ps. The average output power is increased by the amplifier to 850 mW, so the peak power and peak intensity are also increased to 756 W and 2.50 GW/cm$^2$, respectively.

The last stage of the seed of the all-fiber source is the compressor, which is based on HC-PBG fiber technology. The microstructured fiber used in this stage to temporally compress the pulses without inducing NLE (HC-1060, Thorlabs) presents anomalous GVD with a value of – 0.072 ps$^2$/m and has a higher MFD than the fibers of the previous stages, 7.2 μm. Its length is calculated in order to obtain a slightly anomalous net GDD, so 10 m of this fiber result in – 0.015 ps$^2$ net GDD. In that case, the pulses will still experience compression in the first segment of the ANDi PCF and SPM efficiency will be optimized by having the maximum peak power achievable inside the ANDi PCF. The pulses finally delivered by this stage are compressed down to 200 fs temporal width at FWHM while maintaining the 14.5 nm bandwidth at FWHM. The measurement of the spectrum at different amplifier pumping currents is shown in Fig. 3.5. It can be observed that the spectral shape suffers negligible broadening while the pulse propagates through the fiber compressor, not even for the maximum pump current (5 A, corresponding to the 3.75 W pump power). The average output power is 650 mW, but the peak power and intensity are two orders of magnitude higher than in the previous stage with values of 43.3 kW and 106.3 GW/cm$^2$, respectively. With such pulses, SC can be efficiently generated in few tens of centimeters of the ANDi PCF.

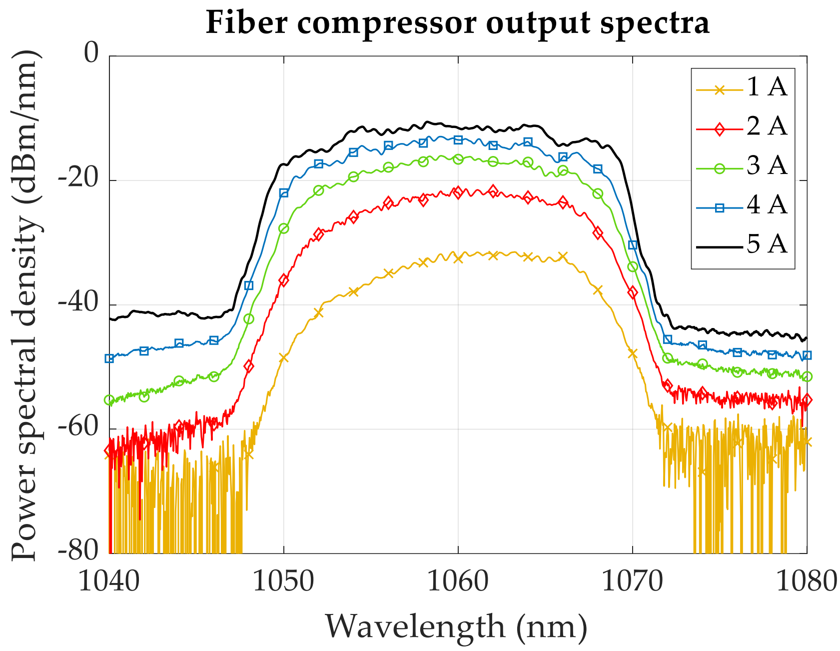


Figure 3.5. Spectra of the seed at the output of the fiber compressor stage for different amplifier pumping currents.

### 3.1.2. SC generation stage: ANDi PCFs design, fabrication and optimization

The seed architecture explained in subsection 3.1.1 delivers output pulses of 200 fs pulse temporal width at FWHM and 106.3 $GW/cm^2$ peak intensity as pumping light to excite the NL stage where the SC generation happens. The ANDi PCF used for this last stage of the all-fiber source was chosen and optimized after a diagnosis of different emission regimes depending on the fiber geometry. The design and fabrication process, explained throughout this subsection, was carried out in collaboration with XLIM (Limoges, France) and Dr. Oleksiy Shulika (University of Guanajuato). Dr. Shulika designed the geometric structure of the PCFs and calculated their dispersion curves, and the research group of Professor Philippe Roy at XLIM was in charge of manufacturing the fibers.

The ANDi PCF is manufactured with F300 silica and the design of its microstructure is based in the standard solid core geometry presented in Fig. 1.3: a solid core that results from a missing hole and that is surrounded by a number

$N_r$ of rings of holes running along the longitudinal axis of the fiber in a hexagonal array. The microstructure of air holes is wrapped by a jacket of uniform silica that confers the fiber a typical diameter of 125 μm. Efficient confinement of the light inside the core is obtained for $N_r = 7$. Parameters $d$ and $\Lambda$ have to be designed taking into account the requirements for the dispersion curve to obtain temporally coherent SC within 400 nm spectral bandwidth centered at 1060 nm, and they have to fall within the technological limits of feasible manufacturing. Not all technologies allow fabricating PCFs with air holes of very small diameter and, more importantly, guarantee the stability of the structure along hundreds of meters and their reproducibility. Controlling the shape and homogeneity of $d$ is often the main issue in the PCF drawing process. Therefore, we set the hole diameter as the independent parameter during the dispersion curve designing process, choosing a minimum and maximum $d$ of 500 and 4000 nm respectively. Related to that range, $\Lambda$ is defined so that the ratio $d/\Lambda$ is within the interval 0.2 – 0.8. In this way, single-mode (SM) behavior is guaranteed for values of $d/\Lambda \leq 0.43$ [132,133]. When $d/\Lambda > 0.43$ the fiber could show either SM or multi-mode behavior. In order to have relatively symmetric spectral broadening it is desirable to also have a dispersion profile $D(\lambda)$ as symmetric as possible relative to the excitation wavelength $\lambda_0$ [134]. It is also required to have a dispersion as small as possible in absolute value to guarantee that SPM will be the dominating spectral broadening mechanism. Setting these conditions, a set of potentially valid dispersion curves is obtained for values of $d$ and $\Lambda$ contained within the ranges d = [0.50 ; 0.64] μm and Λ = [1.50 ; 1.70] μm. We scan the resulting (d, Λ)-space applying two different conditions for the maximum dispersion, $D_{max} \equiv D(\lambda_{max})$: it has to occur at a $\lambda$ value within the laser bandwidth, $\lambda_{max} \in \Delta\lambda$, or to a slightly more extended range, $\lambda_{max} \in \Delta\lambda \pm 15$ nm. Said bandwidth is the output bandwidth at FWHM of the spectrum at the output of stage 4 (temporal fiber compressor), $\Delta\lambda$ = 14.5 nm (1060 ± 7.25 nm). The dispersion curves are calculated using the semi-empirical model proposed by Saitoh et. al. [135] and applying the theory of SM optical fibers to describe dispersion properties of solid core PCFs. The fact that the model is semi-empirical allows to iterate over a large volume of parameters to filter out designs fitted to technical requirements. With this method we obtain a map of $d$ and $\Lambda$ pairs (Fig. 3.6) where the filled purple area corresponds to the stricter condition $\lambda_{max} \in \Delta\lambda$, while the holey blue region extends the condition to a broader bandwidth. The yellow diamond points the target design while the variety of black squares corresponds to different (d, Λ) pairs whose dispersion curves are shown in Fig. 3.7.

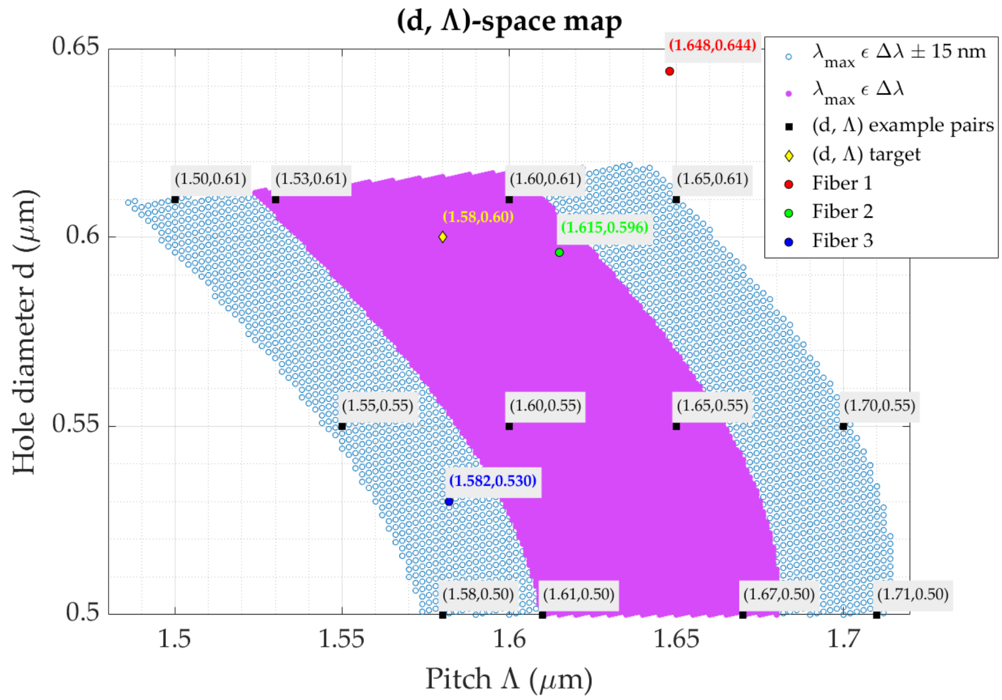


Figure 3.6. Map of acceptable maximum dispersion, $D_{max}$, as a function of the PCF geometrical parameters.

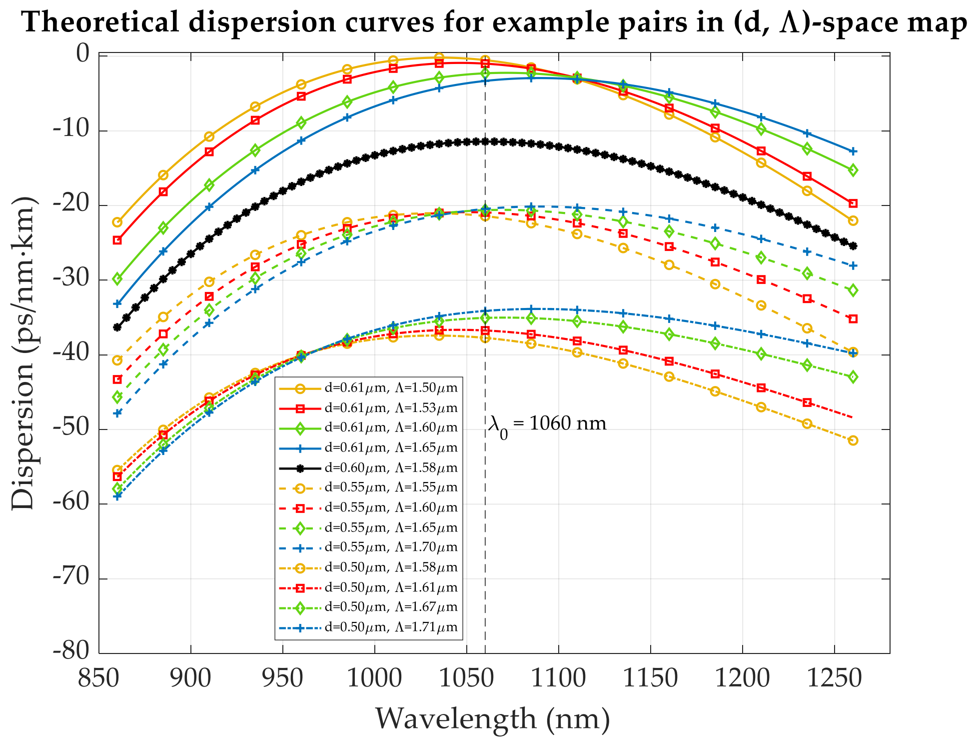


Figure 3.7. Corresponding theoretical $D(\lambda)$ curves of ANDi PCFs with (d, Λ) pairs shown in the map of Fig. 3.6.

For the several (d, Λ) pairs marked in Fig. 3.6 we study the differences in their dispersion curves depending on the hole diameter and on the pitch. Firstly, we can observe that a change in *d* is clearly associated with a displacement in the value of $D_{max}$. While all the groups of curves for every *d* remain below D = 0 ps/nm·km, for smaller diameters the value of $D_{max}$ is also lower. Regarding the change in *Λ*, what we can see is that a change in the curvature is induced when the value of the pitch is changed. For higher values of *Λ* the slope of the curves is also higher and depending on the hole diameter the wavelength at which the curve remains constant is different: for smaller *d* said wavelength is also lower. By studying these effects that *d* and *Λ* have in the dispersion curves we estimate a target geometrical design with a theoretical dispersion curve that fulfills the previously imposed conditions for the desired ANDi PCF (black curve in Fig. 3.7). This way, the suitable design for the ANDi PCF is set as the aim and the fabrication is carried out with well-defined pairs of *d* and *Λ* near said suitable geometrical parameters.

Among the fabrication methods developed to manufacture PCFs, we used the standard stack and draw method [38,43]. In this case, 168 capillaries of 1 mm outer diameter are stacked together around a solid rod of 1 mm diameter. In a first step said stack is introduced and chocked in an outer tube that will be part of the outer cladding of the final fiber. This is how the primary preform is fabricated, which is then drawn into several 1 m long microstructured capillaries (or canes). This step is achieved by applying vacuum into interstitial holes while keeping the 168 inner holes of the canes at atmospheric pressure. Afterwards, one of these microstructured canes is introduced into a jacket tube to reach the expected outer diameter, *Λ* and *d* ranges during the final drawing. Finally, the fine control over *d* and *Λ* is obtained by controlling the following parameters: the furnace temperature, the preform and drawing speeds, and the pressure applied to the holes. Despite the high quality of the control devices and of the regulation of the electronic systems of the drawing tower, stabilizing and controlling the size of the small holes with values of *d* of 500 – 600 nm with an expected accuracy of 50 nm is challenging, especially achieving repeatability from a drawing to another. In fact, repeatability and the fine control of *d* can be influenced by many factors as, for example, micro-geometrical fluctuations along one tube or between external tubes (second drawing step) or residual material stress and geometrical fluctuations between microstructure capillaries (first drawing step). One way to attempt to overcome the impact of said factors is to experimentally test the PCFs during the drawing process. From every 500 m of fiber with fixed drawing parameters, we collected 1 m long fiber samples and then excited them by launching the kW-range peak power pulses of the all-fiber seed in order to observe the signature of the NL mechanisms at the output of the ANDi PCF. Those signatures are deeply related (as explained in the introduction of this thesis) with the shape of the dispersion curve of the ANDi PCF. When having anomalous dispersion, the output spectrum is expected to show asymmetric spectral broadening due to modulation instability, soliton fission and Raman-induced frequency shift. On the other hand, when having ANDi curves but far from zero and exhibiting fast variations of group velocity over the spectral band of interest, the shape of the spectrum is triangular and broadening efficiency is low. In between these two different $D(\lambda)$ curves, an ANDi curve with a flat top near zero leads to the kind of symmetric efficient broadening achieved by pure SPM contribution. Thus, an estimation of $D(\lambda)$ can be done through this observation establishing a relation between the observed spectra and the parameters of each sample, $d$ and $\Lambda$, that are experimentally measured with a scanning electron microscope (SEM). This way, the optimized geometrical parameters of the fiber are defined and the pressure applied in the preform is tuned during the optimization of the manufacturing process to reach said pair of parameters. In order to obtain samples with stabilized geometrical parameters, the inertia of the process requires to wait for several minutes (corresponding to approximately several hundreds of meters of drawn fiber) although the applied changes in pressure are as small as 0.1 kPa for a total applied pressure from 12 to 15 kPa depending on the drawn preform and samples.

In the case of our source, several samples of the manufactured PCF were excited with the all-fiber seed explained in subsection 3.1.1 throughout the optimization process. Fig. 3.8 summarizes the live tests performed to three representative samples named fiber 1, 2 and 3, which are tagged in the (d-Λ)-space map of Fig. 3.6. It shows the SEM image of the cross section of each 20 cm piece of fiber (Fig. 3.8 a.1)-a.3) insets) and their associated theoretical dispersion curve (Fig. 3.8 a.1)-a.3)), against the spectra obtained for each one of them at different amplifier pumping currents when the pieces are excited with the pulses delivered by stage 4 of the all-fiber seed (Fig. 3.8 b.1)-b.3)). 2.0 A, 4.5 A and 5.0A currents for the PLD used in the amplifying stage translate into 1.3 W, 3.3 W and 3.75 W of average pump power, respectively.

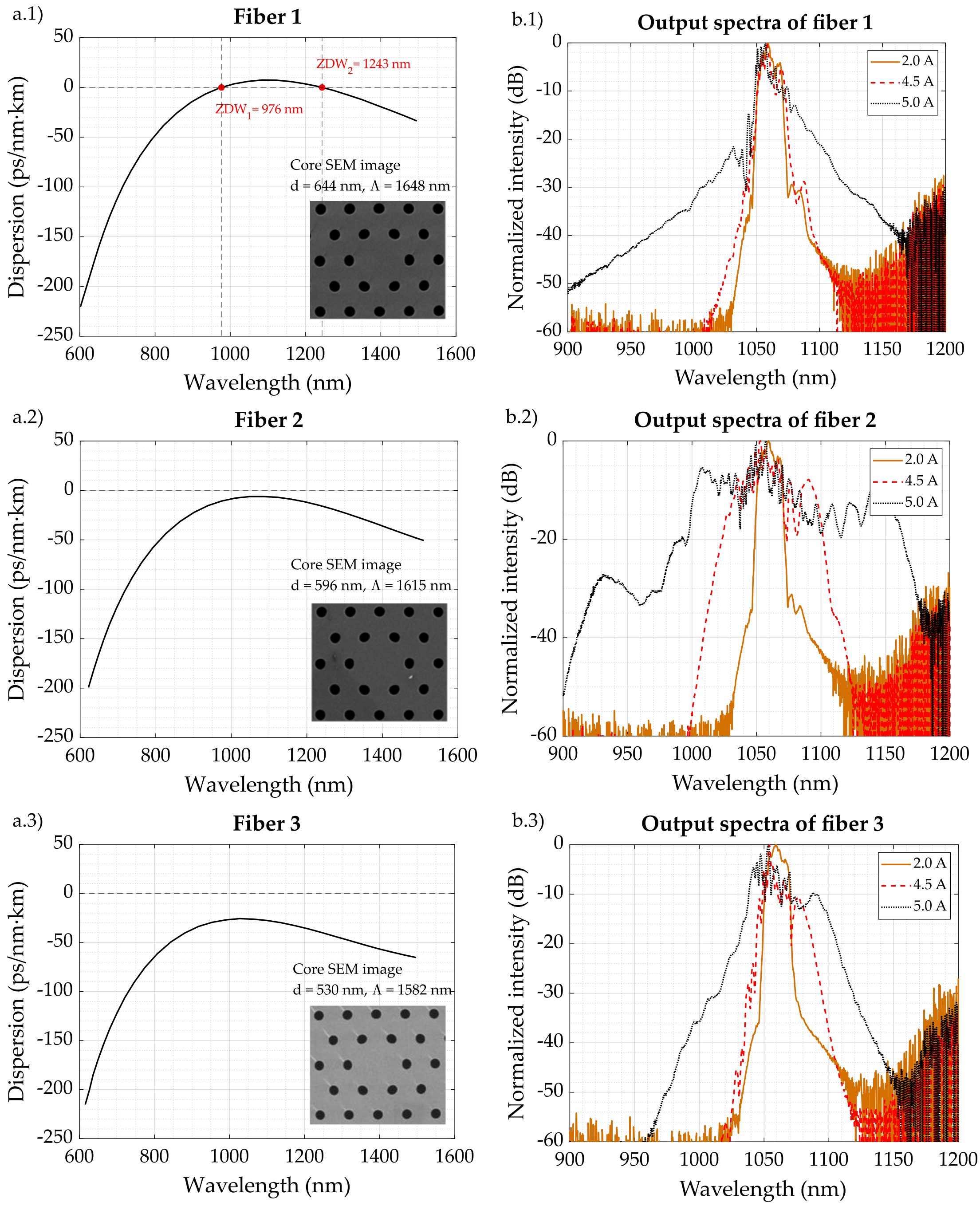


Figure 3.8. Summary of properties of fibers 1, 2 and 3. a.1) – a.3) Calculated dispersion curves and (insets) detailed scanning electron microscope (SEM) images of the core region. b.1) – b.3) Optical spectra at the output of 20 cm of each ANDi PCF with pump powers of 1.3 W (2.0 A, solid yellow line), 3.3 W (4.5 A, dashed red line) and 3.75 W (5.0 A, dotted black line).

With the results obtained from these measurements we can observe that fiber 1 presents a dispersion curve out of the target of ANDi condition (Fig. 3.8 a.1)), being the dispersion parameter D ∈ [0 ; + 5] ps/nm·km within the exciting laser bandwidth. This corresponds to the kind of spectral broadening governed by temporally incoherent dynamics, which can be observed in Fig. 3.8 b.1) and it occurs when hole diameters are too large (e.g., larger than 630 nm, for a pitch of 1650 nm) as is the case of the core region shown in the inset of Fig. 3.8 a.1): d = 644 nm and Λ = 1648 nm. Contrarily, fiber 2 presents an ANDi curve (Fig. 3.8 a.2)), being the dispersion parameter D ∈ [- 25 ; - 5] ps/nm·km within a full bandwidth of 300 nm centered at $\lambda_{max}$ = 1060 nm. In this case, as can be seen in Fig. 3.8 b.2), the evolution of the spectral broadening is symmetric and temporally coherent as it is governed by SPM. Due to the near-zero dispersion of this ANDi PCF the pulse temporal stretching is limited, resulting in high SPM efficiency. The average pump power of 3.75 W is slightly above the limit below which spectral broadening is due to SPM only. Indeed, the optical wave-breaking (OWB) effect (which is a kind of FWM effect [98]) that typically broadens the spectrum further into the short wavelengths, also appears here and is manifested through the shoulder peak observed at 930 nm. To maintain temporally coherent spectral broadening given only by SPM, it is necessary to avoid OWB effects. In the inset of Fig. 3.8 a.2) we can see that this kind of dispersion curve leading to a spectral broadening driven by SPM appears at lower values of *d* and *Λ* compared to those of fiber 1: d = 596 nm for Λ = 1615 nm. Finally, fiber 3, as fiber 2, also presents an ANDi curve (Fig 3.8 a.3)), being D ∈ [- 40 ; - 25] ps/nm·km within a full bandwidth of 300 nm, centered at $\lambda_{max}$ = 1045 nm. These values are further from a zero-dispersion value than those of fiber 2. Consequently, SPM still broadens the spectrum while preserving temporal coherence, but with less efficiency than the case of fiber 2 due to the larger temporal stretching that the pulse suffers in fiber 3. This happens when the geometrical parameters are even lower than for fibers 1 and 2. The core region of fiber 3 is shown in the inset of Fig. 3.8 a.3), where the measured values of its parameters are d = 530 nm and Λ = 1582 nm. Furthermore, despite choosing $N_r$ = 7 to minimize confinement losses, the small ratio d/Λ = 0.33 of this pair of parameters induces larger confinement/bending losses to the fundamental mode.

### 3.1.3. Optimized ANDi PCF exciting stage

Once the optimized fiber is manufactured, it is selected as the ANDi PCF for the last stage of the all-fiber source, stage 5 of Fig. 3.1. Its characteristics are d = 596 nm and Λ = 1615 nm, D ∈ [- 25 ; - 5] ps/nm·km within a full bandwidth of 300 nm centered at $\lambda_{max}$ = 1060 nm and 2.6 μm MFD.

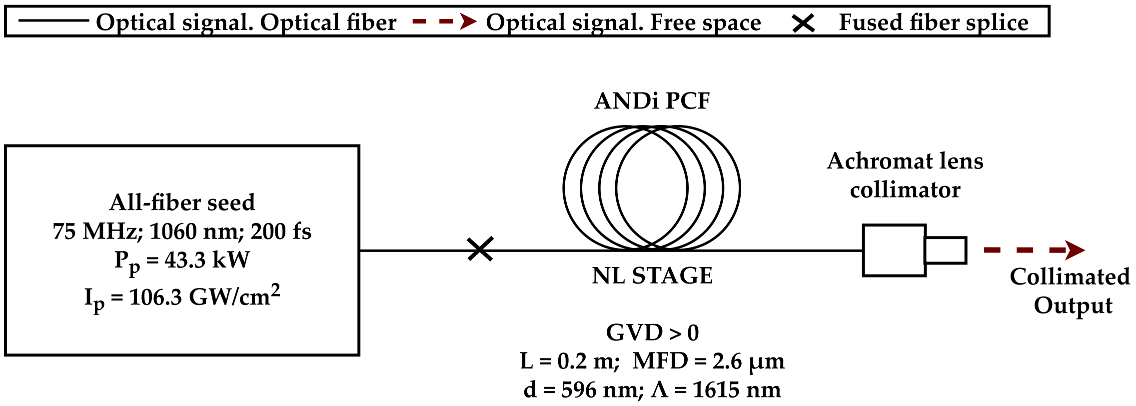


Figure 3.9. Scheme of the all-fiber seed pumping the last stage of the all-fiber source through a fusion splice.

In order to excite this fiber with the pulses coming from the all-fiber seed maintaining an all-fiber configuration, the end of the HC-PBG fiber of stage 4 is spliced to the ANDi PCF of stage 5 (Fig. 3.9) through a weak splice to maintain the integrity of the structure of both fibers. Due to the differences in the MFD between both fibers (7.2 µm and 2.6 µm, respectively), the arc discharge parameters which determine the coupling efficiency when splicing fibers cannot be set with standard values for fibers with matching MFDs. Therefore, we carried out an optimization process to find the arc discharge parameters that maintained the fibers spliced for the maximum achievable coupling efficiency [136], which was of 0.4. Trying different values of the current applied to the arc and the duration of the discharge, the optimized respective values are ~ 9 mA and ~ 0.5 s. Said values are found to be ~ 6 mA and 1.5 s lower than that of a conventional fusion splice between standard 125 µm SM fibers (SM-SM Basic mode of Fujikura FSM 100 P splicer). Finally, the output of the fiber is a home-made endcap. First, the end of the fiber has to be cleaved in angle to reduce as much as possible the risk of having large back-reflections that the isolators could miss. Then, we collapse the holes of the ANDi PCF with an arc discharge of the fusion splicer. Once the endcap is made, its output beam is collimated to a 1 mm-diameter beam spot with an achromat lens (60FC-4-M12-08, Schäfter & Kirchhoff) with 12 mm focal length and anti-reflection coating from 980 to 1550 nm. Fig. 3.10 shows the generated SC measured at the collimated output of the system together with the output spectrum of the previous stage for comparison before and after the ANDi PCF.

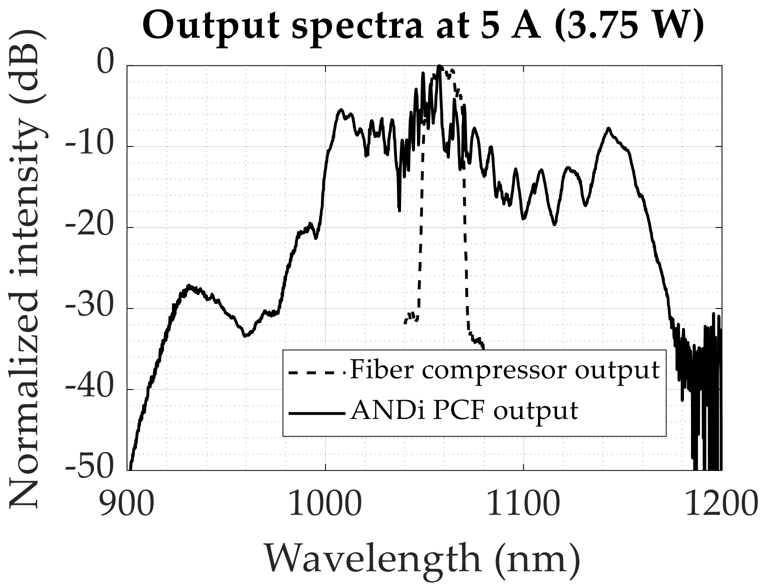


Figure 3.10. Comparison between spectra of stage 4, fiber compressor (dashed line), and stage 5, ANDi PCF, measured at the collimated output of the system (solid line).

## 3.2. Few-cycle pulse compression and optimization

In section 3.1 the few-cycle all-fiber SC has been explained. By few-cycle all-fiber SC we refer to an all-fiber configuration that generates temporally coherent pulses compressible to transform-limited few-cycle duration. This does not imply that few-cycle duration is necessarily happening at the very output of the all-fiber configuration. In fact, getting few-cycle duration at the output of the all-fiber architecture is not an actual advantage since such short pulses always require dispersion pre-compensation before reaching their target (either by free-space or fiber compression means). Hence, we have previously introduced the first part of the system where an all-fiber source generates temporally coherent SC emission, and now the last compression stage is explained in this section.

A free-space temporal compressor of fixed anomalous dispersion and variable normal dispersion is the last stage of the whole system, stage 6. It is designed to compress the temporally coherent pulses of the all-fiber source down to close to their Fourier limited duration of 12.2 fs. The compressor consists of a pair of glass wedges and a pair of chirped mirrors placed in the path of the optical signal to introduce normal and anomalous dispersion respectively. They are designed to compensate the dispersion that the pulse suffers during free-space propagation before it arrives to its target, which will be at a different distance from the output fiber depending on the application. In order to provide the adjustment of said dispersion, the pair of glass wedges is built within a motorized positioner. Thus, dispersion is varied by changing the relative position (insertion length) between the wedges, i.e., changing the amount of glass material effectively traversed by the optical signal. Aiming for a range of net GDD from – 1000 fs$^2$ (0 mm insertion length) to + 1500 fs$^2$ (17 mm insertion length), using BK7 glass, the design of the compressor is defined in collaboration with Dra. Rosa Romero, Dr. Paulo T. Guerreiro, Dr. Miguel Miranda and Dr. Helder Crespo from the company Sphere Ultrafast Photonics [85] (Fig. 3.11). The output pulses of the few-cycle all-fiber SC source are sent to the compressor, which is adjusted to achieve the best quality pulse: the shortest temporal pulse width at FWHM with the highest peak power ratio (PPR) between the main peak and side-lobes.

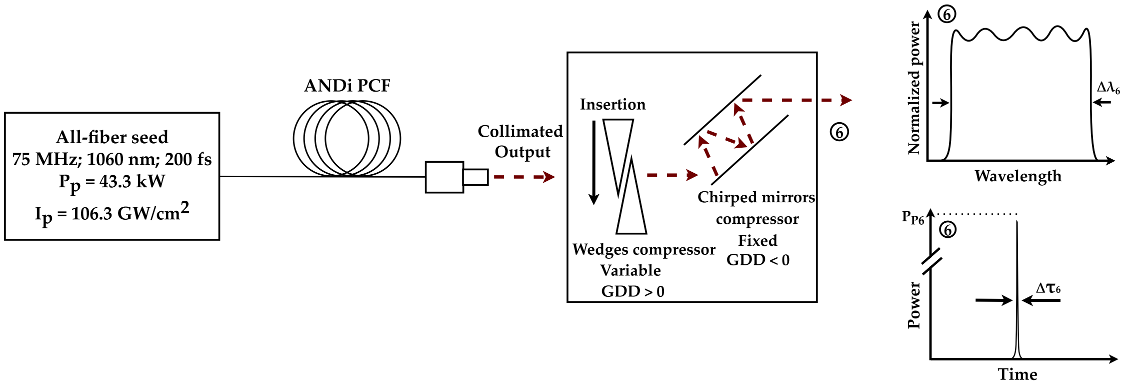


Figure 3.11. Free-space compressor, stage 6, in the optical path of the few-cycle all-fiber SC source output pulses and qualitative representation of their spectral and temporal properties.

To confirm that they are actually compressible to their FTL, two different methods of pulse characterization in the time domain are carried out to compare their results: d-scan technique [137] and interferometric autocorrelation [138]. The d-scan technique is based on performing a dispersion scan to the pulses with the previously described pulse compressor, while measuring the spectrum of the second-harmonic generated (SHG) signal. From this measurement, the phase and the amplitude properties of the electric field of the pulses are retrieved as explained in reference [137]. Fig. 3.12 a) and b) show the measured and retrieved d-scan traces (the SHG signal intensity against wavelength and wedge insertion length) from which the spectral intensity and phase (Fig. 3.12 c)) and temporal intensity (Fig. 3.12 d)) of the electric field of the pulse are retrieved. From Fig. 3.12 d) we find that a 56 ± 4 % of the energy is contained in the main peak and PPR > 8. Table 3.1 collects all the data obtained by the d-scan retrieval regarding the spectral domain (central wavelength and high-order dispersion parameters) and the temporal domain (pulse width, FTL pulse width and wavelength at which the SHG signal shows the maximum intensity: wavelength at peak). The pulses present very low GDD, TOD and fourth order dispersion (FOD), and the measured temporal pulse width and FTL pulse width are 12.97 fs (3.7 optical cycles) and 12.23 fs, respectively.

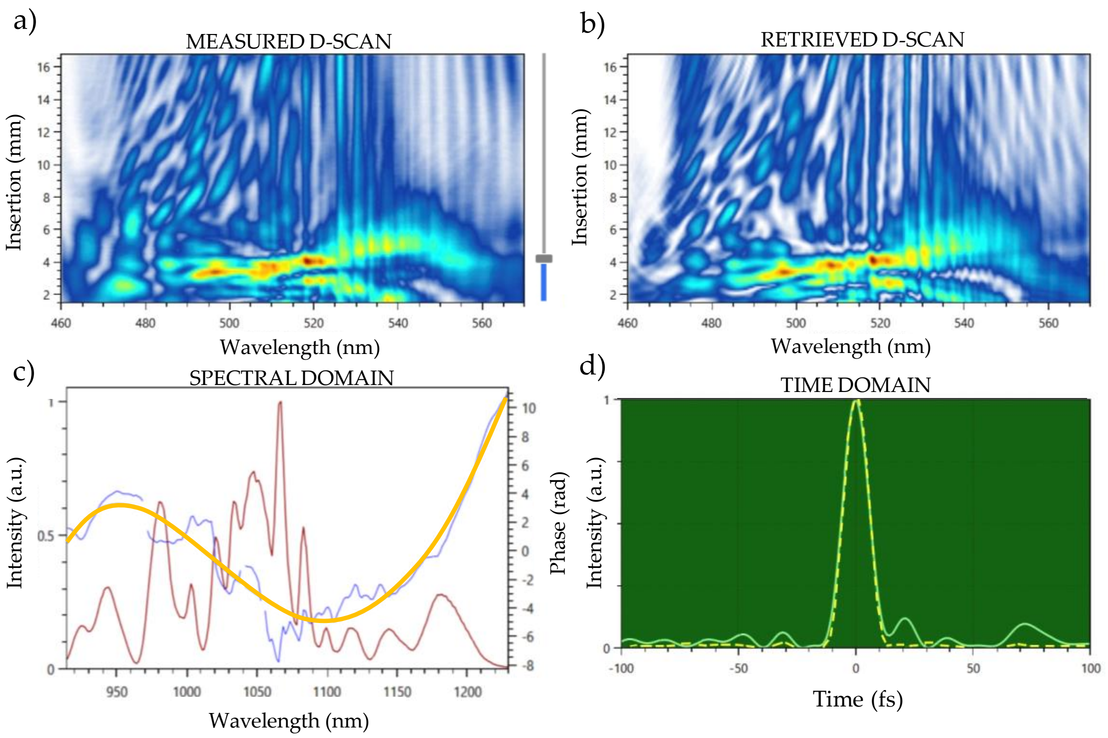


Figure 3.12. Second harmonic generation (SHG) d-scan retrieval results and resulting pulse in the spectral and temporal domains. a) Measured, calibrated d-scan trace. b) Retrieved d-scan trace. c) Measured linear spectrum (red line), retrieved spectral phase (blue line) and 4th order polynomial fit of the spectral phase (orange line). d) Temporal intensity profile of the transform-limited pulse (dashed yellow line) and temporal intensity profile of the measured pulse (light green line).

| **Spectral domain** | | **Temporal domain** | |
|---|---|---|---|
| **Central λ** | 1050.0 nm | **Pulse width** | 12.97 fs |
| **Pulse GDD** | 276 $fs^2$ | **FTL pulse width** | 12.23 fs |
| **Pulse TOD** | – 5.162 $fs^3$ | **λ at peak** | 1037.0 nm |
| **Pulse FOD** | – 1.621 $fs^4$ | | |

Table 3.1. Characterizing parameters of the pulse, obtained from the d-scan retrieval.

This result demonstrates the high degree of temporal coherence of the pulsed signal, since it is very close to the FTL duration supported by its optical spectrum (12.2 fs). The fact that the pulses are properly compressed by a compressor of negligible TOD proves that the pulses suffer very low TOD (comparable to that of the compressor) while being spectrally broadened at the ANDi PCF. This effect results from the flatness of the dispersion of the ANDi PCF (Fig. 3.8 a.2)). The pulse at the output of stage 6 (the pulsed signal compressed to its minimum duration by the compressor) is measured also with an interferometric autocorrelator. The resulting autocorrelation trace is shown in Fig. 3.13. From this trace, an estimation of the temporal width at FWHM of the pulse intensity profile of 12.6 fs is obtained. Despite not providing unambiguously the real form of the pulse intensity profile [139,140], the autocorrelation method is widely known and usually chosen as the method to measure temporal widths of pulses from light sources used in microscopy applications. As mentioned in chapter 1, NLO microscopy is the main target for the presented few-cycle all-fiber SC source. Hence, the fact that interferometric autocorrelation produces, independently from the d-scan measurement, an estimated result of the pulse width comparable to the accurate result of the d-scan method, is relevant for a straightforward use of the source in current NLO microscopy setups.

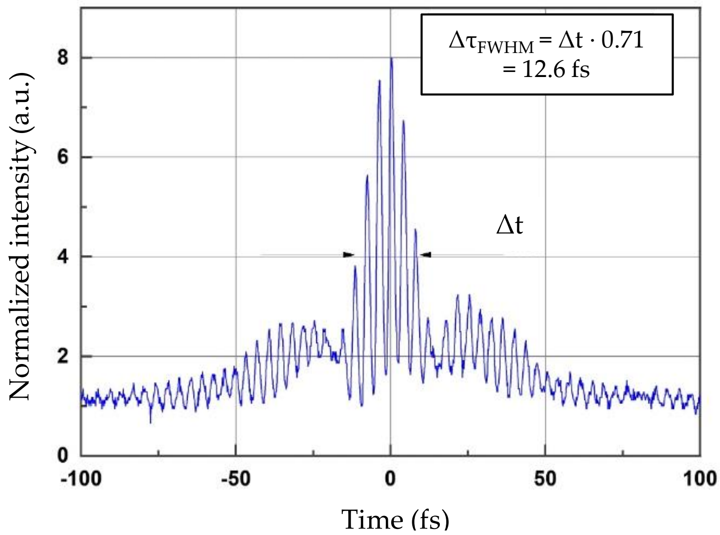


Figure 3.13. Interferometric autocorrelation trace of the pulse, compressed to its minimum achievable duration. A temporal pulse width at FWHM of 12.6 fs is estimated assuming a deconvolution factor 0.71 for a Gaussian shaped pulse.

Average and peak power of the pulses at the output of the compressor are 160 mW and 169.2 kW, respectively. The properties of the pulsed signal at the output of each stage of the system, stage 1 to 6 are summarized in Table 3.2.

| **Stage** | **$\Delta\lambda_{FWHM}$ (nm)** | **$\Delta\tau_{FWHM}$ (fs)** | **$P_{avg}$ (W)** | **$P_p$ (kW)** | **$I_p$ (GW/cm$^2$)** |
|---|---|---|---|---|---|
| **1** | 13.6 | 3100 | 0.02 | 0.086 | - |
| **2** | 13.6 | 9600 | 0.016 | 0.022 | - |
| **3** | 14.5 | 15000 | 0.85 | 0.756 | 2.50 |
| **4** | 14.5 | 200 | 0.65 | 43.3 | 106.3 |
| **5** | 150 | 80 | 0.25 | 41.7 | 784.8 |
| **6** | 150 | 12.6 | 0.16 | 169.2 | 0.021 |

Table 3.2. Properties of the pulsed signal at the output of each stage of the all-fiber source (stages 1 to 5) and at the output of the temporal compressor (stage 6) used to compress the pulse down to its Fourier limited duration. $\Delta\lambda_{FWHM}$: spectral bandwidth at FWHM, $\Delta\tau_{FWHM}$: temporal width at FWHM, $P_{avg}$: average power, $P_p$: pulse peak power, $I_p$: pulse peak intensity.

This all-fiber SC source of few-cycle (3.7 optical cycles) emission has been used as illuminating source for NLO microscopy. The experimental setup and results obtained are explained in chapter 5.

Chapter 4

# Supercontinuum generation using GRIN fibers at 1.5 μm. Study on temporal coherence

In the previous chapter we have demonstrated a few-cycle supercontinuum (SC) source in the 1.0 μm region, a wavelength region relevant to nonlinear optical (NLO) microscopy. Likewise, the 1.5 μm region, where biological tissues present more transparency [141], is also relevant to NLO microscopy in applications such as multiphoton excitation microscopy [16,142]. Ultrashort pulses at 1.5 μm can be generated from all-fiber or quasi all-fiber laser architectures through solitonic compression, chirped pulse amplification (CPA) and other techniques [66,115,143]. Research on the generation of coherent SC spectrum exciting all-normal dispersion photonic crystal fibers (ANDi PCFs) at this wavelength band has been done from a theoretical point of view. Simulations on the properties that the exciting pulses should present and how the resulting SC would be have been reported in [110,111,113]. Experimentally, though, the manufacturing process of ANDi PCFs presents some challenges when the central wavelength, $\lambda_0$, lies within the third telecommunications window. The holes of a 1.5 μm ANDi PCF require smaller diameter than those of a 1.06 μm ANDi PCF and, as explained in chapter 3, it is complicated to maintain stabilized conditions for every hole while fabricating the PCF. Also, due to the smaller size of the holes and the propagation of longer wavelengths, the efficiency of confinement of light inside the fiber during the propagation is lower within this wavelength band [144,145]. Light propagating through the interstices escapes the fiber faster than in PCFs with bigger holes and SC generation is very inefficient as shown by some numerical studies [146,147]. These difficulties are what make experimental SC generation with 1.5 μm ANDi PCFs unappealing.

Instead, we decide to use all-solid graded-index (GRIN) silica fibers to avoid PCFs high confinement losses. As explained in the introduction, GRIN fibers have a refractive index which is dependent on space along the axes which are transversal to the propagation axis. This dependence is induced by doping the silica with other elements as, for example, Ge. These fibers, which present a geometry such as that of Fig. 1.1 b), can be built with different core diameters and doping quantities to shift their zero-dispersion wavelength (ZDW) or modify their properties so as to achieve ANDi curves [148]. All-solid GRIN standard fibers present easier manufacturing conditions than ANDi PCFs through the well-known method of chemical vapor deposition [149]. Through this method, the rod of fused silica that turns into the optical fiber has its inside coated with different percentages of other elements to obtain the desired refractive index profile. Another advantage of this kind of fibers in comparison to PCFs is that thanks to their structure they are not as fragile, so fusion splice of the fiber with other standard fibers is easier to achieve while maintaining its integrity during the process.

These reasons are what lead us to design a monolithic fiber (MF) laser source of SC spectrum, pumping GRIN fibers with a seed based on an all-fiber passively mode-locked oscillator centered at $\lambda_0$ = 1535 nm. This chapter is divided into sections 4.1, 4.2 and 4.3, dedicated to the description of the source used as seed, the experimental results exciting different kinds of GRIN fibers and the study of the temporal compression and degree of coherence of the output emission of the source, respectively.

## 4.1. Architecture of the MF seed

In Fig. 4.1 this MF SC source at 1.5 μm is presented as an MF seed exciting a nonlinear (NL) stage based on GRIN fibers. The seed is designed to generate pulses of a temporal width at FWHM of ~ 100 fs and > 1.5 W average output power. The train of pulses is generated from an all-fiber passively mode-locked oscillator with a repetition rate of 1.30 GHz. Upon said train of pulses we apply amplitude modulation through a modulation setup to obtain MHz-range repetition rates that increase the peak power of the output pulses. A selectable repetition rate allows to observe how the broadening of the spectrum in the NL stage is produced depending on the input conditions of the train of pulses, i.e., for different peak power input values. Subsections 4.1.1 and 4.1.2 explain in detail the architecture of the different stages of the MF seed, how the modulation is performed and the characteristics of the output pulses used as pump of the NL stage.

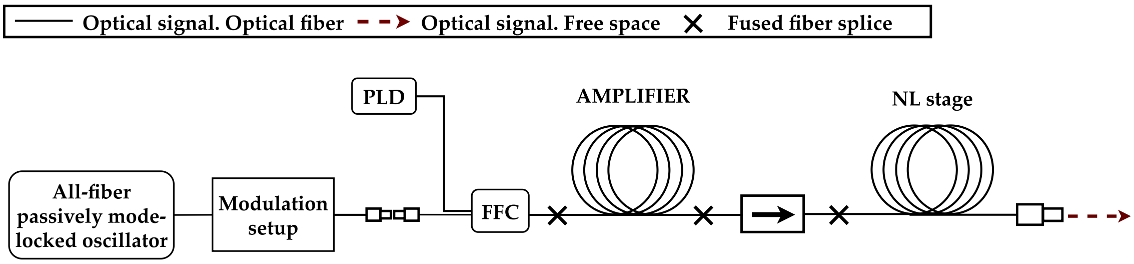


Figure 4.1. Architecture of the monolithic fiber laser source of SC at 1535 nm central wavelength. PLD: pump laser diode, FFC: fused fiber combiner; NL: nonlinear.

### 4.1.1. Modulation of a high repetition rate oscillator

Typically, the kind of fiber lasers of ultrashort pulses that are designed to be used as excitation for NL fibers to generate SC have repetition rates of the order of megahertz. This is convenient since lower repetition rates, for a same value of average output power and temporal width of the pulses, imply higher peak power values. Hence, nonlinear effects (NLE) are more likely to be induced in the fiber and SC can be expected to be generated more efficiently. However, SC spectra generated from trains of pulses of higher repetition rates as gigahertz instead of megahertz present higher average power for a same value of pulse energy. This is convenient for microscopy applications since the free-space optics used in microscopy setups introduce a high amount of losses. Also, the imaging integration time is lower for higher average power levels. In order to benefit from the advantages posed by both ranges, megahertz and gigahertz repetition rates, it is possible to work with a high repetition rate oscillator and easily decrease its natural frequency through modulation techniques. Thus, we decide to use cavities of 1.30 GHz with a passively mode-locked fiber laser previously developed at FYLA [150].

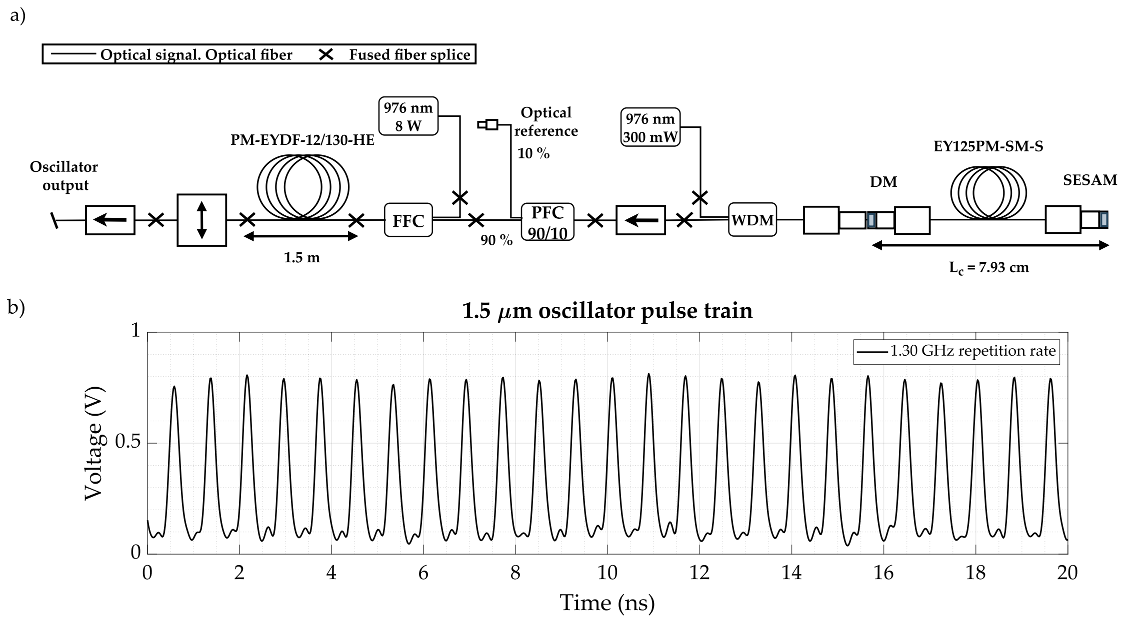


Figure 4.2. a) Architecture of the 1535 nm all-fiber passively mode-locked oscillator. b) Photodetected train of pulses from the optical reference. PM-EYDF-12/130-HE: Er/Yb-doped active fiber of the pre-amplifying stage, EY125PM-SM-S: Er/Yb-doped active fiber of the cavity.

This laser, which is the oscillator of our seed (Fig. 4.2 a)), is built as follows: light coming from a pump laser diode (PLD) at 976 nm is sent through a wavelength division multiplexer (WDM) to a linear cavity of length $L_c$ = 7.93 cm. This light travels back from the end of the cavity, a semiconductor saturable absorber mirror (SESAM) of high reflectance at 1.5 μm acting as one of the reflectors. Therefore, the total length traveled by the generated pulses is 15.86 cm, which corresponds to 1.30 GHz repetition rate according to Eq. (4.1) for silica fibers (refractive index 1.45 [31]).

$$f = \frac{c}{2 \cdot 1.45 \cdot L_c} \tag{4.1}$$

where $f$ is the repetition rate of the cavity, $c$ is the speed of light traveling through vacuum and $L_c$ is the length between the reflectors of the cavity. Part of the laser light that returns from the SESAM exits the cavity through the reflector acting as output coupler, a dichroic mirror (DM) of 99 % reflectance at 1535 nm. Using a DM allows to build a short cavity just from the Er/Yb-doped active fiber used as active medium. A polarization maintaining filter coupler of ratio 90/10 (PFC90/10) is used to obtain an optical reference which is a replica of the output of the cavity (10 % of the total of pulses). The other 90 % of the pulses generated in the cavity are then sent to a fused fiber combiner (FFC) spliced to an 8 W PLD at 976 nm to be amplified through 1.5 m of a double clad Er/Yb-doped active fiber. After this fiber, at the output of the oscillator, an in-line polarizer is placed to obtain a linearly polarized output. At 4.0 A (2.3 W) of PLD current, the average output power, temporal pulse width at FWHM and spectral bandwidth at FWHM of this oscillator are 168 mW, 2.5 ps and 2.0 nm, respectively. Fig. 4.2 b) shows the train of pulses measured with a photodetector of 5 GHz bandwidth at the optical reference. After the oscillator, previous to the amplifying stage, we modulate the frequency of the train of pulses using a pattern generator (86130A BitAlyzer, Agilent) and a Mach-Zehnder modulator (MZM) (MX10B, Thorlabs) (Fig. 4.3 a)). Dividing the natural repetition rate of the oscillator we are able to excite the NL stage with repetition rates in the MHz-range, average output powers in the range of watts, and peak power values in the kW-range. The pattern generator receives as input the photodetected signal of the optical reference. From that reference, the pattern generator is synchronized with the train of pulses of the oscillator. Then, we define the pattern that the MZM follows to modulate the train of pulses. The intensity modulation that it applies to the train results in the elimination of a certain number of pulses according to the goal repetition rate. Adjusting the bias voltage of the MZM we set the right point were the minimum modulation applied coincides with the maximum amplitude of the pulses so that every allowed pulse is transmitted without being clipped. In this work of thesis we have used two different modulation patterns for the division of the repetition rate, with a 1/2 ratio and a 1/3 ratio, respectively, thus setting 650 MHz and 434 MHz repetition rates for the trains of pulses to be used as excitation of the NL stage of the source. Both photodetected trains of pulses are shown in Fig. 4.3 b.1) and b.2).

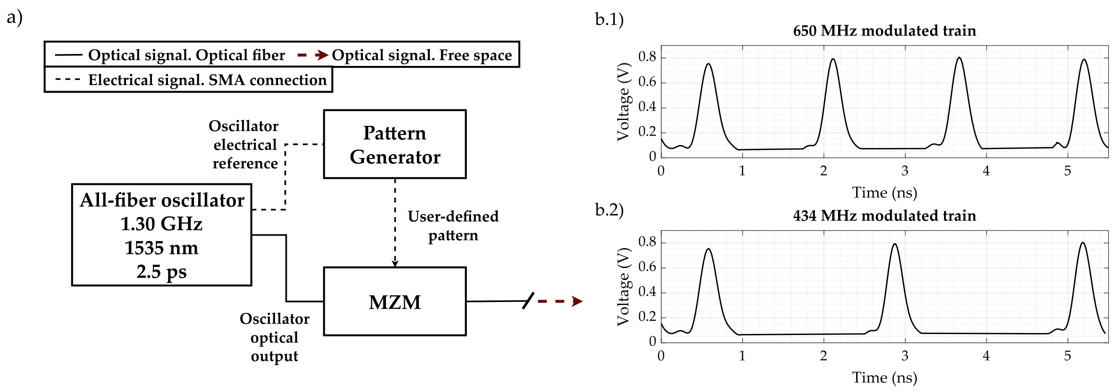


Figure 4.3. a) Scheme of the oscillator of the MF seed when its output signal is modulated. b.1) and b.2) photodetected trains of pulses modulated to 650 and 434 MHz repetition rates, respectively. SMA: SubMiniature version A.

Finally, the pulses obtained at the output of the MZM need to be amplified (from few mW to > 1.5 W average power) and compressed (from few ps to ~ 100 fs duration) prior to be sent as excitation light into the NL stage.

### 4.1.2. Amplifying stage: design and characterization

The pulses coming from the MZM output have the desired repetition rate but not the temporal width and average output power levels required to nonlinearly excite the GRIN fibers of core diameters around 5 – 7 μm. Therefore, to amplify the emission from the previous stage, we lunch the light of an 18 W PLD at 976 nm (K976AA2RN-18.00W, BWT Beijing) through an FFC (MPC-021-051-1-051-D5-0-0.8-100-25, RUIK) and 4 m of a double clad Er/Yb-doped active fiber (PM-EYDF-6/125-HE, Coherent). The light coming from the optical output of the MZM is sent to the FFC through their FC/PC (ferrule connector/physical contact) connectors instead of splicing the fibers (Fig. 4.1). Facing the output surfaces of the two connectors allows us to amplify the pulses of the oscillator with or without the modulation setup: we can insert the output connector of the oscillator straight to the amplifier or make it go through the MZM and introduce the output connector of the modulator in the amplifier. Either way, the amplified signal is delivered through a high power polarizing isolator (up to 5 W) (HPMIS-1535-DF-001-10-0.8-11-1020, RUIK). Since the dispersion sign of the active fiber (D < 0) is opposed to that of the standard passive fiber (D > 0) where the pulses are propagating (PM1550-XP, Coherent), pulses self-compression takes place during the amplification. Hence, a specific compression stage is not necessary. The length of the active fiber, however, needs to be carefully adjusted, as well as the passive fiber of the output port of the isolator, in order to have the shortest possible pulse duration at the input of the NL stage. We do this adjustment without modulation, at 1.30 GHz, by measuring the spectrum and autocorrelation trace of the output pulses of the seed at a fixed pumping current of the PLD, 6.3 A (9 W PLD output power), for different passive fiber lengths, reducing it from 2 m to 1.32 m. When the optimized fiber length is found to be 1.32 m, i.e., when the temporal width at FWHM of the output pulses is minimum, the amplifier output is characterized at 6.3 A pumping current and 650 and 434 MHz repetition rates. For the train of pulses modulated to 650 MHz, the average output power, temporal pulse width at FWHM and bandwidth at FWHM are 2.1 W, 136 fs and 6 nm, respectively. In the case where the modulation reduces the frequency to 434 MHz, the average output power is the same but the temporal pulse width and bandwidth at FWHM are 120 fs and 26 nm, respectively. The characterization of both pumping conditions is summarized in Table 4.1 and the spectra and temporal pulses at the output of each amplifying configuration are shown in Fig. 4.4 a) and b), respectively.

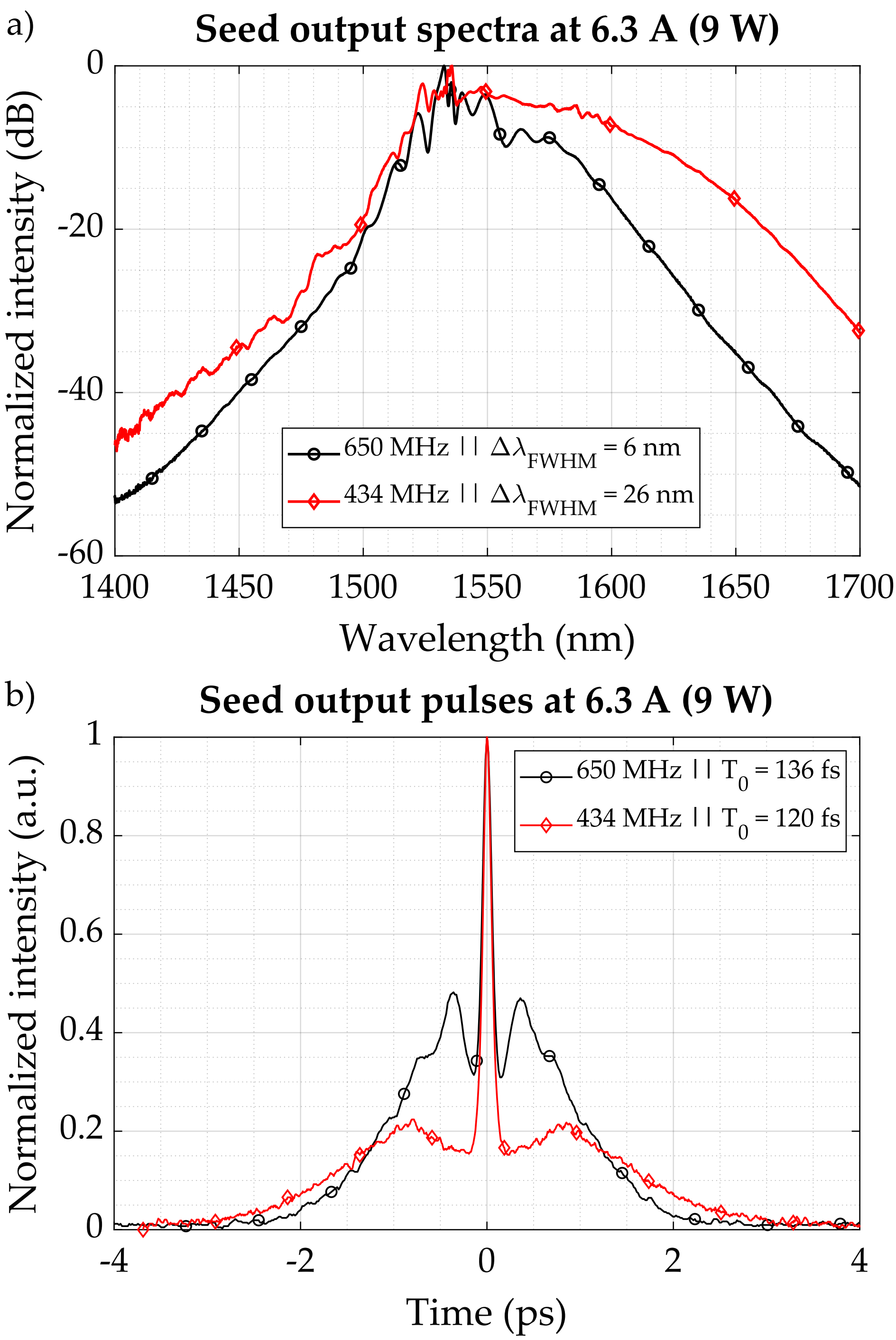


Figure 4.4. a) Spectra and b) autocorrelation traces at the output of the modulated seed at 6.3 A pumping current.

| Modulation | $f$ (MHz) | $\Delta\lambda_{FWHM}$ (nm) | $T_0$ (fs) | $P_{avg}$ (W) |
|---|---|---|---|---|
| **1/2** | 650 | 6 | 136 | 2.1 |
| **1/3** | 434 | 26 | 120 | 2.1 |

Table 4.1. Properties of the output pulses of the MF seed modulated at two different repetition rates. $f$: repetition rate, $\Delta\lambda_{FWHM}$: spectral bandwidth at FWHM, $T_0$: pulse temporal width at FWHM, $P_{avg}$: average power.

## 4.2. SC generation stage: GRIN fibers and excitation conditions

In section 4.1 we have described the MF seed developed to serve as excitation for the NL stage of the 1.5 μm SC source. Its pulses are launched into several pieces of all-solid GRIN fibers with different parameters. Each of these fibers is fabricated with the same refractive index contrast $\Delta n = 30.1 \cdot 10^{-3}$ (Fig. 4.5 a)) and all of them are fused silica fibers doped with 20 % of Ge in their core. Six samples of these fibers where manufactured by the group of Professor Philippe Roy at XLIM Research Institute with different core diameters, $d_c$, within a range of $d_c$ = [5.5 ; 6.5] μm. This range of diameters was defined from the simulations they performed to find the GRIN fiber dispersion curves fulfilling ANDi condition depending on the core size. The simulated dispersion curves of the pair of fibers with minimum and maximum $d_c$ within that range are presented in Fig. 4.5 b) (red-colored curves). We can observe that they have normal dispersion from 1200 to 1700 nm, a range of wavelengths wide enough to generate 1535 nm-centered SC under ANDi condition. However, when the dispersion curves of two drawn fibers were experimentally measured it was found that they present normal and anomalous dispersion regions, with a ZDW close to $\lambda_0$, as can be observed in Fig. 4.5 b) (black-colored curves). The experimental measurement of the dispersion curves was carried out by XLIM through synchronous interferometry [151] for two fibers with opposed sizes of the core, so the rest of the fibers must present a ZDW contained between those two: ZDW = [1454 ; 1534] nm. Table 4.2 summarizes the specifications of each sample: the core diameter is experimentally measured from the image of the cross-section of each fiber obtained by scanning electron microscope (SEM) while the NL coefficient, $\gamma$, and mode field area, MFA, are numerically estimated at 1535 nm [58,152].

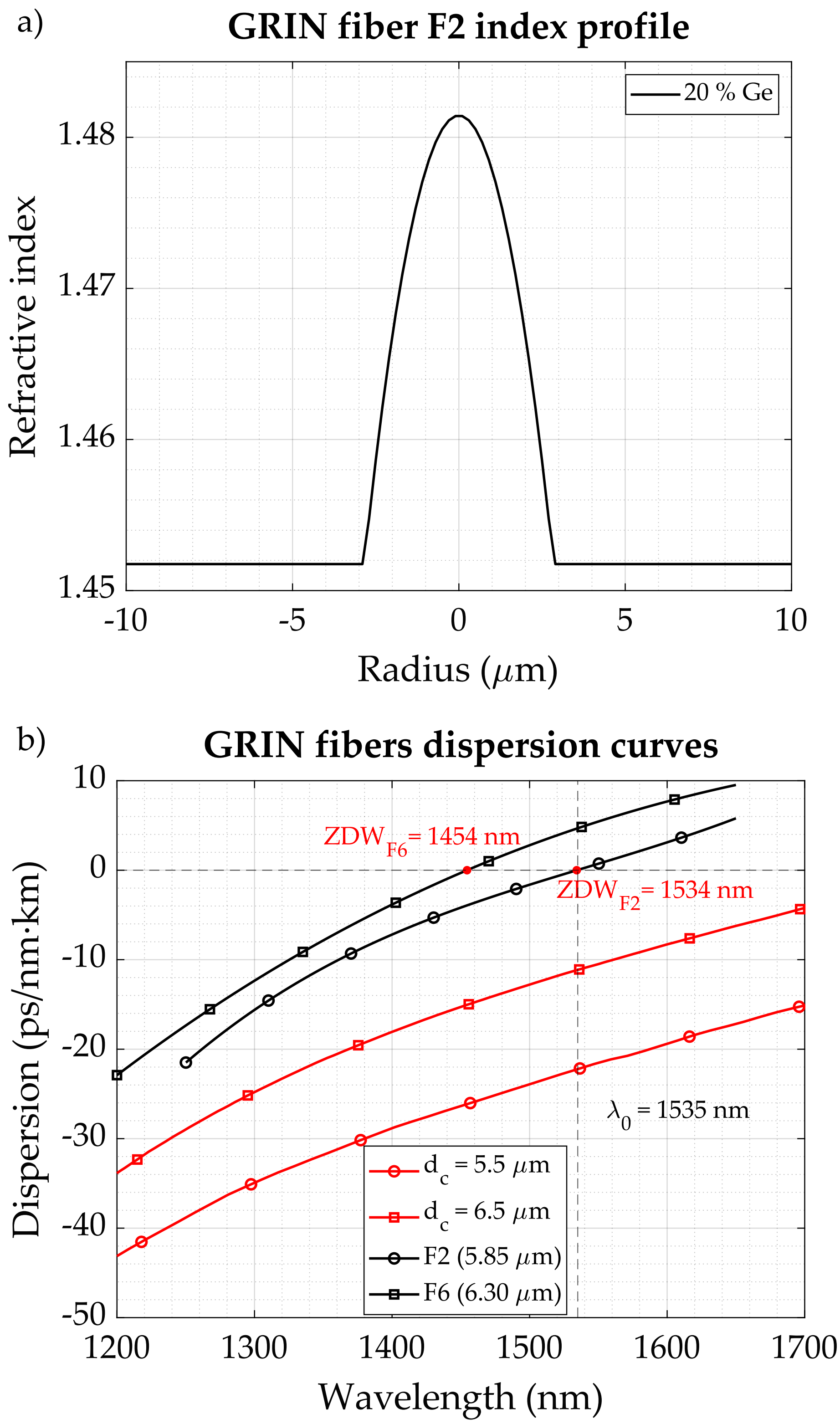


Figure 4.5. a) Profile of the refractive index of fiber F2. B) Simulated dispersion curves of the GRIN fibers of maximum and minimum target core diameter (red lines) and measured dispersion curves of the manufactured GRIN fibers (black lines).

| Fiber label | $d_c$ (μm) | γ ($W^{-1}·km^{-1}$) | MFA ($μm^2$) | ZDW (nm) | $D(\lambda_0)$ (ps/nm·km) |
|---|---|---|---|---|---|
| **F1** | 5.75 | 7.49 | 15.3 | - | - |
| **F2** | 5.85 | 7.40 | 15.5 | 1534 | 0.03 |
| **F3** | 6.00 | 7.27 | 15.4 | - | - |
| **F4** | 6.10 | 7.19 | 15.6 | - | - |
| **F5** | 6.15 | 7.14 | 15.7 | - | - |
| **F6** | 6.30 | 7.01 | 15.9 | 1454 | 4.67 |

Table 4.2. Parameters of each sample of GRIN fiber. $d_c$: experimental core diameter, $\gamma$: numerical NL coefficient, MFA: mode field area at 1535 nm, ZDW: zero-dispersion wavelength, $D(\lambda_0)$: dispersion at excitation wavelength $\lambda_0$.

Fiber samples from F3 to F5 have $d_c$ values between those of F2 and F6 (see Table 4.2), so they are expected to have zero dispersion at wavelengths shorter than that of F2, ZDW = 1534 nm. Being the excitation wavelength $\lambda_0$ = 1535 nm, fiber samples of fibers F3 – F6 are excited in their anomalous dispersion region, relatively far from their ZDW. Fiber F2 is also excited in its anomalous dispersion region but close to its ZDW, and fiber F1 can have a ZDW equal or over $\lambda_0$, so it is excited either at its ZDW or in its normal dispersion region very close to its ZDW. Previously reported theoretical works show that temporal coherence of the SC can be maintained pumping NL fibers even when the SC is not completely produced under normal dispersion [6,81]. Hence, we decide to experimentally study SC generation exciting these samples of GRIN fibers in their anomalous regime comparing the spectra obtained depending on how close the ZDW is to the pumping wavelength.

The output fiber of the MF seed is spliced to pieces of different lengths of these samples using the same technique explained for the 1.06 μm source: fiber transitions. The output fiber of the amplifier is the standard PM1550-XP fiber of 10.4 μm mode field diameter (MFD), which is more than twice the average MFD of the samples, 4.6 μm. Therefore, the splice is performed in two steps: first, we splice the passive fiber to a few mm of a transition fiber and then we splice the transition fiber to the piece of GRIN fiber sample. The coupling efficiency in every splice was optimized by manually adjusting the position of the fibers before splicing them. We measure the average power at 1.1 A pumping current at the output of the seed and then perform the fiber alignment in the splicing machine while we measure the average output power after the sample. The average percentage of losses between the average power at the output of the sample before and after splicing the fibers is ~ 19 %. We excite the GRIN fibers at 6.3 A pumping current and measure the average output power at the output of each sample, 1.1 W, and the spectrum obtained. In the following subsections the results obtained pumping these fibers are presented separately according to the modulation applied to the MF seed.

### 4.2.1. 650 MHz repetition rate excitation condition

We excite pieces of 22 cm of each GRIN fiber sample under 1/2 ratio modulation excitation condition and observe that for higher core diameters, corresponding to those samples with ZDW < $\lambda_0$ (F3 – F6), the broadening mechanisms are clearly produced by effects related to the anomalous group velocity dispersion region.

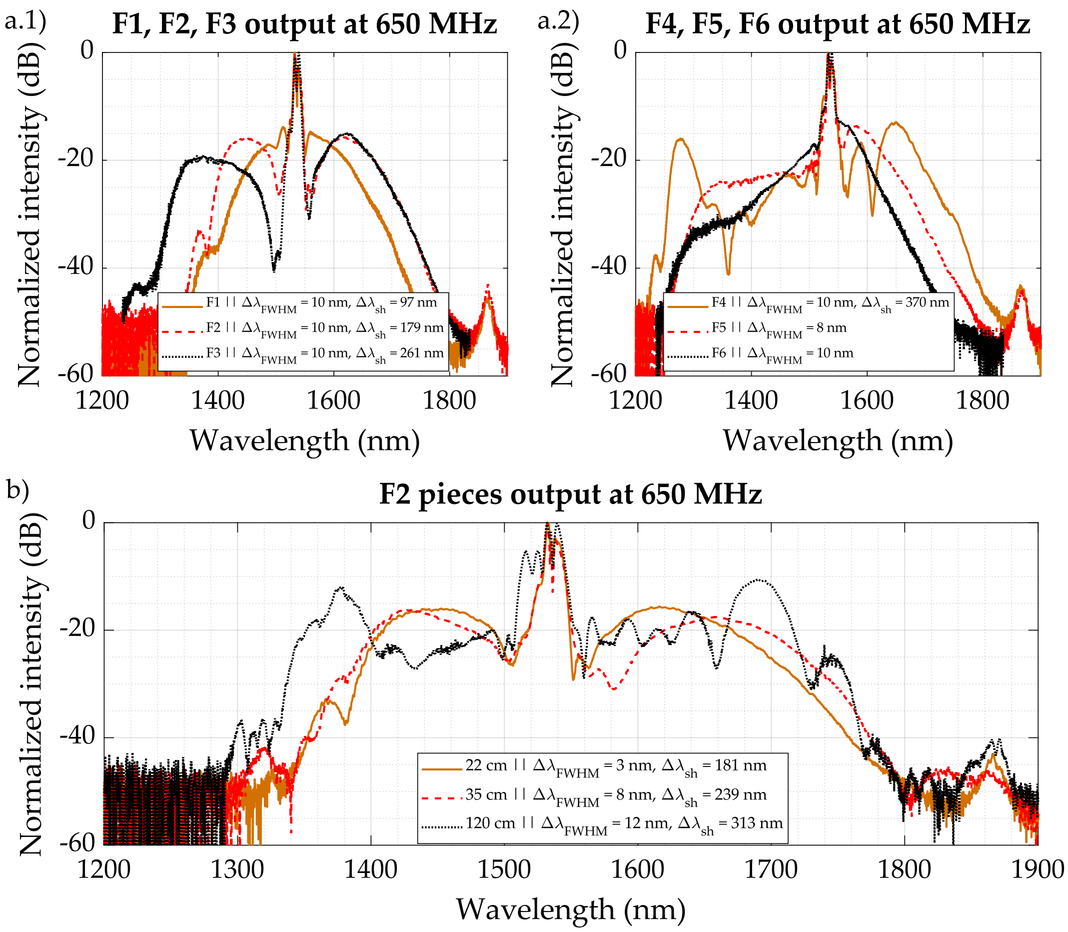


Figure 4.6. a.1) and a.2) SC spectra at the output of pieces of 22 cm of GRIN samples with different core diameters excited at $\lambda_0$ and 650 MHz. b) SC spectra at the output of pieces of different lengths of the GRIN fiber F2, excited under same conditions. Measurements with 1 nm resolution.

In Fig. 4.6 a.2), fiber F6, we can see the asymmetric and triangular shape classically observed when the excitation of the fiber is produced under anomalous dispersion with ZDW < $\lambda_0$. On the contrary, for the two fibers with ZDW ~ $\lambda_0$ (F1 and F2, Fig. 4.6 a.1)) the broadening, although narrower, is more symmetric and efficient. This change in the spectral shape is observed progressively from F6 to F1 as the fiber dispersion at the excitation wavelength changes from high anomalous values to low anomalous (very close to normal) values. The bandwidth between the shoulders of the spectra, $\Delta\lambda_{sh}$, is the parameter that we use to compare the broadening. Said bandwidth is defined as the difference between the wavelengths at which the shoulder presents maximum intensity. Observing the resulting $\Delta\lambda_{sh}$ of each output spectrum we find that, in the cases for which SC generation is achieved (output of fibers F1 – F4), the fibers excited further away from their ZDW (F3 and F4) deliver broader SC, $\Delta\lambda_{sh}$ > 200 nm, than fibers excited closer to their ZDW (F1 and F2), $\Delta\lambda_{sh}$ < 200 nm. Longer fiber lengths extend the broadening some tens of nanometers, as is the case for 35 and 120 cm of the fiber F2, shown in Fig. 4.6 b). The self-phase modulation (SPM) typical symmetric shape is maintained for every piece of fiber F2 of different lengths. Still, the efficiency of each one of these generated SC is very low with values of peak-shoulder ratio, PSR, the ratio between the maximum intensity and that of the shoulder of the spectrum, of > 16 dB.

These results confirm that the dispersion curves of the fibers are not ANDi and are in good agreement with what is expected when the broadening effects are induced in both normal and anomalous dispersion regions: first, SC generation is not achieved exciting the fibers far from the ZDW into de anomalous region; second, there is a huge broadening but asymmetric when the fibers are excited in their anomalous region and closer to the ZDW; finally, symmetric SPM-induced broadening appears when we excite them close to the ZDW.

Then, we reduce the pulse repetition rate of the seed and excite just fiber F2 which is excited close to its ZDW in order to improve the excitation conditions to generate SC aiming for values of PSR < 16 dB.

### 4.2.2. 434 MHz repetition rate excitation condition

We excite pieces of different lengths of fiber F2 with input pulses under 1/3 modulation excitation condition instead of 1/2. The difference in the excitation repetition rate translates into higher peak intensities. Thus, NLE induced to the

GRIN fiber are expected to be more efficient at 434 MHz than at 650 MHz, as we experimentally confirm and present in this subsection. Using the same MF seed to excite the pieces, under the same conditions of amplifier pumping current (6.3 A) and average output power (2.1 W), pulses of 120 fs at 434 MHz repetition rate are delivered through 5, 10, 25 and 86 cm of fiber F2. The pieces are spliced to the output of the seed performing the same fiber transition explained before and maintaining low losses of < 20 % between the average power at the output of the sample before and after the splice.

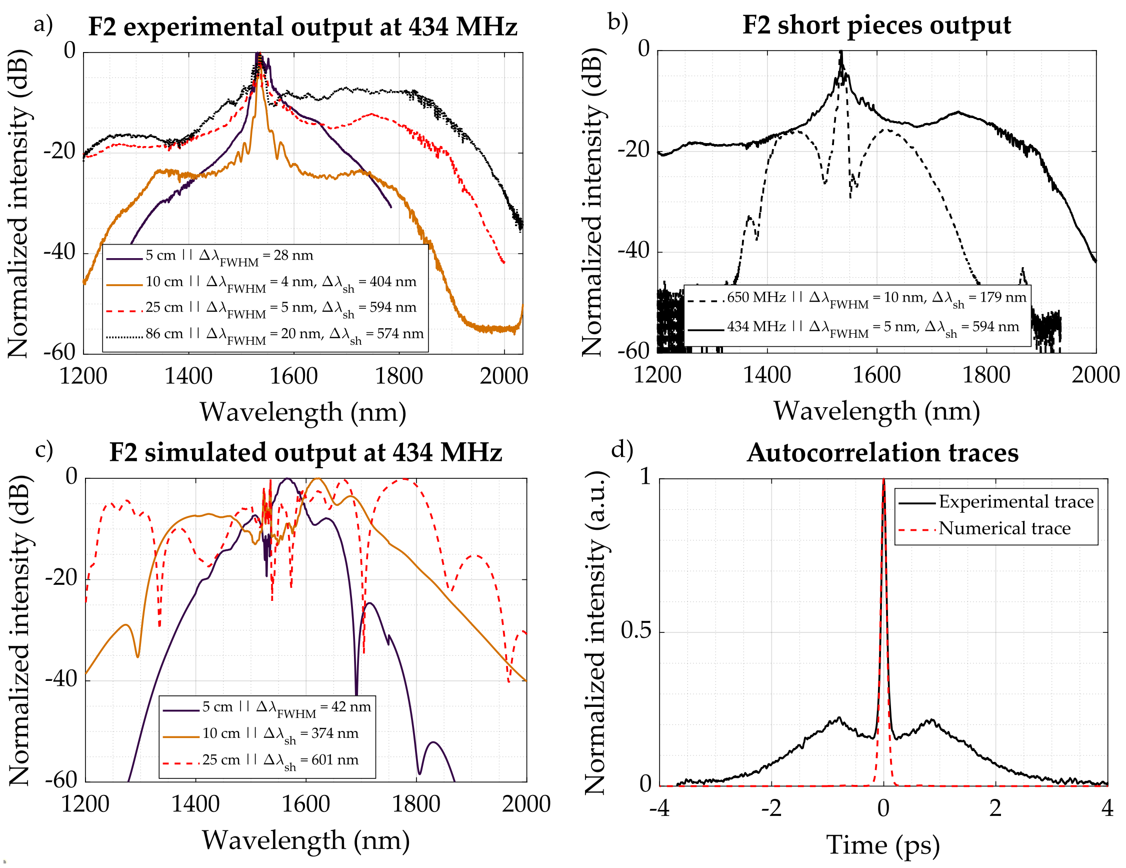


Figure 4.7. a) Experimental SC spectra at the output of pieces of different lengths of GRIN fiber F2 at 434 MHz seed repetition rate. b) Experimental SC spectra at the output of pieces of ~ 20 cm of fiber F2 at different seed repetition rates. c) Simulated SC spectra at the output of different lengths of fiber F2 at 434 MHz seed repetition rate. d) Experimental (black solid line) and numerical (red dashed line) autocorrelation traces at the output of the modulated seed (434 MHz).

Fig. 4.7 a) shows the resulting spectra at the output of said pieces of fiber F2 and Fig. 4.7 b) presents a comparison between the SC spectra generated at repetition rates of the seed of 650 and 434 MHz with 22 and 25 cm of F2, respectively. In these results we can see a significant improvement regarding the spectral broadening. While at 650 MHz the maximum broadening achieved was $\Delta\lambda_{sh}$ = 313 nm, exciting at 434 MHz we observe $\Delta\lambda_{sh}$ > 400 nm for every piece of fiber. At 434 MHz pumping condition we observe several differences between the spectra. First, the experimental curve corresponding to the 10 cm-length piece (yellow solid line curve in Fig. 4.7 a)) presents less broadening but more symmetric spectrum in comparison with the 25 and 86 cm-length pieces output (red dashed line and black dotted line curves, respectively): a 4 nm bandwidth at FWHM with 404 nm between shoulders against the 20 nm bandwidth at FWHM and 574 nm between shoulders of the longest piece. However, its PSR is over 15 dB in comparison with the 7 dB of the piece of 86 cm. In contrast, the longest piece shows the best PSR with a great broadening of > 500 nm. In this case, the shape of the resulting spectrum is slightly asymmetric with respect to the central wavelength. The 25 cm-length piece also generates a SC spectrum wider and more efficient than the 10 cm-length piece showing a broadening of $\Delta\lambda_{sh}$ = 594 nm and a 12 dB PSR. Second, in Fig. 4.7 a) we can observe an initial narrowing of the spectrum. When the input pulses propagate through 5 cm there is no SC generation and the bandwidth at FWHM is 28 nm, which is approximately the same as the input spectrum (Fig. 4.4 a)). However, when the pulses are sent through a 10 cm-length piece of fiber F2 we find that the spectrum narrows around the central wavelength. This spectral compression until 10 cm indicates that the input pulse is negatively chirped [58]. The positive NL chirp induced initially by SPM gives then rise to a reduction of the root-mean-square spectral width, as observed, e.g., in [153], that may last until the initial chirp is fully compensated and the pulse spectrum starts to broaden. Furthermore, the fact that the narrowing is more pronounced for red-shifted wavelengths suggests a left-skewed input pulse. Finally, attending to the spectra at 10 cm and 25 cm, sidelobes around 1750 nm and between 1250 and 1350 nm grow compared to neighboring wavelengths. This phenomenon could be attributed to phase-matched four-wave mixing (FWM) processes. Being initially located symmetrically with respect to the central wavelength (see the spectrum at 10 cm), the spectral sidelobes might originate from a degenerate FWM process where photons at the center pulse frequency act as pump waves, as in modulation instability [58]. In addition, in view of the spectrum at 25 cm, the positions of these red- and blue-shifted lobes move to longer and shorter wavelengths, respectively, as the pulse propagates. This shift along the propagation distance might be related to the emission of dispersive waves (another mechanism relying on phase-matched FWM [81,154]) under large high-order dispersion, as recently studied in [155].

We perform a preliminary simulation to check if the span of the output spectrum is in accordance with the widespread theory employed to model SC generation, the generalized nonlinear Schrödinger equation (GNLSE) [58]. Dr. David Castelló was responsible of the simulation using his own model developed at the Laboratory of Fiber Optics (Laboratori de Fibres Òptiques) of the University of Valencia. To model the propagation of the pulses the program uses a free-access Runge-Kutta routine to solve first-order differential equations and a free-access routine to calculate fast Fourier transforms. As input data we use our experimental data such as the length of the fibers, the temporal pulse shape of the input pulses and the dispersion parameters of said fiber. On the one hand, from the intensity autocorrelation of the input pulse (Fig. 4.7 d) black curve) a multipulse structure can be inferred. Even though a main pulse is apparent, its peak power is necessarily several times below the ~ 45 kW value corresponding to a truly single input pulse. Since complex pulse shapes cannot be derived from the pulse autocorrelation and spectrum alone [58], and taking into account the purpose of these simulations, a pragmatic approach is adopted here: a quadratic spectral phase is assumed [156] in order to recover the width of the main lobe of the autocorrelation trace from the input pulse spectrum. In light of our previous interpretation, the sign of the spectral phase is chosen so that a negative (temporal) chirp is obtained. Importantly, only the main pulse in the autocorrelation trace is considered, together with the average power determined experimentally, to estimate an effective peak power of 10 kW for the input pulse employed in these simulations. On the other hand, from the dispersion curve measured for fiber F2, with a NL refractive index $n_2 = 2.78 \cdot 10^{-20}$ m$^2$/W [157] and a NL coefficient $\gamma = 7.4$ W$^{-1}$km$^{-1}$, the GNLSE has been numerically solved. Fig. 4.7 c) shows the simulated output spectra after 5, 10 and 25 cm of fiber F2 at 434 MHz repetition rate. Despite the approximations, the simulation reproduces the output bandwidth observed experimentally, including the red- and blue-shifted spectral resonances, obtaining $\Delta\lambda_{sh} = 601$ nm.

Analyzing the results presented in this section we can see that the optimized SC is achieved exciting pieces of 25 cm of the GRIN fiber F2 with the MF seed modulated to 1/3 of its natural repetition rate, supplying pulses of 64.5 GW/cm$^2$ peak intensity (for an effective peak power of 10 kW). The SC spectrum shows the best PSR and broadening values, and it conserves a high level of symmetry with respect to the central wavelength. Therefore, from now on we define the MF SC source at 1.5 μm as the optimized architecture in which we excite a piece of the GRIN fiber F2 of 25 cm at 434 MHz seed repetition rate and 6.3 A amplifier pump current. After the spectral characterization of the output of the SC source we perform its temporal characterization and study its temporal coherence. The experimental results of the pulse compression and the study of the degree of coherence are explained in the following section.

## 4.3. SC temporal characterization

Once we have determined the best excitation conditions and output spectrum, we connectorize the output fiber, collimate its output (F280FC-1550 collimator, Thorlabs) and measure the output temporal shape of the pulses. The temporal characterization of the pulses is performed with an intensity autocorrelator at the collimated output of the source (Fig. 4.8) and with an interferometric autocorrelator (Fig. 4.9 b) and c)) after the compression module. The measurement (Fig. 4.8 circle-marked black curve) gives a temporal width of the pulses at FWHM of 2.9 ps. According to the Fourier transform limit (FTL) of the optical spectrum, shown in Fig. 4.8 (diamond-marked red curve), the pulses of this SC source can be compressed down to 29 fs if they are temporally coherent. We design experimental setups to perform pulses compression of the output of the source using a free-space wedges pulse compressor developed and manufactured by Sphere Ultrafast Photonics, and to measure the degree of coherence of the source using an interferometer, respectively described in subsections 4.3.1 and 4.3.2.

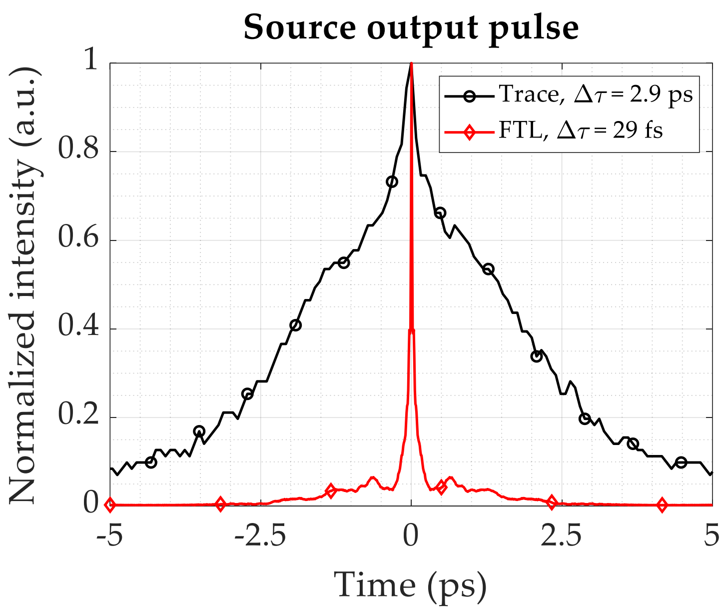


Figure 4.8. Experimental autocorrelation trace (circle-marked black line) and calculated FTL autocorrelation trace (diamond-marked red line) of the output pulses of the SC source. $\Delta\tau$: temporal width at FWHM.

### 4.3.1. Pulse compression technique

To estimate the temporal coherence of the source we use a free-space pulse compressor, with the aim to compress the pulses to their calculated FTL of 29 fs. The compressor is composed of a pair of wedges which introduces a variable dispersion between ~ – 3310 fs$^2$ and – 1324 fs$^2$ in the optical path of the beam. The insertion length is adjusted for this compressor in the same way as for the 1.06 μm d-scan: one of the wedges is motorized so that it is possible to change the insertion length of that wedge with respect to the other from 4 to 10 mm.

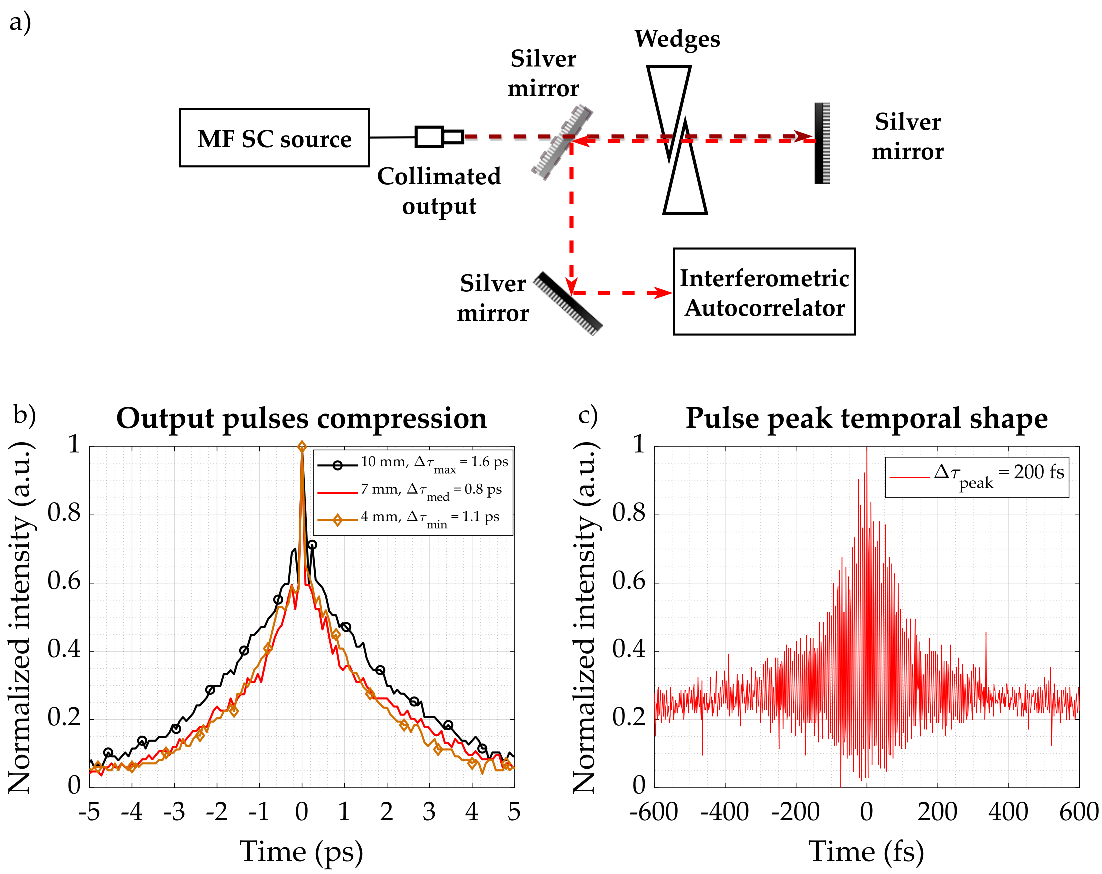


Figure 4.9. a) Experimental setup to compress and measure the SC source output pulses. b) Autocorrelation traces of the pulses at the maximum (10 mm, circle-marked black line), intermediate (7 mm, solid red line) and minimum (4 mm, diamond-marked yellow line) insertion lengths. c) Autocorrelation trace of the peak of the pulse at the intermediate insertion length.

Fig. 4.9 a) shows the experimental setup where the source output beam goes through the wedges in a double step configuration and then it is sent to the autocorrelator using silver mirrors (PF10-03-P01, Thorlabs) that provide > 97 % reflectance from 450 to 2000 nm. The beam going from the source to the wedges follows a path which is set at a higher height than the path followed by the beam returning from the wedges to the first silver mirror (the mirror placed closest to the source). Scanning three different positions of the motorized wedge (maximum, intermediate and minimum), we measure with an interferometric autocorrelator the autocorrelation traces of the pulses looking for the minimum temporal width at FWHM. The autocorrelation traces of the pulses measured at the three insertion positions are shown in Fig. 4.9 b). A minimum temporal pulse width at FWHM is found for the intermediate position of the wedge insertion, 7 mm. The obtained value is 0.80 ps, which is far from the FTL of the spectrum. However, the pulse shows a noise-like shape [158] characterized by a pedestal of picoseconds and a narrower peak over said pedestal. Measuring the pulse width of the peak that rises over the pedestal of the output pulse when it traverses through 7 mm of wedge material, we find a lower temporal pulse duration of 200 fs (Fig. 4.9 c)). These results reveal that we are broadening the spectrum classically, without maintaining the temporal coherence for the new generated wavelengths. Thus, the output pulses are not compressible to their FTL even though a certain compression can be achieved at the peak in the shape of noise-like pulses.

### 4.3.2. Measurement of the degree of coherence

To further confirm the level of temporal coherence of the source we design an interferometric experimental setup (based on works previously reported [80,159]) to measure the degree of coherence between consecutive pulses, $g_{1,2}$. Fig. 4.10 a) shows our experimental setup based on the Michelson interferometer. The collimated output of the source is aligned with a beam splitter (BS) (BP145B3, Thorlabs). The BS separates the beam into two paths, arm 1 and 2 of different lengths calculated to bring together one pulse and its consecutive in the last segment of propagation: $L_1 = S/2$ and $L_2 = S$ where $S$ is the distance of separation between two consecutive pulses calculated with 434 MHz repetition rate of the source. To perform a fine adjustment of $L_2$, the second arm is designed with a motorized mirror that allows translations of the order of several hundreds of micrometers. The BS film introduces differences in the polarization of both arms. Therefore, a half wavelength plate is used to control the polarization of arm 2 with respect to arm 1. The optical path where both arms are again propagating together is aligned with an optical spectrum analyzer that returns the trace of the spectrum measured with 1 nm resolution. The spectrum resulting from the interference of one pulse and the following is used to calculate $g_{1,2}$ with the visibility of the fringes of the interference, $V(\lambda)$:

$$V(\lambda) = \frac{I_{max}-I_{min}}{I_{max}+I_{min}} = g_{1,2}\,\frac{2\sqrt{I_1(\lambda)\cdot I_2(\lambda)}}{I_1(\lambda)+I_2(\lambda)} \tag{4.2}$$

where $I_{max}$ and $I_{min}$ are, for a given wavelength $\lambda$, the closest to $\lambda$ maximum and minimum intensities of the interference pattern, respectively. $I_1(\lambda)$ and $I_2(\lambda)$ are the spectral intensities at $\lambda$ when the light travels only through arm 1 and only through arm 2, respectively. The visibility of the fringes is calculated for an averaged trace resulting from 20 different traces measured under the same conditions. The interference measurement (left axis) and its corresponding calculated degree of coherence (right axis) are shown in Fig. 4.10 b).

We can see that the degree of coherence is ~ 0.7 around 1535 nm (wavelength at which the seed has a high degree of coherence of 0.9), but it is not maintained for the rest of the spectrum, where it decreases to almost 0.1. One reason for the loss of coherence out of the bandwidth of the seed might be the excitation of the GRIN fiber F2 so close to its ZDW. The SPM broadening effect happens both in the normal and anomalous dispersion regions enabling mechanisms which do not conserve the temporal coherence of the SC: Raman-induced soliton shift, stimulated Raman scattering or modulation instability, for instance [27,58,160], as opposed to our 1.06 μm source in which SPM happens only in the normal dispersion region. With fiber dispersion curves of ZDW so close to $\lambda_0$, coherence is not expected to be maintained for the wavelengths out of the bandwidth of the seed.

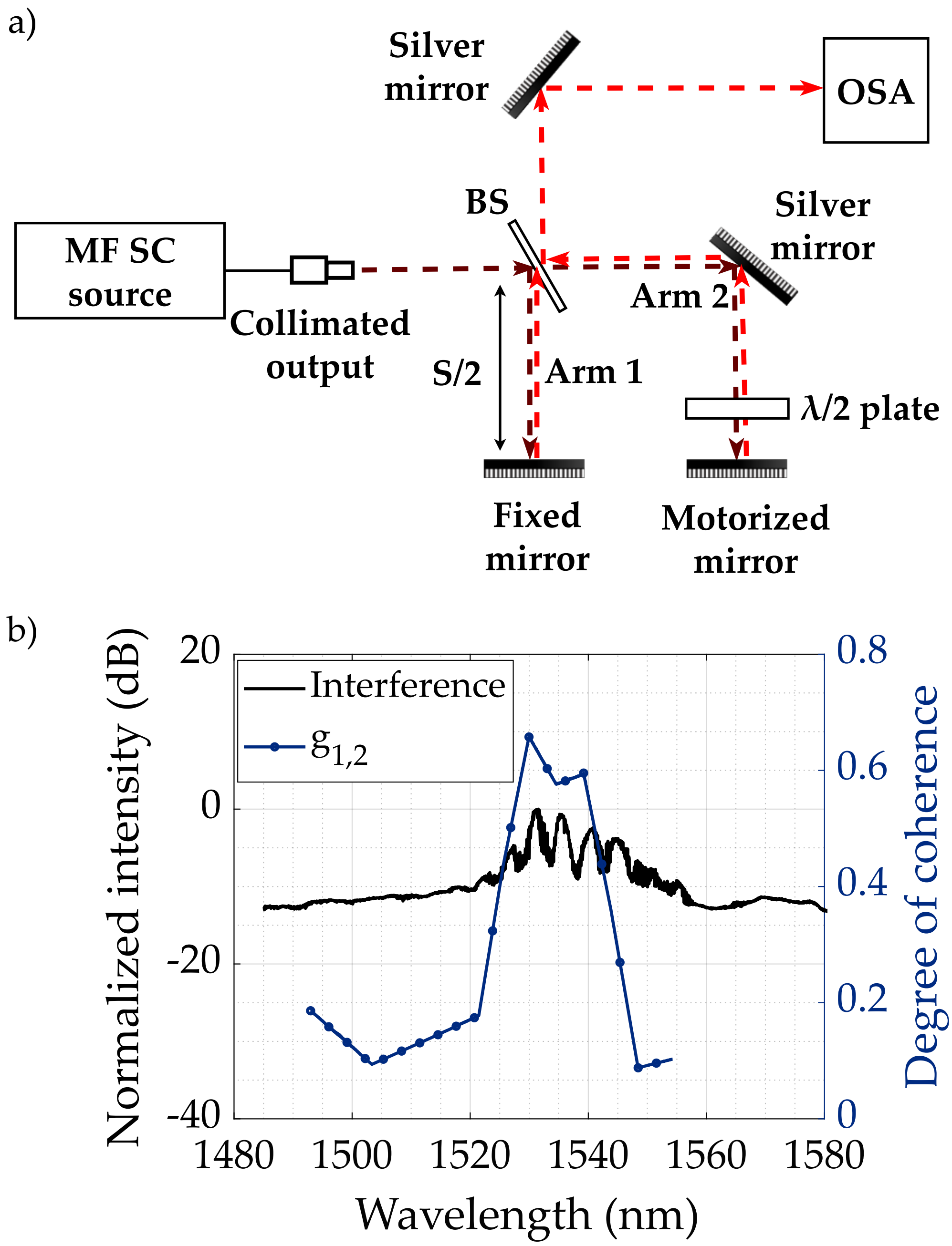


Figure 4.10. a) Experimental setup of measurement of the degree of coherence. b) Spectral trace of the interference pattern generated from two consecutive pulses (left axis) and its calculated degree of coherence (right axis).

Chapter 5

# Application in NLO microscopy

In the previous chapters of this thesis we have introduced the concepts of supercontinuum (SC) generation and the nonlinear (NL) processes that are induced in all-normal dispersion photonic crystal fibers (ANDi PCFs) and graded-index (GRIN) fibers to coherently broaden the spectrum of the pulses that propagate through said fibers. We also have explained the architecture and the output pulse characteristics of the sources that we have designed and manufactured at 1.06 and 1.5 μm wavelengths. As a final part of this work of PhD thesis, we explain in more detail in this chapter the advantages that our sources bring to nonlinear optical (NLO) microscopy applications. Section 5.1 is a brief introduction to the NLO microscopy applications in which we focus on this work. Then, section 5.2 presents the results obtained using our 1.06 μm source as exciting source for such applications and we compare them to the results obtained using a commercial Ti:Sa femtosecond laser, the source which is currently more employed in NLO microscopy.

## 5.1. NLO microscopy applications and exciting sources

Through optical microscopy we obtain functional and morphological information by imaging samples of specimens in a non-invasive way. In the case of NLO microscopy applications, the images of the samples are obtained through techniques based on nonlinear effects (NLE). These applications have attracted enough interest to experience an important progress from decades ago, when first seminal proposals envisioned its advantages [161,162], to the present, when is an indispensable facility in microscopy services of large scientific institutions [163–165]. This is due to the fact that they benefit from the advantages that NL processes present, which allow to observe samples of living specimens over time without perturbating them and to extract a higher amount of information. For instance, multiphoton excitation microscopy (MPM) is based on the use of NL processes involving the excitation of two or more photons. The advantages that multiphoton excitation presents stem from its quadratic or higher order dependence with the intensity of the light used to excite the fluorophores of the samples. On the one hand, since the simultaneous excitation of two or more photons only takes place at high intensity values, the interaction between the fluorophore and the incident photons is limited to the focal plane of the sample where the beam is focused and intensity is maximum. This means that there is only a small focal volume where the sample is perturbed. Light out of focus does not excite the sample and there is no risk of obtaining imaging from out-of-focus scattered light. In contrast to microscopy techniques based on linear processes, perturbation of just a small focal volume favors sectioned imaging, allowing to obtain three-dimensional images of the samples. On the other hand, to efficiently induce multiphoton processes high photon irradiances are required [166,167]. Ti:Sa lasers are the sources typically used as exciting light for MPM [163]. These sources emit ultrashort pulses of the order of femtoseconds (in some cases with pulse durations as short as the time corresponding to few oscillations of the optical field, i.e., in the few-cycle regime), at low average power levels of the order of milliwatts and at wavelengths between 700 and 1000 nm, providing very high photon irradiances (typically > $10^{27}$ photons/s·cm$^2$). These characteristics bring advantages to the MPM: the possibility of imaging living specimens thanks to the low energy of the pulses, a wider range of biological scattering tissues that can be penetrated at longer wavelengths [141] reaching depths 2 or 3 times higher than with confocal microscopy [164], and the possibility of simultaneously exciting several microscopy techniques and/or exciting light-emitting probes at different incident wavelengths because of the broad spectrum inherently associated to few-cycle pulses (bandwidths typically > 200 nm for sources operating in the near-IR). Therefore, in contrast to classic single-photon fluorescence microscopy, MPM techniques allow deep tissue penetration, 3D-sectioning imaging, out-of-focus scatter-free imaging, small focal volume (thus high resolution in all three spatial axes), imaging of living specimens, and multimodal and multispectral microscopy [14,15].

Among multiphoton excitation processes which are part of the MPM techniques we can find: two or three-photon excitation fluorescence (2PEF, 3PEF), second or third-harmonic generation (SHG, THG), sum-frequency generation, stimulated Raman scattering and coherent anti-Stokes Raman scattering. Multiphoton excited fluorescence (MPEF) and SHG are amongst the most relevant MPM techniques for biological investigations. MPEF is a NL process based on the absorption of two or more photons of the same energy by a molecule which interacts with them. In MPEF, the sample is administered some light-emitting probes which are chemically bound to the biological target material, e.g., DNA or proteins. These probes, as can be dye molecules or fluorescent proteins, are excited with the incident light from the microscope and the light emitted in response is detected and used to reconstruct the images [168]. When the intensity of the exciting light is high enough, the fluorescent molecule used as probe absorbs two or more incident photons simultaneously. The energy it emits is equivalent to that which the molecule would emit when absorbing one single photon of energy equal to the sum of energies of the lower-energy incident photons. Fig. 5.1 illustrates the difference between single-photon and two-photon absorption. In the single-photon example, an incident single photon of wavelength $\lambda_s$ and energy $E_s = \hbar c/\lambda_s$ is absorbed by the molecule and another photon of wavelength $\lambda_e$ is emitted in exchange with energy $E_e = \hbar c/\lambda_e$. In the two-photon example, two photons of wavelength $2\lambda_s$ and energies $E_1 = \hbar c/(2\lambda_s)$ and $E_2 = \hbar c/(2\lambda_s)$, respectively, are absorbed by the molecule and yet the photon emitted has the same wavelength and energy that the one emitted in the single-photon example: $\lambda_e$ and $E_e = \hbar c/\lambda_e$. In both cases the energy emitted is slightly lower than the total energy of all the incident photons. On the contrary, in the SHG process the energy is conserved as two photons of the same energy interact simultaneously with non-centrosymmetric structures, without being absorbed, by NL polarization [163]. Then, the radiation emitted as a consequence of the annihilation of those two photons has an energy which is exactly twice the energy of the incident photons: the wavelength of the emitted radiation, $\lambda_e$, is half the wavelength of the incident photons, $\lambda_e = \lambda_i/2$, as presented in Fig. 5.1.

As mentioned before, MPM benefits from the ability of simultaneously employing different microscopy techniques. For instance, through MPEF we can excite both endogenous and exogenous fluorophores, while SHG can enable observation of the spatial structure of non-centrosymmetric materials and/or interfaces (e.g., changes of the index of refraction) in unlabeled biological specimens [169].

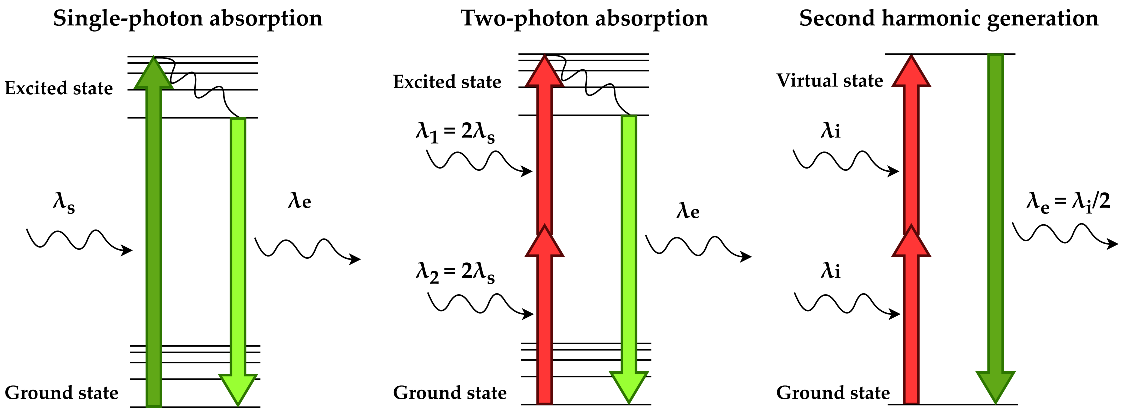


Figure 5.1. Schemes representing processes of single-photon and two-photon absorption and second-harmonic generation.

The kind of light used to induce these effects, as described above, are pulsed lasers of pulse durations in the femtosecond range. Femtosecond pulsed laser sources present the best trade-off between high photon irradiance and harmless average power. Particularly, few-cycle sources delivering pulse durations in the range of 10 fs increase the efficiency of multiphoton excitation processes by an order of magnitude [170], helping to reduce the average power on the samples and maximize their viability. We can find sources with pulse durations of around 100 fs, such as solid-state and optical fiber mode-locked lasers, used as exciting sources for NLO microscopy [16,163,164]. There are also sources of shorter pulses as of 60 fs, achieved by frequency conversion of mode-locked fiber lasers, proposed for NLO microscopy and NL vision studies [171–174]. Few-cycle sources, however, are less explored as excitation sources, even though the availability of all-fiber few-cycle sources with emission in the 1 μm region is of special interest in biological microscopy. In the infrared (IR) spectral region there is a good compromise between the two main factors that limit the imaging depth in biological samples: the scattering and the absorption coefficients of the tissues [175–178]. For longer wavelengths both coefficients decrease exponentially [176,177]. This means that, compared to Ti:Sa source pulses emitted at 800 nm, pulses emitted from a fiber laser at 1.06 μm such as the one described in chapter 3 are less affected by scattering and absorption.

Furthermore, pulses in the 1.5 and 2 μm regions [8,179] suffer even less scattering and have been used successfully in 3PEF microscopy. Comparing the results from using pulses in these spectral regions for 3PEF microscopy to those obtained from using 1 μm pulses for 2PEF microscopy, pulses of longer wavelengths have shown deeper penetration, lower signal to background ratios and reduced out-of-focus background [177,180]. However, in the 1.5 and 2 μm regions the absorption coefficient in water is up to 2 and 3 orders of magnitude higher compared to the 1 μm band [176,177]. Besides, for a given fluorophore, the two-photon absorption coefficient is several orders of magnitude higher than the three-photon absorption coefficient. This means that to generate a 3PEF signal comparable to 2PEF signal higher peak powers are required [181] and, since a higher photon density is needed to generate three-photon images, it is more probable to cause damage to the sample, compared to two-photon images.

## 5.2. 1.06 μm all-fiber few-cycle source for broadband multispectral and multimodal NL imaging

In this section we present the experimental setup and the results on the performance of the 1.06 μm few-cycle all-fiber source described in chapter 3 as exciting light source in multimodal and multispectral NLO microscopy. These experiments and measurements were carried out by the research group of Professor Pablo Loza at ICFO and by Dr. Salvador Torres from FYLA LASER.

Fig. 5.2 shows the experimental setup: the output of the free-space compressor (stage 6) of the system is coupled to an adapted inverted confocal microscope (Eclipse TE2000-U, Nikon) modified for NL imaging experiments. We use the variable dispersion compressor to pre-compensate the dispersion of the optical elements in the path of the microscope towards the sample, where the pulse duration is maintained below an estimated duration of 16 fs (inset in Fig. 5.2). The 15.6 fs duration is calculated from the autocorrelation trace (assuming a deconvolution factor of 0.71 for a Gaussian-shaped pulse), which is only slightly longer than the duration at the output of the source (12.6 fs, estimated with the same Gaussian-shaped approximation, in Fig. 3.13). This difference is mostly due to residual uncompensated higher order dispersion (TOD and above) of the optics in the path of the beam, and not due to loss of spectral components.

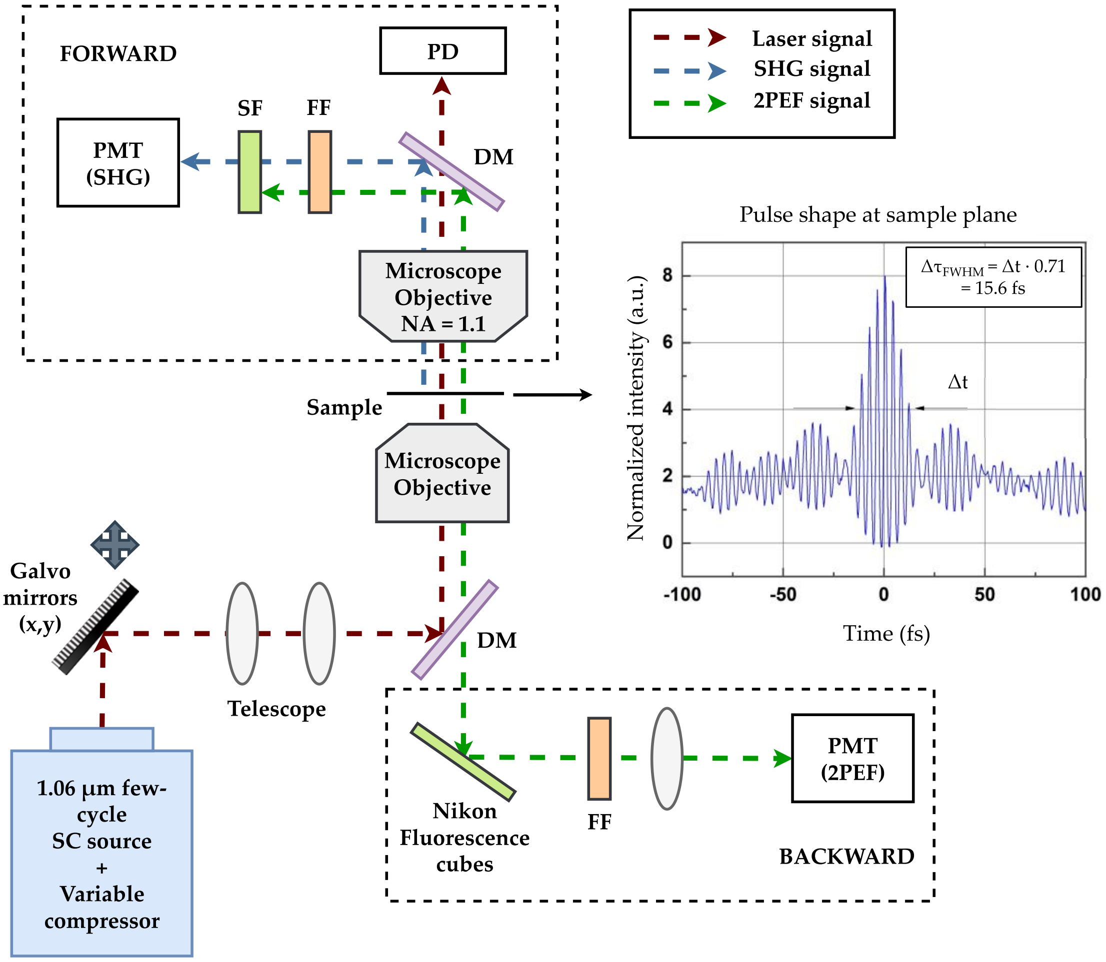


Figure 5.2. Setup diagram. The excitation laser (red arrows) is focused with a microscope objective on the sample. The 2PEF signal (green arrows) is collected in the backward direction. In the forward direction, the excitation laser and the SHG signal (blue arrows) are collected with a microscope objective. A dichroic mirror (DM) is used to separate the laser light from the NL signals. The 2PEF signal is filtered from the SHG signal with a narrow bandpass filter (second filter, SF). The 2PEF and SHG signal are detected using photomultiplier tube (PMT) detectors. The transmitted light from the excitation laser is detected with a photodiode (PD). Inset: interferometric autocorrelation trace of the pulse, measured at the sample plane, compressed to its minimum achievable duration, for the case of XL Plan N 25x objective. NA: Numerical aperture, FF: first filter, $\Delta\tau_{FWHM}$: temporal width at FWHM.

The coupling system of the external illumination source includes two galvanometric mirrors (Cambridge Technology, UK) and a telescope arrangement. We use a dichroic mirror (DM) (FF825-SDi01, Semrock) for sending the pulses to the illumination objective. The generated fluorescent light captured using this objective is collimated and sent through the same DM, in a non-descanned configuration, for detection using a photomultiplier tube (PMT) detector (H9305-04, Hamamatsu). Three different microscope objectives, with different refractive index immersion media, numerical apertures (NA) and magnifications are used (see Table 5.1). We perform dispersion pre-compensation for each of these objectives. The illumination source used for all image acquisitions is the few-cycle all-fiber source described in chapter 3, except for images in Fig. 5.4 (F),(H) that were generated with a pulsed Ti:Sa laser (MIRA 900-F, Coherent, 200 fs nominal pulse width) operating at a central wavelength of 810 nm. Possible leakage of fundamental laser light was blocked with a 350 – 700 nm bandpass filter of BG40 glass (FGB37-A, Thorlabs, first filter FF in Fig. 5.2). The 2PEF signal is filtered with fluorescence filter cubes (DAPI, FITC and TRITC: Standard series, Nikon) and collected in the backward direction. We use a 25x NA1.10 water immersion objective (Apo LWD, Nikon) for the SHG signal collection in the forward direction. A DM (FF665-Di02, Semrock) separates the laser light from the NL signals. The SHG signal is filtered with a bandpass filter (FF01-542/27-25, Semrock, second filter SF in Fig. 5.2).

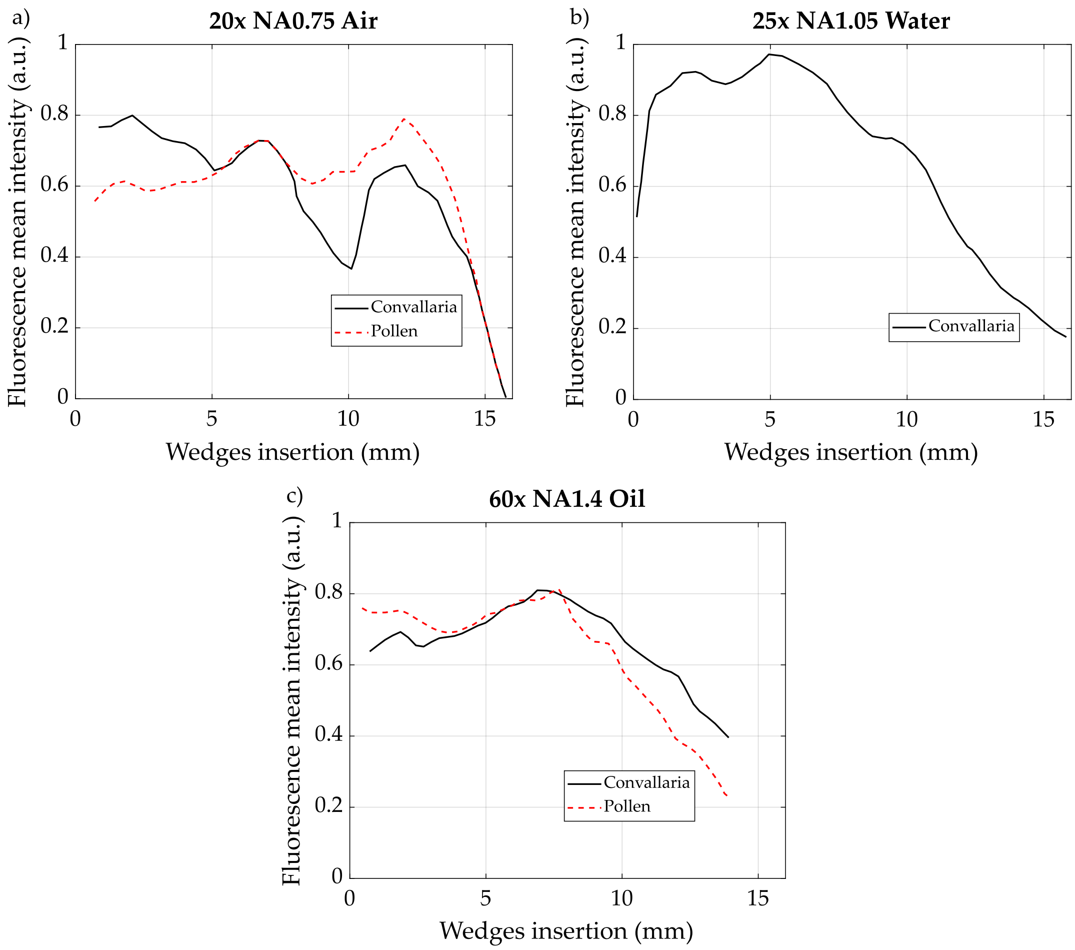


Figure 5.3. Mean intensity of the generated 2PEF signal as function of insertion length of the variable compressor glass wedges, for different objectives and sample specimens (Convallaria and pollen).

| Objective | Brand | Magnification | NA | RI Medium |
|---|---|---|---|---|
| **Plan Apo λ** | Nikon | 20x | 0.75 | Air |
| **XL Plan N** | Olympus | 25x | 1.05 | Water |
| **Plan Apo DIC H IR** | Nikon | 60x | 1.4 | Oil |

Table 5.1. Parameters of each microscope objective. NA: numerical aperture, RI: refractive immersion.

Once the source is completely integrated in the above described setup, the performance of the dispersion pre-compensation of the variable compressor is evaluated by varying the glass wedges insertion to adjust the duration of the pulse at the sample plane, as described in chapter 3. For each image, we measure the mean intensity of the generated 2PEF signal as a function of glass insertion. The results can be seen in Fig. 5.3. The induced dispersion per glass insertion length is + 147 $fs^2$/mm. We see that the pre-compensation system can be efficiently used to maximize the fluorescent signal from the sample. A maximum 2PEF intensity depending on the insertion of the glass is observed. This indicates that the system is capable of pre-compensating the dispersion introduced by the different microscope objectives. The discrepancies found in the optimum insertion length when imaging different samples can be attributed to changes in the refractive index of the samples.

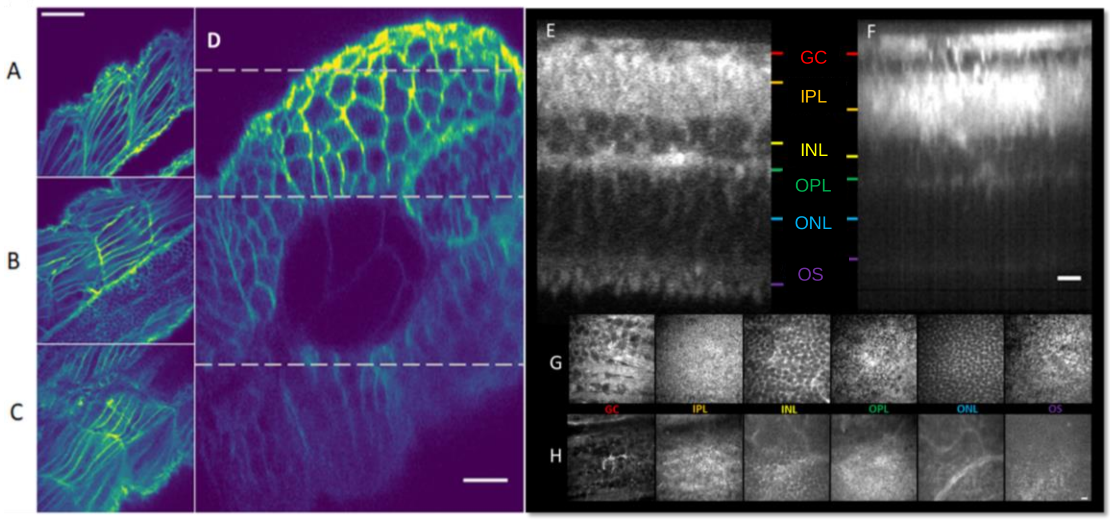


Figure 5.4. (A)-(D) 2PEF images of the tail of a 2-days-old transgenic line zebrafish embryo (CAAX-GFP) expressing green fluorescent protein (GFP) in all cell membranes: (A)-(C) Intensity-normalized images corresponding to 26, 71 and 150 µm depth, respectively. Scalebar: 40 µm. (D) Lateral re-slice of a Z-stack composed of 300 images (0.71 µm step spacing). Scalebar: 20 µm. (E)-(H) Comparison of 2PEF imaging performance between our few-cycle all-fiber temporally coherent SC source (E),(G), and a Coherent MIRA 900-F laser (F),(H), as illuminating

sources for 2PEF imaging of an excised rat retina (retinal ganglion cells side up) stained with Alexa Fluor 647-phalloidin and Alexa Fluor 405-phalloidin, respectively: (E) Lateral re-slice of a Z-stack composed of 376 images (0.52 μm step spacing) acquired with the few-cycle all-fiber source. (F) Lateral re-slice of a Z-stack composed of 404 images (0.50 μm step spacing) acquired with the Coherent MIRA 900-F laser. Scalebar: 15 μm. GC: Ganglion cells; IPL: Inner plexiform layer; INL: Inner nuclear layer; OPL: Outer plexiform layer; ONL: Outer nuclear layer; OS: Outer segment photoreceptors.

Using the 25x objective under the optimized group velocity dispersion settings of the compressor, we have successfully imaged several samples. Importantly, good fluorescence signal and depth are achieved using an average power of the pulsed beam of ~ 4 mW, measured at the sample plane. With a variable neutral density filter and helped by intrinsic losses of the optical components placed along the microscope optical path, we attenuate the beam at the output of the variable compressor, where it has 160 mW of average output power. The maximum penetration achieved corresponds to 220 μm in depth (Fig. 5.4 (A)-(D)) of the tail of a transgenic line zebrafish embryo (CAAX-GFP) expressing green fluorescence protein (GFP) in all cell membranes. Zebrafish embryos are transparent, so they allow imaging at these large penetration depths. To test the penetration capabilities of the laser within a scattering tissue two excised rat retinas were stained with the same cytoskeleton marker (phalloidin), each conjugated with a different fluorescent dye: AlexaFluor 405 and 647, to be excited with a Ti:Sa Coherent MIRA 900-F laser ($\Delta\lambda_{FWHM}$ = 10 nm, $\lambda_0$ = 810 nm) and with our few-cycle all-fiber source ($\Delta\lambda_{FWHM}$ = 150 nm, $\lambda_0$ =1060 nm), respectively. We proceeded to record the full retina (~ 170 μm) with cellular resolution, acquiring Z-stack images (Fig. 5.4 (G) and (H)). For both lasers, we used the same laser power at the sample plane and similar step spacing for constructing the Z-stacks. Then lateral re-slices of the Z-stack images were performed. Fig. 5.4 (E) and (F) show the comparison of the lateral re-slice 2PEF images acquired with our few-cycle all-fiber source and with a Coherent MIRA 900-F laser, respectively. In the image acquired with our few-cycle all-fiber source, all synaptic (bright regions) and nuclear (gap regions) layers that characterize the tissue can be distinguished (Fig. 5.4 (E)). However, in the images acquired with the Coherent MIRA 900-F laser it was only possible to distinguish four layers (Fig. 5.4 (F)). Larger imaging depth was achieved using the few-cycle all-fiber source, with which properly resolved images of the retina deeper layers ONL (outer nuclear layer) and OS (outer segment photoreceptors) were obtained (Fig. 5.4 (E) and (G)). It is interesting to mention that the rat retina is highly autofluorescent to light in the blue-green region of the spectrum. In addition, the external segment of the photoreceptor cells where opsins (photopigments) are packaged, is highly absorbing to visible light. Therefore, illumination sources in the IR spectrum combined with red fluorescent dyes are ideal for depth imaging to prevent the autofluorescence generation/distortions in this tissue.

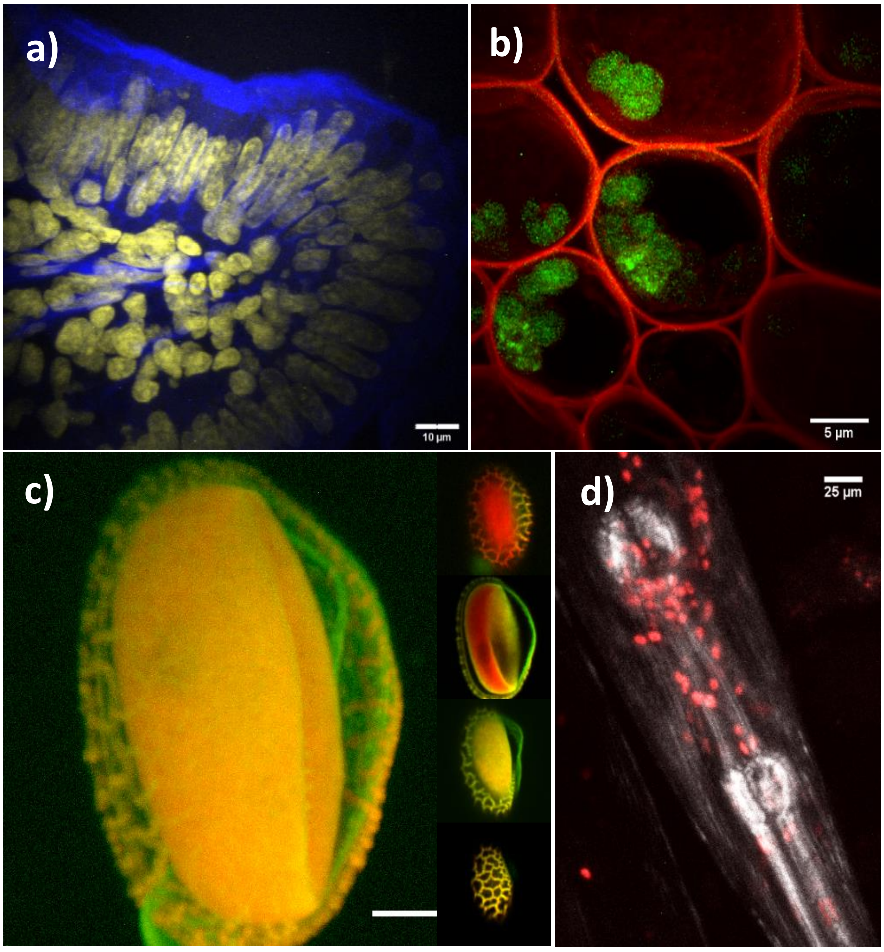


Figure 5.5. a) Maximum intensity (MAX) projection of 2PEF images of a mouse intestine section. Nuclei (yellow) and actin filaments (blue) are shown. Scalebar: 10 µm. b) MAX projection of a Z-stack of 2PEF images of a rhizome of Convallaria majalis. Chloroplasts (green) and cell walls (red) are shown. Scalebar: 5 µm. c) MAX projection of a Z-stack corresponding to 37 images (1.95 µm step spacing) of autofluorescence 2PEF images of a pollen grain. FITC (green) and TRITC (red) filtered signals. Yellow corresponds to the overlap of autofluorescence signal filtered with the FITC and TRITC filters. Scalebar: 10 µm. Selected frames from the same Z-stack. d) SUM projection of a Z-stack corresponding to 56 images (0.65 µm step spacing) of SHG signal of the muscle and pharynx (grey) and 2PEF from the neurons (red) of a living C. elegans (OH15500 strain). Scalebar: 25 µm.

To test the capability of our few-cycle all-fiber source to nonlinearly excite multiple markers we proceeded to acquire 2PEF images of multiple fluorophores: GFP, SYTOX Green, Alexa Fluor 568, tagRFP and Alexa Fluor 647. We also acquired SHG images of unlabeled tissues. Care was taken to use the corresponding filters for acquiring the 2PEF signals. Fig. 5.5 a) shows an image of a mouse intestine section stained with SYTOX Green (FITC filter) labelling the nuclei shown in yellow, and Alexa Fluor 568 phalloidin (TRITC filter) labelling the actin filaments shown in blue. Fig. 5.5 b) shows the rhizome of Convallaria majalis stained with Fast Green and Safranin. Chloroplasts are shown in green (FITC filter), and cell walls are shown in red (TRITC filter). In Fig. 5.5 c), it is also possible to see the autofluorescence of a pollen grain. The large emitted autofluorescence spectrum was detected using two different fluorescence filters, FITC filter shown in green and TRITC filter shown in red. We have also been able to image in vivo samples with cellular resolution. In particular, paralyzed C. elegans specimens. In Fig. 5.5 d), we can see a C. elegans OH15500 strain expressing tagRFP in all neurons. The SHG signal revealed all the different structures of the pharynx of the animal: corpus, isthmus and posterior bulb. Moreover, we can see the muscle fibers and their contraction during swallowing over time. These structures are a high-priced reference while imaging the neurons with 2PEF. By using different emission filters, we have been able to split the fluorescence from the different fluorophores to visualize multiple structures with a single illumination source.

Chapter 6

# Conclusions

In this thesis we have designed and fabricated monolithic fiber-optic supercontinuum (SC) sources at 1.06 μm and 1.5 μm central wavelengths (chapters 3 and 4, respectively). Then, we have characterized their output pulsed emission to determine, particularly, their temporal coherence properties. The 1.06 μm source has been integrated in a nonlinear optical (NLO) microscopy setup to demonstrate the advantages of using temporally coherent SC lasers as illumination source in this application (chapter 5).

In section 3.1 we have presented a monolithic fiber-optic source of transform-limited few-cycle pulses centered at 1.06 μm. Firstly, we have explained the different stages of the all-fiber femtosecond seed based on chirped pulse amplification technique, where we have used hollow-core photonic bandgap fiber technology in the pulse compression stage. The proposed architecture has allowed us to obtain output pulses of 200 fs temporal width at FWHM and 106.3 GW/cm$^2$ pulse peak intensity. Secondly, different samples of all-normal dispersion photonic crystal fibers (ANDi PCFs) were drawn and tested as stage for SC generation by exciting them with the developed all-fiber femtosecond seed. We have described the design of the target dispersion curve of the fibers, the definition of its target geometry and the fabrication method. By performing live tests of SC generation with some of the drawn samples we analyzed the nonlinear effects (NLE) involved in the broadening of the spectrum. With that, we could determine a well-defined hole diameter $d$ and pitch $\Lambda$ of the microstructure of the ANDi PCF for which the SC generation is led by self-phase modulation (SPM), successfully avoiding solitonic effects: d = 596 nm and Λ =

1615 nm. Finally, in the last part of this section we described the output stage of the few-cycle all-fiber temporally coherent SC source detailing how we find the suitable parameters to splice the last stage of the all-fiber seed to the ANDi PCF with best coupling efficiency. In section 3.2 we have presented the temporal compression of the source pulses, comparing the results obtained with the d-scan method and the interferometric autocorrelation method. We confirmed that the source is temporally coherent: according to the d-scan retrievals, we can compress the pulses to 12.97 fs, almost its Fourier transform limit (12.23 fs). This conclusion is backed up with the fact that the autocorrelation measurements provided a pulse of the same temporal width: 12.6 fs (3.7 cycles). In chapter 5 we have shown the performance of this few-cycle all-fiber source in multimodal and multispectral NLO microscopy. Imaging of different biological specimens was obtained by simultaneous two-photon excitation fluorescence (2PEF) of multiple fluorophores whose single-photon peak absorption wavelengths are in the band from 480 to 580 nm. Also, 2PEF and second-harmonic generation (SHG) techniques were combined to obtain images of neurons (via 2PEF) and of muscle and pharynx (via SHG) of living C. elegans specimens. The penetration depth capability of the few-cycle source was assessed by 2PEF imaging of transparent specimens (zebrafish embryos) and of scattering tissues (Wistar rat retina): an image of the full retina, of ~ 170 μm depth, was obtained with cellular resolution, showing better imaging resolution and depth than the image of the same sample acquired with a commercial Ti:Sa laser at a central wavelength of 810 nm.

In chapter 4 we have described a monolithic fiber-optic SC source centered at 1.5 μm. In the first section, section 4.1, we detailed the architecture of the seed used to excite the SC generation, which consisted of an all-fiber passively mode-locked oscillator followed by a Mach-Zehnder modulator and an erbium/ytterbium-doped fiber amplifier. The signal generated at the oscillator is modulated and amplified to optimize the SC exciting conditions. The seed delivers pulses of ~ 100 fs temporal width at FWHM centered at 1535 nm, of 2.1 W of average power at its natural repetition rate, 1.3 GHz. We performed a modulation to the train of pulses and characterized the seed at two different repetition rates: 650 MHz and 434 MHz, 1/2 and 1/3 of the natural frequency of the oscillator, respectively. In section 4.2 we studied the SC generation produced by the excitation of all-solid core graded-index (GRIN) fibers at different conditions of the seed. Different pieces of GRIN fibers with core diameters ranging between 5.8 and 6.3 μm were manufactured and tested. Their dispersion curves show zero-dispersion wavelengths (ZDWs) lower than the excitation wavelength $\lambda_0$ = 1535 nm. From the experimental and theoretical results herein presented, we have found the optimum SC spectrum by exciting very close to its ZDW (under anomalous dispersion region) pieces of lengths of ~ 25 cm of the 5.8 μm core diameter GRIN fiber with pulses of 120 fs temporal width at FWHM at a repetition rate of 434 MHz. To complete this section we have explained the numerical simulations performed using as input data the measured spectrum of the seed, its corresponding theoretical transform limited pulse duration and an effective peak power of 10 kW. The theoretical SC spectrum obtained from the generalized nonlinear Schrödinger equation qualitatively reproduced the experimental bandwidth of ~ 600 nm. Finally, in section 4.3 we have measured the degree of temporal coherence between two consecutive pulses and the autocorrelation of the pulses after they traverse a free-space wedges pulse compressor. We have found that the SC is generated through NLE that do not keep pulse-to-pulse temporal coherence. The measured degree of coherence is of ~ 0.7 in a band of 20 nm centered at 1535 nm, but it is almost 0 at any other wavelength out of the bandwidth of the seed. This was also confirmed by the temporal compression of the pulses. Should these pulses be coherent, according to the FTL of the measured spectrum, the pulses could be compressed down to 29 fs. On the contrary, the minimum temporal width obtained from the autocorrelation traces is 800 fs. Furthermore, the pulses present a noise-like shape with a 200 fs structure at the highest values of intensity of the autocorrelation trace and with > 800 fs wide pedestals. In conclusion, we have reported experimental SC generation at 1.5 μm central wavelength, achieving ~ 600 nm bandwidth by exciting all-solid core GRIN fibers close to their ZDW.

Regarding the industrial aspect of this thesis, the work presented in chapter 3 has resulted in a commercial source which is the all-fiber laser of the shortest pulses currently available on the market (Cyclone [182]). We have delivered several few-cycle all-fiber temporally coherent SC sources to customers such as the Italian Institute of Technology (IIT), the University of Rochester (UR) and the Massachusetts Institute of Technology (MIT). The IIT uses it as illumination source in a microscopy setup to obtain 2PEF images, while UR and MIT have integrated the laser in a microscopy setup to perform both 2PEF and SHG imaging. This source has also been selected as one of the three finalists in the 14$^{th}$ Annual Prism Awards for Photonics Innovation 2022, Scientific Lasers category, which are the international awards most relevant in the photonics industry.

Chapter 7

# Future work

The work carried out in this thesis has demonstrated that few-cycle supercontinuum can be obtained with all-fiber configurations and that they perform excellently in NLO microscopy. However, many challenges remain unsolved and several enhancing developments are advisable. In this chapter we outline some of them.

All-fiber lasers present characteristics that are powerful factors in favor of fiber technology: simplicity, robustness and cost-effectiveness. Traditional solid-state sources of few-cycle pulses can be replaced by all-fiber configurations in various applications due to these advantages. In chapters 3 and 4 we have described monolithic fiber sources that are/could potentially be great assets as illumination sources in NLO microscopy. The successful performance of our 1.06 μm source to provide high quality 2PEF and SHG microscopy images anticipates its utility in three-photon excitation fluorescence and third-harmonic generation (THG) microscopy, as well as in other NLO microscopy techniques, such as coherent anti-Stokes Raman scattering [183], multiphoton fluorescence lifetime imaging microscopy [184,185] and, consequently, in multimodal and multispectral combinations between all mentioned techniques. The central wavelength of ~ 1 μm is also more favorable for microscopy compared to the ~ 800 nm central wavelengths of Ti:Sa lasers, as it results in larger penetration depth in biological tissues and enables performing THG microscopy without going into the deep-UV, as would be the case of a central wavelength of ~ 800 nm. Utility of this type of source is anticipated also in applications of other disciplines that rely on the inherent properties of few-cycle pulses, such as ultrafast spectroscopy, optical frequency comb generation and frequency metrology [186–188]. We have presented pulse durations as short as 13.0 fs (3.7 cycles), with a central wavelength of 1.06 μm, but this is a non-fundamental limit that we expect to overcome with enhanced fiber manufacture precision to obtain flatter and nearer-to-zero dispersion curves of the ANDi PCFs. Further work can be done to improve the seed used to excite the ANDi PCFs, and the temporal compressor of the d-scan stage. Regarding the development of the seed, based on the all-fiber configuration reported here, the output average power can be increased to the few-watts level using exciting seeds of GHz-range repetition rates. With higher average power, the losses introduced by free-space optics of the microscopy setups using this laser as illumination source would impact less the performance of the source, and the integration time required for imaging applications would be reduced. About the dispersion management of the pulses at the output of the source, the current compressor could be modified to perform the dispersion management of the output pulses through means based on optical fiber components. For example, studying the possibility of using hollow core PCFs filled with gases [189–192]. These fibers can have their dispersion adjusted by controlling the pressure of the gas inside the fiber [193], which would allow to control the temporal width of the output pulses at the sample plane.

The SC source developed in chapter 4 needs to be further explored in order to achieve temporally coherent supercontinuum. The seed of this source delivers pulses of ~ 100 fs, but the temporal shape of the output pulses of the seed presents multipulse structure. This results in a low effective peak power of the seed used to excite the NL fibers (all-solid core GRIN fibers) where SC is generated. Also, the GRIN fibers manufactured to generate the SC spectrum have dispersion curves that present normal and anomalous dispersion regions, with a ZDW close to the excitation wavelength. The proximity between the ZDW and the excitation wavelength implies broadening mechanisms from NLE that do not keep the temporal coherence between pulses, i.e., solitonic effects and noise-originated NLE take part in the generation of the SC. Future work can be focused on the level of pulse-to-pulse temporal coherence of the source, attempting to increase it through the improvement of the NL fiber stage and the excitation conditions of the seed. Firstly, an option could be designing and manufacturing GRIN fibers with ANDi curves in a range of wavelengths of several hundreds of nanometers around the central wavelength of the seed used to excite them. In that case, NLE involved in the SC generation that do not conserve the temporal coherence of the pulses would be avoided. A different option could be the development of ANDi PCFs to excite them instead of using GRIN fibers. To avoid the high confinement losses presented by 1.5 μm PCFs, research on new designs with inner and outer rings of the cladding of different hole sizes [112] could be carried out. Secondly, it is possible to modulate the natural frequency of the seed to lower repetition rates and redesign the architecture of the amplifying stage. This stage could be built as a sequence of stages to have chirped pulse amplification of the pulses similarly to those of the architecture of the source from chapter 3. In this way, pulsed emission with a temporal shape corresponding to that of a truly single pulse could be expected.

Chapter 8

# Publications and awards

## 8.1. Publications related to the thesis

### 8.1.1. Journals

[1] B. Alonso, S. Torres-Peiró, R. Romero, P. T. Guerreiro, **A. Almagro-Ruiz**, H. Muñoz-Marco, P. Pérez-Millán and H. Crespo, 'Detection and elimination of pulse train instabilities in broadband fibre lasers using dispersion scan', *Scientific Reports*, vol. 10, 7242, 2020.

[2] **A. Almagro-Ruiz**, S. Torres-Peiró, H. Muñoz-Marco, M. Cunquero, G. Castro-Olvera, R. Dauliat, R. Jamier, O. V. Shulika, R. Romero, P. T. Guerreiro, M. Miranda, H. Crespo, P. Roy, P. Loza-Álvarez and P. Pérez-Millán, 'Few-cycle all-fiber supercontinuum laser for ultrabroadband multimodal nonlinear microscopy', *Optics Express*, vol. 30, no. 16, pp. 29044–29062, 2022.

[3] **A. Almagro-Ruiz**, D. Castelló-Lurbe, H. Muñoz-Marco, S. Torres-Peiró, S. Rota-Rodrigo, R. Dauliat, R. Jamier, P. Roy, J. Solis, P. Pérez-Millán, 'Study on Supercontinuum Generation Using Graded-Index Fibers at 1.5 μm', *Photonics Technology Letters* (submitted 01/06/2023).

### 8.1.2. Conferences

[1] **A. Almagro-Ruiz**, 'Desarrollo y aplicaciones de láseres de pulsos ultracortos de supercontinuo todo-fibra basados en fibras de cristal fotónico de dispersión todo-normal', in Jornada de Doctorandos de Física y Astrofísica de la UCM, Libro de resúmenes, Madrid, Spain, May 2020, p. 2.

[2] P. Pérez-Millán, S. Torres-Peiró, H. Muñoz-Marco and **A. Almagro-Ruiz**, 'Ultrafast fiber lasers in multiphoton science', in Photon 2020, Fr-11-2, London, UK – online, Sept. 2020.

[3] B. Alonso, S. Torres-Peiró, R. Romero, P. T. Guerreiro, **A. Almagro-Ruiz**, H. Muñoz-Marco, P. Pérez-Millán and H. Crespo, 'Detecting and quantifying pulse train instabilities with self-calibrating d-scan', in OSA Frontiers in Optics/Laser Science 2020, FTh1B.3, Washington D.C., EE.UU. – online, Sept. 2020.

[4] B. Alonso, S. Torres-Peiró, R. Romero, P. T. Guerreiro, **A. Almagro-Ruiz**, H. Muñoz-Marco, P. Pérez-Millán and H. Crespo, 'Experimental quantification of pulse train instabilities using dispersion scan', in The 22$^{nd}$ OSA International Conference on Ultrafast Phenomena, Tu4B.19, Beijing, China – online, Nov. 2020.

[5] **A. Almagro-Ruiz**, S. Torres-Peiró, H. Muñoz-Marco, R. Dauliat, R. Jamier, R. Romero, P. T. Guerreiro, M. Cunquero, G. Castro, P. Loza-Álvarez, H. Crespo, P. Roy and P. Pérez-Millán, 'Few-cycle all-fiber temporally coherent supercontinuum sources', Proc. of SPIE LASE, Frontiers in Ultrafast Optics: Biomedical, Scientific and Industrial Applications XXI, vol. 11676, 11676M-7, San Francisco, EE.UU. – online, March 2021.

[6] **A. Almagro-Ruiz**, S. Torres-Peiró, H. Muñoz-Marco, R. Dauliat, R. Jamier, R. Romero, P. T. Guerreiro, M. Cunquero, G. Castro-Olvera, P. Loza-Álvarez, H. Crespo, P. Roy and P. Pérez-Millán, 'Few-cycle all-fiber temporally coherent supercontinuum sources. Nonlinear microscopy applications', in XII Reunión Nacional de Optoelectrónica, OPTOEL'21, Fr2.1, virtual event, July 2021.

[7] **A. Almagro-Ruiz**, S. Torres-Peiró, H. Muñoz-Marco, M. Cunquero, G. Castro-Olvera, R. Dauliat, R. Jamier, R. Romero, P. T. Guerreiro, M. Miranda, H. Crespo, P. Roy, P. Loza-Álvarez and P. Pérez-Millán, '15 fs all-fiber supercontinuum source and its application to multimodal nonlinear microscopy', in XIII Reunión Nacional de Óptica, RNO 21, Proc. 225, , virtual event, Nov. 2021, pp. 292-293.

## 8.2. Other publications

[1] **A. Almagro-Ruiz**, V. Otgon, A. Ortigosa-Claveria, J. Abreu-Afonso and P. Pérez-Millán, ‘Benefits of the Arbitrary Shaping of Fiber Laser Pulse Properties in the Pulsed Laser Ablation on Liquid Technique’, in $1^{st}$ International Conference on Nanofluids, ICNf2019, Castellón, Spain, June 2019, pp. 544-546.

[2] **A. Almagro-Ruiz**, J. Abreu-Afonso, S. Torres-Peiró, A. Ortigosa-Claveria, A. G. de la Reina-Carrió, V. Otgon and P. Pérez Millán, ‘Pulse compression and burst function in a picosecond high-power fiber laser’, in XI Reunión Española de Optoelectrónica, OPTOEL’19, SP1.LAS03, Zaragoza, Spain, July 2019.

[3] H. Muñoz-Marco, **A. Almagro-Ruiz** and P. Pérez-Millán, ‘1550 nm Femtosecond Fiber Laser System for the Two-Photon Excitation of Transient Currents in Semiconductors Detectors’, in The $36^{th}$ RD50 Workshop (CERN – online Workshop), June 2020, p. 1.

[4] **A. Almagro-Ruiz**, H. Muñoz-Marco and P. Pérez-Millán, ‘Towards an All-Fiber Femtosecond Laser System as Excitation Source in the Two-Photon Absorption-Transient Current Technique’, in The $39^{th}$ RD50 Workshop, Proc. 5, Valencia, Spain, Nov. 2021, pp. 2-3.

[5] **A. Almagro-Ruiz**, S. Pape, H. Muñoz-Marco, M. Wiehe, E. Currás, M. Fernández-García, M. Moll, R. Montero, F. R. Palomo, C. Quintana, I. Vila and P. Pérez-Millán, ‘Fiber laser system of 1550 nm femtosecond pulses with configurable properties for the two-photon excitation of transient currents in semiconductor detectors’, Applied Optics, vol. 61, no. 32, pp. 9386-9397, 2022.

## 8.3. Awards

Few-cycle temporally coherent supercontinuum source (Cyclone) finalist of the $14^{th}$ Annual SPIE Prism Awards for Photonics Innovation 2022, Scientific Lasers category; Photonic West, San Francisco, 2022.

ANNEX

# Instrumentation

For every measurement of average power reported in chapters 3 and 4 we use a high power (up to 10 W) and a low power (up to 1 W) thermal sensor from Thorlabs, models S425C and S401C, respectively. We also use two different photodiode power sensors from Thorlabs to measure average power values up to 20 mW: models S151C and S155C for wavelength ranges of measurement from 400 – 110 nm and 800 – 1700 nm, respectively. To measure the temporal widths of each stage of both sources and the autocorrelation traces shown in Fig. 4.4 and 4.8 we use an intensity autocorrelator from Femtochrome Research, model FR-103XL, together with an oscilloscope of 1 GHz bandwidth from Tektronix, model MDO34. For Fig. 3.13, 4.9, and 5.2 we use an interferometric autocorrelator from the same manufacturer, model FR-103TPM. Trains of pulses reported in chapter 4 are measured with an oscilloscope of 2 GHz bandwidth from Rode & Schwarz, model RTO2024, using a photodetector of 5 GHz bandwidth from Thorlabs, model DET08CFC. Every spectral trace from chapters 3 and 4 of optical spectra contained in wavelength ranges from 350 – 1200 nm are measured with an optical spectrum analyzer from Yokogawa, model AQ6373B; for those contained in wavelength ranges from 1200 – 2400 nm: model AQ6375B. Between non-polarization maintaining fibers, splices are performed with the splicer machine from Fujikura, model 70S; when one of the fibers or both are polarization maintaining: model FSM 100P. Microscope images of the sections of the photonic crystal fibers used in chapter 3 are obtained with a scanning electron microscope from Zeiss, model Ultra 55.

# References


[1] R. R. Alfano and S. L. Shapiro, 'Emission in the Region 4000 To 7000 Å Via Four-Photon Coupling in Glass', *Phys. Rev. Lett.*, vol. 24, no. 11, pp. 584–588, 1970.

[2] N. G. Bondarenko, I. V. Eremina, and V. I. Talanov, 'Broadening of spectrum in self-focusing of light in crystals', *Pis'ma Zh. Eksp. Teor. Fiz.*, vol. 12, pp. 125–128, 1970.

[3] Ö. Boyraz, J. Kim, M. N. Islam, F. Coppinger, and B. Jalali, '10 Gb/s Multiple Wavelength, Coherent Short Pulse Source Based on Spectral Carving of Supercontinuum Generated in Fibers', *J. Light. Technol.*, vol. 18, no. 12, pp. 2167–2175, 2000.

[4] H. Sotobayashi and K. Kitayama, '325nm bandwidth supercontinuum generation at 10Gbit/s using dispersion-flattened and non-decreasing normal dispersion fibre with pulse compression technique', *Electron. Lett.*, vol. 34, no. 13, pp. 1336–1337, 1998.

[5] S. Xing, A. S. Kowligy, D. M. B. Lesko, A. J. Lind, and S. A. Diddams, 'All-fiber frequency comb at 2 μm providing 1.4-cycle pulses', *Opt. Lett.*, vol. 45, no. 9, pp. 2660–2663, 2020.

[6] Y. Okawachi, M. Yu, J. Cardenas, X. Ji, M. Lipson, and A. L. Gaeta, 'Coherent, directional supercontinuum generation', *Opt. Lett.*, vol. 42, no. 21, pp. 4466–4469, Nov. 2017.

[7] T. Udem, R. Holzwarth, and T. W. Hänsch, 'Optical frequency metrology', *Nature*, vol. 416, no. 3, pp. 233–237, Mar. 2002.

[8] H. Timmers *et al.*, 'Molecular fingerprinting with bright, broadband infrared frequency combs', *Optica*, vol. 5, no. 6, pp. 727–732, Jun. 2018.

[9] A. M. Heidt *et al.*, 'High quality sub-two cycle pulses from compression of supercontinuum generated in all-normal dispersion photonic crystal fiber', *Opt. Express*, vol. 19, no. 15, pp. 13873–13879, Jul. 2011.

[10] D. G. Purdie *et al.*, 'Few-cycle pulses from a graphene mode-locked all-fiber laser', *Appl. Phys. Lett.*, vol. 106, no. 25, p. 253101, 2015.

[11] S. Demmler *et al.*, 'Generation of high quality, 1.3 cycle pulses by active phase control of an octave spanning supercontinuum', *Opt. Express*, vol. 19, no. 21, pp. 20151–20158, Oct. 2011.

[12] S. Rao D. S. *et al.*, 'Shot-noise limited, supercontinuum-based optical coherence tomography', *Light Sci. Appl.*, vol. 10, no. 133, pp. 1–13, Jun. 2021.

[13] B. Povazay *et al.*, 'Submicrometer axial resolution optical coherence

tomography', *Opt. Lett.*, vol. 27, no. 20, pp. 1800–1802, 2002.

[14] I. Pope, W. Langbein, P. Watson, and P. Borri, 'Simultaneous hyperspectral differential-CARS, TPF and SHG microscopy with a single 5 fs Ti:Sa laser', *Opt. Express*, vol. 21, no. 6, pp. 7096–7106, 2013.

[15] C. Maibohm *et al.*, 'SyncRGB-FLIM: synchronous fluorescence imaging of red, green and blue dyes enabled by ultra-broadband few-cycle laser excitation and fluorescence lifetime detection', *Biomed. Opt. Express*, vol. 10, no. 4, pp. 1891–1904, 2019.

[16] C. Xu and F. W. Wise, 'Recent advances in fibre lasers for nonlinear microscopy', *Nat. Photonics*, vol. 7, no. 11, pp. 875–882, 2013.

[17] C. R. Petersen *et al.*, 'Mid-infrared multispectral tissue imaging using a chalcogenide fiber supercontinuum source', *Opt. Lett.*, vol. 43, no. 5, pp. 999–1002, 2018.

[18] K. Tai, A. Hasegawa, and N. Bekki, 'Fission of optical solitons induced by stimulated Raman effect', *Opt. Lett.*, vol. 13, no. 5, pp. 392–394, 1988.

[19] P. Beaud, W. Hodel, B. Zysset, and H. P. Weber, 'Ultrashort pulse propagation, pulse breakup, and fundamental soliton formation in a single-mode optical fiber', *IEEE J. Quantum Electron.*, vol. 23, no. 11, pp. 1938–1946, 1987.

[20] J. N. Kutz, C. Lyngå, and B. J. Eggleton, 'Enhanced Supercontinuum Generation through Dispersion-Management', *Opt. Express*, vol. 13, no. 11, pp. 3989–3998, 2005.

[21] D. R. Austin, C. M. de Sterke, B. J. Eggleton, and T. G. Brown, 'Dispersive wave blue-shift in supercontinuum generation', *Opt. Express*, vol. 14, no. 25, pp. 11997–12007, 2006.

[22] I. Cristiani, R. Tediosi, L. Tartara, and V. Degiorgio, 'Dispersive wave generation by solitons in microstructured optical fibers', *Opt. Express*, vol. 12, no. 1, pp. 124–135, 2004.

[23] A. Efimov *et al.*, 'Interaction of an Optical Soliton with a Dispersive Wave', *Phys. Rev. Lett.*, vol. 95, no. 21, p. 213902, 2005.

[24] R. H. Stolen, C. Lee, and R. K. Jain, 'Development of the stimulated Raman spectrum in single-mode silica fibers', *J. Opt. Soc. Am. B*, vol. 1, no. 4, pp. 652–657, 1984.

[25] S. C. Pinault and M. J. Potasek, 'Frequency broadening by self-phase modulation in optical fibers', *J. Opt. Soc. Am. B*, vol. 2, no. 8, pp. 1318–1319, 1985.

[26] K. R. Tamura, H. Kubota, and M. Nakazawa, 'Fundamentals of stable continuum generation at high repetition rates', *IEEE J. Quantum Electron.*, vol. 36, no. 7, pp. 773–779, 2000.

[27] T. Hori, N. Nishizawa, T. Goto, and M. Yoshida, 'Experimental and numerical analysis of widely broadened supercontinuum generation in highly nonlinear dispersion-shifted fiber with a femtosecond pulse', *J. Opt.*

*Soc. Am. B*, vol. 21, no. 11, pp. 1969–1978, 2004.

[28] A. V. Yulin, D. V. Skryabin, and P. S. J. Russell, 'Four-wave mixing of linear waves and solitons in fibers with higher-order dispersion', *Opt. Lett.*, vol. 29, no. 20, pp. 2411–2413, 2004.

[29] V. P. Yanovsky and F. W. Wise, 'Nonlinear propagation of high-power, sub-100-fs pulses near the zero-dispersion wavelength of an optical fiber', *Opt. Lett.*, vol. 19, no. 19, pp. 1547–1549, 1994.

[30] J. M. Dudley, G. Genty, and S. Coen, 'Supercontinuum generation in photonic crystal fiber', *Rev. Mod. Phys.*, vol. 78, no. 4, pp. 1135–1184, 2006.

[31] G. P. Agrawal, *Nonlinear fiber optics*. Amsterdam ; Elsevier / Academic Press, 2007.

[32] A. L. Gaeta, 'Nonlinear propagation and continuum generation in microstructured optical fibers', *Opt. Lett.*, vol. 27, no. 11, pp. 924–926, 2002.

[33] A. M. Zheltikov, 'Nonlinear optics of microstructure fibers', *Physics-Uspekhi*, vol. 47, no. 1, pp. 69–98, 2004.

[34] D. K. Mynbaev and L. L. Scheiner, *Fiber-optic communications technology*. Prentice Hall, 2001.

[35] M. A. Saifi, S. J. Jang, L. G. Cohen, and J. Stone, 'Triangular-profile single-mode fiber', *Opt. Lett.*, vol. 7, no. 1, pp. 43–45, 1982.

[36] R. Tewari, B. P. Pal, and U. K. Das, 'Dispersion-Shifted Dual-Shape Core Fibers: Optimization Based on Spot Size Definitions', *J. Light. Technol.*, vol. 10, no. 1, pp. 1–5, 1992.

[37] E. Yablonovitch, 'Inhibited Spontaneous Emission in Solid-State Physics and Electronics', *Phys. Rev. Lett.*, vol. 58, no. 20, pp. 2059–2062, 1987.

[38] J. C. Knight, 'Photonic crystal fibres', *Nature*, vol. 424, no. 8, pp. 847–851, 2003.

[39] J. C. Knight, J. Broeng, T. A. Birks, and P. S. J. Russell, 'Photonic Band Gap Guidance in Optical Fibers', *Science (80-. ).*, vol. 282, no. 5393, pp. 1476–1478, 1998.

[40] R. F. Cregan *et al.*, 'Single-Mode Photonic Band Gap Guidance of Light in Air', *Science (80-. ).*, vol. 285, no. 5433, pp. 1537–1539, 1999.

[41] D. Strickland and G. Mourou, 'Compression of amplified chirped optical pulses', *Opt. Commun.*, vol. 56, no. 3, pp. 219–221, 1985.

[42] S. Hädrich, J. Rothhardt, T. Eidam, and J. Limpert, 'Hollow-core fiber compression of high repetition rate fiber CPA systems', in *Advanced Solid-State Photonics*, 2009, pp. 1–3.

[43] J. C. Knight, T. A. Birks, P. S. J. Russell, and D. M. Atkin, 'All-silica single-mode optical fiber with photonic crystal cladding', *Opt. Lett.*, vol. 21, no. 19, pp. 1547–1549, 1996.

[44] T. A. Birks, J. C. Knight, and P. S. J. Russell, 'Endlessly single-mode photonic crystal fiber', *Opt. Lett.*, vol. 22, no. 13, pp. 961–963, 1997.

[45] P. S. J. Russell, 'Photonic Crystal Fibers', *Science (80-. ).*, vol. 299, no. 5605,

pp. 358–362, 2003.
[46] P. J. Roberts *et al.*, 'Control of dispersion in photonic crystal fibers', *J. Opt. Fiber Commun. Reports*, vol. 2, no. 5, pp. 435–461, 2005.
[47] D. Mogilevtsev, T. A. Birks, and P. S. J. Russell, 'Group-velocity dispersion in photonic crystal fibers', *Opt. Lett.*, vol. 23, no. 21, pp. 1662–1664, 1998.
[48] J. C. Knight, J. Arriaga, T. A. Birks, A. Ortigosa-Blanch, W. J. Wadsworth, and P. S. J. Russell, 'Anomalous Dispersion in Photonic Crystal Fiber', *IEEE Photonics Technol. Lett.*, vol. 12, no. 7, pp. 807–809, 2000.
[49] M. Diouf, A. Wague, and M. Zghal, 'Numerical investigation of an ultra-broadband coherent mid-infrared supercontinuum in a chalcogenide AsSe2-As2S5 multimaterial photonic crystal fiber', *J. Opt. Soc. Am. B*, vol. 36, no. 2, pp. A8–A14, 2019.
[50] W. H. Reeves, J. C. Knight, P. S. J. Russell, and P. J. Roberts, 'Demonstration of ultra-flattened dispersion in photonic crystal fibers', *Opt. Express*, vol. 10, no. 14, pp. 609–613, 2002.
[51] A. Ferrando, E. Silvestre, P. Andrés, J. Miret, and M. Andrés, 'Designing the properties of dispersion-flattened photonic crystal fibers', *Opt. Express*, vol. 9, no. 13, pp. 687–697, 2001.
[52] M. L. V. Tse *et al.*, 'Supercontinuum generation at 1.06 μm in holey fibers with dispersion flattened profiles', *Opt. Express*, vol. 14, no. 10, pp. 4445–4451, 2006.
[53] K. M. Hilligsøe *et al.*, 'Supercontinuum generation in a photonic crystal fiber with two zero dispersion wavelengths', *Opt. Express*, vol. 12, no. 6, pp. 1045–1054, 2004.
[54] K. Saitoh and M. Koshiba, 'Highly nonlinear dispersion-flattened photonic crystal fibers for supercontinuum generation in a telecommunication window', *Opt. Express*, vol. 12, no. 10, pp. 2027–2032, 2004.
[55] E. P. Ippen and R. H. Stolen, 'Stimulated Brillouin scattering in optical fibers', *Appl. Phys. Lett.*, vol. 21, no. 11, pp. 539–541, 1972.
[56] R. H. Stolen and A. Ashkin, 'Optical Kerr effect in glass waveguide', *Appl. Phys. Lett.*, vol. 22, no. 6, pp. 294–296, 1973.
[57] R. H. Stolen and C. Lin, 'Self-phase-modulation in silica optical fibers', *Phys. Rev. A*, vol. 17, no. 4, pp. 1448–1453, 1978.
[58] G. P. Agrawal, 'Nonlinear fiber optics: its history and recent progress [Invited]', *J. Opt. Soc. Am. B*, vol. 28, no. 12, pp. A1–A10, 2011.
[59] L. F. Mollenauer, R. H. Stolen, and J. P. Gordon, 'Experimental Observation of Picosecond Pulse Narrowing and Solitons in Optical Fibers', *Phys. Rev. Lett.*, vol. 45, no. 13, pp. 1095–1098, 1980.
[60] J. C. Travers, 'Blue extension of optical fibre supercontinuum generation', *J. Opt.*, vol. 12, no. 11, p. 113001, 2010.
[61] A. V. Husakou and J. Herrmann, 'Supercontinuum Generation of Higher-Order Solitons by Fission in Photonic Crystal Fibers', *Phys. Rev. Lett.*, vol.

87, no. 20, p. 203901, 2001.
[62] N. Akhmediev and M. Karlsson, 'Cherenkov radiation emitted by solitons in optical fibers', *Phys. Rev. A*, vol. 51, no. 3, pp. 2602–2607, 1995.
[63] D. V. Skryabin and A. V. Gorbach, 'Colloquium: Looking at a soliton through the prism of optical supercontinuum', *Rev. Mod. Phys.*, vol. 82, no. 2, pp. 1287–1299, 2010.
[64] X. Liu *et al.*, 'Soliton self-frequency shift in a short tapered air-silica microstructure fiber', *Opt. Lett.*, vol. 26, no. 6, pp. 358–360, 2001.
[65] F. M. Mitschke and L. F. Mollenauer, 'Discovery of the soliton self-frequency shift', *Opt. Lett.*, vol. 11, no. 10, pp. 659–661, 1986.
[66] Y. Matsui, M. D. Pelusi, and A. Suzuki, 'Generation of 20-fs Optical Pulses from a Gain-Switched Laser Diode by a Four-Stage Soliton Compression Technique', *IEEE Photonics Technol. Lett.*, vol. 11, no. 10, pp. 1217–1219, 1999.
[67] N. Nishizawa, Y. Ito, and T. Goto, 'Wavelength-Tunable Femtosecond Soliton Pulse Generation for Wavelengths of 0.78-1.0 μm Using Photonic Crystal Fibers and a Ultrashort Fiber Laser', *Jpn. J. Appl. Phys.*, vol. 42, no. 2A, pp. 449–452, 2003.
[68] E. M. Dianov *et al.*, 'Stimulated-Raman conversion of multisoliton pulses in quartz optical fibers', *Pis'ma Zh. Eksp. Teor. Fiz.*, vol. 41, no. 6, pp. 242–244, 1985.
[69] J. Takayanagi, N. Nishizawa, H. Nagai, M. Yoshida, and T. Goto, 'Generation of High-Power Femtosecond Pulse and Octave-Spanning Ultrabroad Supercontinuum Using All-Fiber System', *IEEE Photonics Technol. Lett.*, vol. 17, no. 1, pp. 37–39, 2005.
[70] M. Nakazawa, K. Suzuki, H. Kubota, and H. A. Haus, 'High-order solitons and the modulational instability', *Phys. Rev. A*, vol. 39, no. 11, pp. 5768–5776, 1989.
[71] K. Tai, A. Hasegawa, and A. Tomita, 'Observation of Modulational Instability in Optical Fibers', *Phys. Rev. Lett.*, vol. 56, no. 2, pp. 135–138, 1986.
[72] M. Nakazawa, K. Tamura, H. Kubota, and E. Yoshida, 'Coherence Degradation in the Process of Supercontinuum Generation in an Optical Fiber', *Opt. Fiber Technol.*, vol. 4, no. 2, pp. 215–223, 1998.
[73] H. Kubota, K. R. Tamura, and M. Nakazawa, 'Analyses of coherence-maintained ultrashort optical pulse trains and supercontinuum generation in the presence of soliton–amplified spontaneous-emission interaction', *J. Opt. Soc. Am. B*, vol. 16, no. 12, pp. 2223–2232, 1999.
[74] M. Bellini and T. W. Hänsch, 'Phase-locked white-light continuum pulses: toward a universal optical frequency-comb synthesizer', *Opt. Lett.*, vol. 25, no. 14, pp. 1049–1051, 2000.
[75] S. V. Smirnov, J. D. Ania-Castanon, T. J. Ellingham, S. M. Kobtsev, S.

Kukarin, and S. K. Turitsyn, 'Optical spectral broadening and supercontinuum generation in telecom applications', *Opt. Fiber Technol.*, vol. 12, no. 2, pp. 122–147, 2006.
[76] J. Herrmann *et al.*, 'Experimental Evidence for Supercontinuum Generation by Fission of Higher-Order Solitons in Photonic Fibers', *Phys. Rev. Lett.*, vol. 88, no. 17, p. 173901, 2002.
[77] D. Türke, S. Pricking, A. Husakou, J. Teipel, J. Herrmann, and H. Giessen, 'Coherence of subsequent supercontinuum pulses generated in tapered fibers in the femtosecond regime', *Opt. Express*, vol. 15, no. 5, pp. 2732–2741, 2007.
[78] S. Kim, J. Park, S. Han, Y.-J. Kim, and S.-W. Kim, 'Coherent supercontinuum generation using Er-doped fiber laser of hybrid mode-locking', *Opt. Lett.*, vol. 39, no. 10, pp. 2986–2989, 2014.
[79] X. Gu *et al.*, 'Experimental studies of the coherence of microstructure-fiber supercontinuum', *Opt. Express*, vol. 11, no. 21, pp. 2697–2703, 2003.
[80] F. Lu and W. H. Knox, 'Generation of a broadband continuum with high spectral coherence in tapered single-mode optical fibers', *Opt. Express*, vol. 12, no. 2, pp. 347–353, 2004.
[81] D. Castelló-Lurbe, N. Vermeulen, and E. Silvestre, 'Towards an analytical framework for tailoring supercontinuum generation', *Opt. Express*, vol. 24, no. 23, pp. 26629–26645, 2016.
[82] Y. Liu, H. Tu, and S. A. Boppart, 'Wave-breaking-extended fiber supercontinuum generation for high compression ratio transform-limited pulse compression', *Opt. Lett.*, vol. 37, no. 12, pp. 2172–2174, 2012.
[83] P. L. Baldeck and R. R. Alfano, 'Intensity Effects on the Stimulated Four Photon Spectra Generated by Picosecond Pulses in Optical Fibers', *J. Light. Technol.*, vol. 5, no. 12, pp. 1712–1715, 1987.
[84] G. Genty, M. Lehtonen, and H. Ludvigsen, 'Effect of cross-phase modulation on supercontinuum generated in microstructured fibers with sub-30 fs pulses', *Opt. Express*, vol. 12, no. 19, pp. 4614–4624, 2004.
[85] B. Alonso *et al.*, 'Detection and elimination of pulse train instabilities in broadband fibre lasers using dispersion scan', *Sci. Rep.*, vol. 10, p. 7242, 2020.
[86] J. K. Ranka, R. S. Windeler, and A. J. Stentz, 'Visible continuum generation in air-silica microstructure optical fibers with anomalous dispersion at 800 nm', *Opt. Lett.*, vol. 25, no. 1, pp. 25–27, 2000.
[87] T. A. Birks, W. J. Wadsworth, and P. S. J. Russell, 'Supercontinuum generation in tapered fibers', *Opt. Lett.*, vol. 25, no. 19, pp. 1415–1417, 2000.
[88] J. M. Dudley and S. Coen, 'Coherence properties of supercontinuum spectra generated in photonic crystal and tapered optical fibers', *Opt. Lett.*, vol. 27, no. 13, pp. 1180–1182, 2002.
[89] J. W. Nicholson *et al.*, 'All-fiber, octave-spanning supercontinuum', *Opt.*

*Express*, vol. 28, no. 8, pp. 643–645, 2003.

[90] K. M. Hilligsøe, H. N. Paulsen, J. Thøgersen, S. R. Keiding, and J. J. Larsen, 'Initial steps of supercontinuum generation in photonic crystal fibers', *J. Opt. Soc. Am. B*, vol. 20, no. 9, pp. 1887–1893, 2003.

[91] L. Yin, Q. Lin, and G. P. Agrawal, 'Soliton fission and supercontinuum generation in silicon waveguides', *Opt. Lett.*, vol. 32, no. 4, pp. 391–393, 2007.

[92] F. Leo *et al.*, 'Dispersive wave emission and supercontinuum generation in a silicon wire waveguide pumped around the 1550 nm telecommunication wavelength', *Opt. Lett.*, vol. 39, no. 12, pp. 3623–3626, 2014.

[93] K. L. Corwin *et al.*, 'Fundamental Noise Limitations to Supercontinuum Generation in Microstructure Fiber', *Phys. Rev. Lett.*, vol. 90, no. 11, p. 113904, 2003.

[94] J. M. Dudley and S. Coen, 'Fundamental limits to few-cycle pulse generation from compression of supercontinuum spectra generated in photonic crystal fiber', *Opt. Express*, vol. 12, no. 11, pp. 2423–2428, 2004.

[95] R. Holzwarth, T. Udem, T. W. Hänsch, J. C. Knight, W. J. Wadsworth, and P. S. J. Russell, 'Optical Frequency Synthesizer for Precision Spectroscopy', *Phys. Rev. Lett.*, vol. 85, no. 11, pp. 2264–2267, Sep. 2000.

[96] Y. Liu, H. Tu, W. A. Benalcazar, E. J. Chaney, and S. A. Boppart, 'Multimodal Nonlinear Microscopy by Shaping a Fiber Supercontinuum From 900 to 1160 nm', *IEEE J. Sel. Top. Quantum Electron.*, vol. 18, no. 3, pp. 1209–1214, 2012.

[97] Y. Liu, M. D. King, H. Tu, Y. Zhao, and S. A. Boppart, 'Broadband nonlinear vibrational spectroscopy by shaping a coherent fiber supercontinuum', *Opt. Express*, vol. 21, no. 7, pp. 8269–8275, 2013.

[98] A. M. Heidt, 'Pulse preserving flat-top supercontinuum generation in all-normal dispersion photonic crystal fibers', *J. Opt. Soc. Am. B*, vol. 27, no. 3, pp. 550–559, 2010.

[99] A. Hartung, A. M. Heidt, and H. Bartelt, 'Design of all-normal dispersion microstructured optical fibers for pulse-preserving supercontinuum generation', *Opt. Express*, vol. 19, no. 8, pp. 7742–7749, 2011.

[100] L. E. Hooper, P. J. Mosley, A. C. Muir, W. J. Wadsworth, and J. C. Knight, 'Coherent supercontinuum generation in photonic crystal fiber with all-normal group velocity dispersion', *Opt. Express*, vol. 19, no. 6, pp. 4902–4907, 2011.

[101] M. Klimczak, B. Siwicki, A. Heidt, and R. Buczyński, 'Coherent supercontinuum generation in soft glass photonic crystal fibers', *Photonics Res.*, vol. 5, no. 6, pp. 710–727, 2017.

[102] I. A. Sukhoivanov, S. O. Iakushev, O. V. Shulika, E. Silvestre, and M. V. Andrés, 'Design of All-Normal Dispersion Microstructured Optical Fiber on Silica Platform for Generation of Pulse-Preserving Supercontinuum

Under Excitation at 1550 nm', *J. Light. Technol.*, vol. 35, no. 17, pp. 3772–3779, 2017.

[103] N. Nishizawa, T. Niinomi, Y. Nomura, L. Jin, and Y. Ozeki, 'Octave Spanning Coherent Supercontinuum Comb Generation Based on Er-Doped Fiber Lasers and Their Characterization', *IEEE J. Sel. Top. Quantum Electron.*, vol. 24, no. 3, p. 5100409, 2018.

[104] C. Huang *et al.*, 'Asterisk-shaped microstructured fiber for an octave coherent supercontinuum in a sub-picosecond region', *Opt. Lett.*, vol. 43, no. 3, pp. 486–489, 2018.

[105] C. Fourcade-Dutin and D. Bigourd, 'Near Infrared tunable source delivering ultra-short pulses based on an all normal dispersion fiber and a zero dispersion line', *Appl. Phys. B Lasers Opt.*, vol. 124, no. 154, pp. 1–5, 2018.

[106] N. Nishizawa and J. Takayanagi, 'Octave spanning high-quality supercontinuum generation in all-fiber system', *J. Opt. Soc. Am. B*, vol. 24, no. 8, pp. 1786–1792, 2007.

[107] A. M. Heidt *et al.*, 'Coherent octave spanning near-infrared and visible supercontinuum generation in all-normal dispersion photonic crystal fibers', *Opt. Express*, vol. 19, no. 4, pp. 3775–3787, 2011.

[108] M. Klimczak *et al.*, 'Coherent supercontinuum generation up to 2.3 μm in all-solid soft-glass photonic crystal fibers with flat all-normal dispersion', *Opt. Express*, vol. 22, no. 15, pp. 18824–18832, 2014.

[109] K. Tarnowski, T. Martynkien, P. Mergo, K. Poturaj, G. Soboń, and W. Urbańczyk, 'Coherent supercontinuum generation up to 2.2 μm in an all-normal dispersion microstructured silica fiber', *Opt. Express*, vol. 24, no. 26, pp. 30523–30536, 2016.

[110] C. Huang *et al.*, 'Ultraflat, broadband, and highly coherent supercontinuum generation in all-solid microstructured optical fibers with all-normal dispersion', *Photonics Res.*, vol. 6, no. 6, pp. 601–608, 2018.

[111] M. L. Ferhat, L. Cherbi, and I. Haddouche, 'Supercontinuum generation in silica photonic crystal fiber at 1.3 μm and 1.65 μm wavelengths for optical coherence tomography', *Optik (Stuttg).*, vol. 152, no. 1, pp. 106–115, 2018.

[112] S. Rao D. S. *et al.*, 'Ultra-low-noise supercontinuum generation with a flat near-zero normal dispersion fiber', *Opt. Lett.*, vol. 44, no. 9, pp. 2216–2219, 2019.

[113] C. Cheng, Y. Zeng, Y. Ou, Z. Yang, and Z. Chen, 'Flatly Broadened and Highly Coherent Supercontinuum Generation by Induced Modulation Instability in ANDi-PCF', *J. Appl. Math. Phys.*, vol. 6, no. 4, pp. 640–646, 2018.

[114] Y. Nozaki, Y. Nomura, M. Aramaki, and N. Nishizawa, 'Octave spanning coherent supercontinuum generation using 51 fs high-power ultrashort pulse from Er-doped similariton amplifier', *Jpn. J. Appl. Phys.*, vol. 53, no.

2, p. 020301, 2014.

[115] K. K. Chow, Y. Takushima, C. Lin, C. Shu, and A. Bjarklev, 'Flat supercontinuum generation based on normal dispersion nonlinear photonic crystal fibre', *Electron. Lett.*, vol. 42, no. 17, pp. 989–991, 2006.

[116] C. Poudel and C. F. Kaminski, 'Supercontinuum radiation in fluorescence microscopy and biomedical imaging applications', *J. Opt. Soc. Am. B*, vol. 36, no. 2, pp. A139–A153, 2019.

[117] H. Tu and S. A. Boppart, 'Coherent fiber supercontinuum for biophotonics', *Laser Phot. rev.*, vol. 7, no. 5, pp. 1–33, 2013.

[118] B. Alonso Fernández *et al.*, *El láser: la luz de nuestro tiempo*, 1st ed. Salamanca, 2010.

[119] M. E. Fermann, D. C. Hanna, D. P. Shepherd, P. J. Suni, and J. E. Townsend, 'Efficient operation of an Yb-sensitised Er fibre laser at 1.56 μm', *Electron. Lett.*, vol. 24, no. 18, pp. 1135–1136, 1988.

[120] J. F. Philipps, T. Töpfer, H. Ebendorff-Heidepriem, D. Ehrt, and R. Sauerbrey, 'Energy transfer and upconversion in erbium-ytterbium-doped fluoride phosphate glasses', *Appl. Phys. B Lasers Opt.*, vol. 74, no. 3, pp. 233–236, 2002.

[121] P. W. Milonni and J. H. Eberly, *LASER PHYSICS*. New Jersey: Wiley, 2010.

[122] H. Muñoz-Marco, '1.5 μm ultrafast fiber lasers of repetition rates from single shot to GHz range', 2021.

[123] A. Cabasse, G. Martel, and J. L. Oudar, 'High power dissipative soliton in an Erbium-doped fiber laser mode-locked with a high modulation depth saturable absorber mirror', *Opt. Express*, vol. 17, no. 12, pp. 9537–9542, 2009.

[124] N. N. Akhmediev, A. Ankiewicz, M. J. Lederer, and B. Luther-Davies, 'Ultrashort pulses generated by mode-locked lasers with either a slow or a fast saturable-absorber response', *Opt. Lett.*, vol. 23, no. 4, pp. 280–282, 1998.

[125] E. A. DeSouza *et al.*, 'Saturable absorber mode locked polarisation maintaining erbium-doped fibre laser', in *OSA Annual Meeting 1992*, 1992, p. 1.

[126] I. Hartl, G. Imeshev, L. Dong, G. C. Cho, and M. E. Fermann, 'Ultra-compact dispersion compensated femtosecond fiber oscillators and amplifiers', in *2005 Conference on Lasers and Electro-Optics, CLEO*, 2005, pp. 1–3.

[127] M. E. Fermann and I. Hartl, 'Ultrafast fiber laser technology', *IEEE J. Sel. Top. Quantum Electron.*, vol. 15, no. 1, pp. 191–206, 2009.

[128] M. Brotons-Gisbert *et al.*, 'Comprehensive Theoretical and Experimental Study of Short- and Long-Term Stability in a Passively Mode-Locked Solitonic Fiber Laser', *J. Light. Technol.*, vol. 33, no. 19, pp. 4039–4049, 2015.

[129] A. Hartung, A. M. Heidt, and H. Bartelt, 'Pulse-preserving broadband visible supercontinuum generation in all-normal dispersion tapered

suspended-core optical fibers', *Opt. Express*, vol. 19, no. 13, pp. 12275–12283, 2011.

[130] Y. Liu *et al.*, 'Suppressing Short-Term Polarization Noise and Related Spectral Decoherence in All-Normal Dispersion Fiber Supercontinuum Generation', *J. Light. Technol.*, vol. 33, no. 9, pp. 1814–1820, 2015.

[131] G. P. Agrawal, *Fiber-Optic Communiction Systems*, 4th ed. 2010.

[132] B. T. Kuhlmey, R. C. McPhedran, and C. M. de Sterke, 'Modal cutoff in microstructured optical fibers', *Opt. Lett.*, vol. 27, no. 19, pp. 1684–1686, 2002.

[133] N. A. Mortensen, 'Effective area of photonic crystal fiber', *Opt. Express*, vol. 10, no. 7, pp. 341–348, 2002.

[134] I. A. Sukhoivanov, S. O. Iakushev, O. V. Shulika, J. A. Andrade-Lucio, A. Díez, and M. Andrés, 'Supercontinuum generation at 800 nm in all-normal dispersion photonic crystal fiber', *Opt. Express*, vol. 22, no. 24, pp. 30234–30250, 2014.

[135] K. Saitoh and M. Koshiba, 'Empirical relations for simple design of photonic crystal fibers', *Opt. Express*, vol. 13, no. 1, pp. 267–274, 2005.

[136] R. Photonics, 'Fiber joints, connectors, alignment tolerances, coupling loss, single-mode, multimode fiber'. [Online]. Available: https://www.rp-photonics.com/fiber_joints.html. [Accessed: 09-Sep-2023].

[137] M. Miranda, T. Fordell, C. Arnold, A. L'Huillier, and H. Crespo, 'Simultaneous compression and characterization of ultrashort laser pulses using chirped mirrors and glass wedges', *Opt. Express*, vol. 20, no. 1, pp. 688–697, 2012.

[138] S. Toenger *et al.*, 'Interferometric autocorrelation measurements of supercontinuum based on two-photon absorption', *J. Opt. Soc. Am. B*, vol. 36, no. 5, pp. 1320–1326, 2019.

[139] R. Trebino, *Frequency-Resolved Optical Gating: The Measurement of Ultrashort Laser Pulses*. Springer US, 2000.

[140] J. H. Chung and A. M. Weiner, 'Ambiguity of ultrashort pulse shapes retrieved from the intensity autocorrelation and the power spectrum', *IEEE J. Sel. Top. Quantum Electron.*, vol. 7, no. 4, pp. 656–666, 2001.

[141] B. C. Wilson and S. L. Jacques, 'Optical Reflectance and Transmittance of Tissues: Principles and Applications', *IEEE J. Quantum Electron.*, vol. 26, no. 12, pp. 2186–2199, 1990.

[142] T. Wang and C. Xu, 'Three-photon neuronal imaging in deep mouse brain', *Optica*, vol. 7, no. 8, pp. 947–960, 2020.

[143] T. Hori, N. Nishizawa, and T. Goto, 'Generation of 14-fs ultrashort pulse in all fiber scheme by use of highly nonlinear hybrid fiber', in *Springer Ser. Chem. Phys*, 2005, vol. 79, pp. 31–33.

[144] H. Ademgil and S. Haxha, 'Bending insensitive large mode area photonic crystal fiber', *Optik (Stuttg).*, vol. 122, no. 21, pp. 1950–1956, 2011.

[145] G. D. Krishna, G. Prasannan, S. K. Sudheer, and V. P. M. Pillai, 'Design of Ultra-Low Loss Highly Nonlinear Dispersion Flattened Octagonal Photonic Crystal Fibers', *Opt. Photonics J.*, vol. 5, no. 12, pp. 335–343, 2015.

[146] F. Begum and Y. Namihira, 'Design of supercontinuum generating photonic crystal fiber at 1.06, 1.31 and 1.55 μm wavelengths for medical imaging and optical transmission systems', *Nat. Sci.*, vol. 3, no. 5, pp. 401–407, 2011.

[147] A. Barrientos-García *et al.*, 'Numerical Study of Highly Nonlinear Photonic Crystal Fiber with Tunable Zero Dispersion Wavelengths', *J. Electromagn. Anal. Appl.*, vol. 7, no. 5, pp. 141–151, 2015.

[148] C. C. Wang, M. H. Wang, and J. Wu, 'Heavily germanium-Doped Silica Fiber With a Flat Normal Dispersion Profile', *IEEE Photonics J.*, vol. 7, no. 2, p. 7101110, 2015.

[149] J.-O. Carlsson and P. M. Martin, 'Chemical Vapor Deposition', in *Handbook of Deposition Technologies for Films and Coatings: Science, Applications and Technology*, Third Edit., Elsevier Ltd., 2010, pp. 314–363.

[150] H. Muñoz-Marco, J. Abreu-Afonso, G. Sardiello, and P. Pérez-Millán, 'Theoretical and experimental comprehensive study of GHz-range passively mode-locked fiber lasers', *Appl. Opt.*, vol. 59, no. 23, pp. 6817–6827, 2020.

[151] H. Muñoz-Marco *et al.*, 'Synchronous interferometric broadband measurement of dispersion applied to manufacturing optimization of microstructured optical fibers', in *SPIE Photonics Europe*, 2018, vol. 10681, no. May, p. 1068115.

[152] M. Young, 'Mode-field diameter of single-mode optical fiber by far-field scanning', *Appl. Opt.*, vol. 37, no. 24, pp. 5605–5619, 1998.

[153] N. Vermeulen *et al.*, 'Negative Kerr Nonlinearity of Graphene as seen via Chirped-Pulse-Pumped Self-Phase Modulation', *Phys. Rev. Appl.*, vol. 6, no. 4, p. 044006, 2016.

[154] M. Erkintalo, Y. Q. Xu, S. G. Murdoch, J. M. Dudley, and G. Genty, 'Cascaded Phase Matching and Nonlinear Symmetry Breaking in Fiber Frequency Combs', *Phys. Rev. Lett.*, vol. 109, no. 22, p. 223904, 2012.

[155] D. Castelló-Lurbe, 'Dispersive-wave self-frequency shift unveiled through length scales propagation', *Opt. Lett.*, vol. 46, no. 17, pp. 4152–4155, 2021.

[156] S. A. Planas, N. L. Pires Mansur, C. H. Brito Cruz, and H. L. Fragnito, 'Spectral narrowing in the propagation of chirped pulses in single-mode fibers', *Opt. Lett.*, vol. 18, no. 9, pp. 699–701, 1993.

[157] Y. Yatsenko and A. Mavritsky, 'D-scan measurement of nonlinear refractive index in fibers heavily doped with GeO2', *Opt. Lett.*, vol. 32, no. 22, pp. 3257–3259, 2007.

[158] S. Liu, F.-P. Yan, L.-N. Zhang, W.-G. Han, Z.-Y. Bai, and H. Zhou, 'Noise-like femtosecond pulse in passively mode-locked Tm-doped NALM-based

oscillator with small net anomalous dispersion', *J. Opt.*, vol. 18, no. 1, p. 015508, 2016.

[159] F. Leo, S.-P. Gorza, S. Coen, B. Kuyken, and G. Roelkens, 'Coherent supercontinuum generation in a silicon photonic wire in the telecommunication wavelength range', *Opt. Lett.*, vol. 40, no. 1, pp. 123–126, 2015.

[160] S. Coen *et al.*, 'Supercontinuum generation by stimulated Raman scattering and parametric four-wave mixing in photonic crystal fibers', *J. Opt. Soc. Am. B*, vol. 19, no. 4, pp. 753–764, 2002.

[161] J. N. Gannaway and C. J. R. Sheppard, 'Second-harmonic imaging in the scanning optical microscope', *Opt. Quantum Electron.*, vol. 10, no. 9, pp. 435–439, 1978.

[162] W. Denk, J. H. Strickler, and W. W. Webb, 'Two-Photon Laser Scanning Fluorescence Microscopy', *Science (80-. ).*, vol. 248, no. 4951, pp. 73–76, 1990.

[163] W. R. Zipfel, R. M. Williams, and W. W. Webb, 'Nonlinear magic: multiphoton microscopy in the biosciences', *Nat. Biotechnol.*, vol. 21, no. 11, pp. 1369–1377, 2003.

[164] E. E. Hoover and J. A. Squier, 'Advances in multiphoton microscopy technology', *Nat. Photonics*, vol. 7, no. 2, pp. 93–101, 2013.

[165] M. Ingaramo, A. G. York, E. J. Andrade, K. Rainey, and G. H. Patterson, 'Two-photon-like microscopy with orders-of-magnitude lower illumination intensity via two-step fluorescence', *Nat. Commun.*, vol. 6, p. 8184, 2015.

[166] M. Göppert-Mayer, 'Elementary processes with two quantum transitions', *Ann. Phys.*, vol. 18, no. 7–8, pp. 466–479, 2009.

[167] W. Kaiser and C. G. B. Garrett, 'Two-photon excitation in CaF2: Eu2+', *Phys. Rev. Lett.*, vol. 7, no. 6, pp. 229–231, 1961.

[168] D. B. Murphy, *Fundamentals of Light Microscopy and Electronic Imaging*, vol. 83, no. 991. John Wiley & Sons, Inc., 2001.

[169] V. Parodi, E. Jacchetti, R. Osellame, G. Cerullo, D. Polli, and M. T. Raimondi, 'Nonlinear Optical Microscopy: From Fundamentals to Applications in Live Bioimaging', *Front. Bioeng. Biotechnol.*, vol. 8, p. 585363, 2020.

[170] P. Xi, Y. Andegeko, L. R. Weisel, V. V. Lozovoy, and M. Dantus, 'Greater signal, increased depth, and less photobleaching in two-photon microscopy with 10 fs pulses', *Opt. Commun.*, vol. 281, no. 7, pp. 1841–1849, 2008.

[171] D. Stachowiak, J. Bogusławski, A. Głuszek, Z. Łaszczych, M. Wojtkowski, and G. Soboń, 'Frequency-doubled femtosecond Er-doped fiber laser for two-photon excited fluorescence imaging', *Biomed. Opt. Express*, vol. 11, no. 8, pp. 4431–4442, 2020.

[172] J. Boguslawski *et al.*, 'In vivo imaging of the human eye using a 2-photon-

excited fluorescence scanning laser ophthalmoscope', *J. Clin. Invest.*, vol. 132, no. 2, p. e154218, 2022.

[173] G. Krauss *et al.*, 'Compact coherent anti-Stokes Raman scattering microscope based on a picosecond two-color Er:fiber laser system', *Opt. Lett.*, vol. 34, no. 18, pp. 2847–2849, 2009.

[174] D. Stachowiak *et al.*, 'Femtosecond Er-doped fiber laser source tunable from 872 to 1075 nm for two-photon vision studies in humans', *Biomed. Opt. Express*, vol. 13, no. 4, pp. 1899–1911, 2022.

[175] E. C. S. C. on E. and N. I. H. R. (SCENIHR), 'Health Effects of Artificial Light'. p. 118, 2012.

[176] S. L. Jacques, 'Optical properties of biological tissues: A review', *Phys. Med. Biol.*, vol. 58, pp. R37–R61, 2013.

[177] K. Wang, N. G. Horton, K. Charan, and C. Xu, 'Advanced Fiber Soliton Sources for Nonlinear Deep Tissue Imaging in Biophotonics', *IEEE J. Sel. Top. Quantum Electron.*, vol. 20, no. 2, p. 6800311, 2014.

[178] G. Castro-Olvera *et al.*, 'Multimodal SWIR Laser Imaging for Assessment and Detection of Urothelial Carcinomas', in *Short-Wavelength Infrared Windows for Biomedical Applications*, SPIE, 2021, pp. 261–286.

[179] H.-Y. Chung, W. Liu, Q. Cao, F. X. Kärtner, and G. Chang, 'Er-fiber laser enabled, energy scalable femtosecond source tunable from 1.3 to 1.7 μm', *Opt. Express*, vol. 25, no. 14, pp. 15760–15771, 2017.

[180] N. G. Horton *et al.*, 'In vivo three-photon microscopy of subcortical structures within an intact mouse brain', *Nat. Photonics*, vol. 7, no. 3, pp. 205–209, Mar. 2013.

[181] C. Xu, W. Zipfel, J. B. Shear, R. M. Williams, and W. W. Webb, 'Multiphoton fluorescence excitation: New spectral windows for biological nonlinear microscopy', *Proc. Natl. Acad. Sci. U. S. A.*, vol. 93, pp. 10763–10768, 1996.

[182] ~ FYLA LASER S.L., 'Cyclone: Fiber Laser - Femtosecond Laser | FYLA'. [Online]. Available: https://fyla.com/laser/cyclone/. [Accessed: 30-May-2023].

[183] J.-X. Cheng and X. S. Xie, 'Coherent Anti-Stokes Raman Scattering Microscopy: Instrumentation, Theory, and Applications', *J. Phys. Chem. B*, vol. 108, no. 3, pp. 827–840, 2004.

[184] W. Becker, A. Bergmann, M. A. Hink, K. König, K. Benndorf, and C. Biskup, 'Fluorescence Lifetime Imaging by Time-Correlated Single-Photon Counting', *Microsc. Res. Tech.*, vol. 63, pp. 58–66, 2004.

[185] C. W. Chang, D. Sud, and M. A. Mycek, 'Fluorescence Lifetime Imaging Microscopy', *Methods Cell Biol.*, vol. 81, pp. 495–524, 2007.

[186] F. X. Kärtner, *Few-Cycle Laser Pulse Generation and Its Applications*. Berlin, Heidelberg: Springer Berlin Heidelberg, 2004.

[187] M. Maiuri, M. Garavelli, and G. Cerullo, 'Ultrafast Spectroscopy: State of the Art and Open Challenges', *J. Am. Chem. Soc.*, vol. 142, no. 1, pp. 3–15,

2020.

[188] T. Fortier and E. Baumann, '20 years of developments in optical frequency comb technology and applications', *Commun. Phys.*, vol. 2, p. 153, 2019.

[189] B. Debord, F. Amrani, L. Vincetti, F. Gérôme, and F. Benabid, 'Hollow-Core Fiber Technology: The Rising of "Gas Photonics"', *Fibers*, vol. 7, no. 16, pp. 1–58, 2019.

[190] J. C. Travers, W. Chang, J. Nold, N. Y. Joly, and P. S. J. Russell, 'Ultrafast nonlinear optics in gas-filled hollow-core photonic crystal fibers [Invited]', *J. Opt. Soc. Am. B*, vol. 28, no. 12, pp. A11–A26, 2011.

[191] M. Maurel *et al.*, 'Scalable hollow fiber pulse compressor for NIR and UV lasers', in *SPIE Photonic West 2019*, 2019, p. 10.

[192] F. Tani *et al.*, 'Temporal Self-Compression and Self-Frequency Shift of Submicrojoule Pulses at a Repetition Rate of 8 MHz', *Phys. Rev. Appl.*, vol. 18, no. 6, p. 064069, 2022.

[193] M. Azhar, G. K. L. Wong, W. Chang, N. Y. Joly, and P. S. J. Russell, 'High Pressure Gases in Hollow Core Photonic Crystal Fiber:A New Nonlinear Medium', *Arxiv*, pp. 1–7, 2012.

# List of figures

# List of tables

# List of acronyms

| | |
|---|---|
| 2PEF | Two-photon excitation fluorescence |
| 3PEF | Three-photon excitation fluorescence |
| ANDi | All-normal dispersion |
| CFBG | Chirped fiber Bragg grating |
| CPA | Chirped pulse amplification |
| D-scan | Dispersion-scan |
| DM | Dichroic mirror |
| DSF | Dispersion-shifted fiber |
| DW | Dispersive waves |
| FBG | Fiber Bragg grating |
| FFC | Fused fiber combiner |
| FTL | Fourier transform limit |
| FWHM | Full width at half maximum |
| FWM | Four-wave mixing |
| GC | Ganglion cells |
| GDD | Group delay dispersion |
| GFP | Green fluorescent protein |
| GRIN | Graded-index |
| GVD | Group velocity dispersion |
| HC | Hollow core |
| HOD | High-order dispersion |
| INL | Inner nuclear layer |
| IPL | Inner plexiform layer |
| MFD | Mode field diameter |
| MI | Modulation instability |
| MM | Multi-mode |
| MOF | Microstructured optical fiber |
| NA | Numerical aperture |
| NL | Nonlinear |
| NLE | Nonlinear effects |
| NLO | Nonlinear optical |
| NLSE | Nonlinear Schrödinger equation |
| ONL | Outer nuclear layer |
| OPL | Outer plexiform layer |
| OSP | Outer segment photoreceptors |

| | |
|---|---|
| OWB | Optical wave-breaking |
| PBG | Photonic bandgap |
| PCF | Photonic crystal fiber |
| PD | Photodetector |
| PLD | Pump laser diode |
| PM | Polarization maintaining |
| PMT | Photomultiplier tube |
| PSR | Peak-shoulder ratio |
| RI | Refractive immersion |
| RIFS | Raman-induced frequency shift |
| SC | Supercontinuum |
| SEM | Scanning electron microscope |
| SESAM | Semiconductor saturable absorber mirror |
| SHG | Second harmonic generation |
| SI | Step-index |
| SM | Single-mode |
| SPM | Self-phase modulation |
| THG | Third harmonic generation |
| Ti:Sa | Titanium:sapphire |
| TOD | Third-order dispersion |
| ZDW | Zero-dispersion wavelength |